LASER POWDER BED FUSION OF AISI H13 TOOL STEEL FOR TOOLING APPLICATIONS IN AUTOMOTIVE INDUSTRY

Laser Powder Bed Fusion of AISI H13 Tool Steel for Tooling Applications in Automotive Industry

By

MORTEZA NARVAN, BSc., MSc.

A Thesis

Submitted to the School of Graduate Studies in Partial Fulfillment of the Requirements

for the Degree Doctor of Philosophy

McMaster University

DOCTOR OF PHILOSOPHY (2021) McMaster University

(Mechanical Engineering) Hamilton, Ontario

TITLE: Laser Powder Bed Fusion of AISI H13 for Tooling Applications in Automotive Industry

AUTHOR: Morteza Narvan

B.Sc. in Mechanical Engineering (Azad University)

M.Sc. in Mechanical Engineering (University of Tehran)

SUPERVISORS: Dr. M. A. Elbestawi

NUMBER OF PAGES: xix, 175

Abstract

Owing to good combination of high hot hardness, wear resistance, toughness, and fairly low material cost in comparison to its counterparts, AISI H13 tool steel is commonly used in the manufacture of tooling and dies in different industries. Due to the layer-wise nature of the additive manufacturing (AM) techniques such as Laser Powder Bed Fusion (LPBF), they offer substantial geometric design freedom in comparison with conventional subtractive manufacturing methods, thereby enabling construction of complex near-net shape parts with internal cavities like conformal cooling channels.

In the context of AM, processing H13 tool steel is quite challenging, which in turn hurdles its implementation in industrial practices to manufacture reliable tools and dies. Because of the presence of martensite phase (as a brittle phase) and the considerable thermal stresses during the process, H13 tool steel has a high propensity to developing cracks in the final parts. Porosity, and surface quality are other major issues that must be appropriately dealt with. On the other hand, the presence of the residual stresses in the final part begs the question whether the costly stress-relief post-processing is mandatory. After meeting these challenges to get a defect-free parts, it would be of great interest to know if it is possible to utilize the capabilities of AM to design functional materials to enhance wear resistance of the monolithic H13. The following is the synopsis of the obtained results in regards to the abovementioned discussion.

First, the relative density, surface roughness, crack formation, microstructure, and hardness were evaluated. The relative density is shown to increase with increasing the volumetric energy density and then no significant increase could be pointed out; the maximum relative

density of 99.7% was obtained. A preheating of 200°C generally aided to increase the relative density and eliminated the crack formation in the final parts. The microstructure of as-built samples showed a fine cellular-dendritic structure composed of martensite as the predominant phase, and some retained austenite. The microhardness of the as-built samples was found to vary from 650 to 689 $HV_{0.2}$, which is superior to a conventionally produced H13 tool steel.

Second, residual stresses, as the other important defect developed during the laser powder bed fusion processing of H13 tool steel was thoroughly examined via experiment and part-level simulations. Twin-cantilever beams and cubic coupons were printed in a wide range of process parameters to characterize the nature of residual stresses and contributing factors under preheated and non-preheated conditions. The residual stresses were assessed using X-ray diffraction method (XRD) as a direct way of getting the residual stress figures at distinct spots and along the depth of cubic coupons. Moreover, the level of beam deflections, as an indication of the magnitude of residual stresses, were both measured and simulated to gain an insight into the accuracy of the part-level simulation. The XRD and beam deflection measurement results revealed the significant role of martensitic phase transformation, process parameters, densification level, and preheating condition on the final residual stress regime and consequently beam deflections. Neglecting the martensitic phase transformation and defects in the deflection modelling introduced a discrepancy between the predictions and experimental measurements. The knowledge gained from the microstructure and residual stress characterizations unraveled that 200°C of preheating eliminates not only the cracks but also the need for stress-relief post-processing.

At last, the feasibility of fabricating defect-free functionally graded bi-materials (FGMs) with enhanced wear resistance via incorporation of vanadium carbide (VC) into H13 tool

steel was investigated. Three distinct composite powders containing 1, 3, and 5wt.%VC were prepared through ball-milling and subjected to laser powder bed fusion (LPBF) process to print different composites on top of monolithic H13 in a wide range of process parameters. Almost fully-dense parts were achieved (maximum of 99.8, 99.8, and 99.5% for 1, 3 and 5wt.%VC composite systems, respectively); however, the increase in VC content narrowed down the processability window range from 60 J/mm3 for 1, and 3wt.%VC systems to 30 J/mm3 for 5wt.%VC system. The mechanical properties of optimum samples were characterized through microhardness, nanohardness, and wear tests. The incorporation of VC significantly improved the mechanical properties, 17-40% in microhardness, 10-40% in nanohardness, and 20-53% in wear resistance. The underlying reasons behind such an improvement were correlated to the dissolution of VC during the heating stage of the LPBF process and the formation of (V+C)-supersaturated solid solution in large extents as a result of extremely high cooling rates. This study introduces LPBF-processed FGMs as promising candidates for applications in which wear resistance is paramount.

Preface

This thesis deals with the LPBF processing of H13 tool steel for tooling applications. The thesis is composed of three journal papers and one conference paper (dedicated to the results of an industrial project). The followings list them in the order of the year:

Chapter 2: A version of this chapter is published in VMPT conference, McMaster university, Hamilton, Ontario. Narvan, M., and M. A. Elbestawi. "Metal Additive Manufacturing for Automotive Applications." (2018).

Chapter 3: A version of this chapter is published as a research paper: Narvan, Morteza, Kassim S. Al-Rubaie, and Mohamed Elbestawi. "Process-structure-property relationships of AISI H13 tool steel processed with selective laser melting." *Materials* 12.14 (2019): 2284.

Chapter 4: A version of this chapter is under-review in the *Materials & Design* journal as a research paper: Narvan, Morteza, Ali Ghasemi, Eskandar Fereiduni, and Mohamed Elbestawi. "Part level deflections and residual stresses in laser powder bed fusion of AISI H13 tool steel. " *submitted to the Materials & Design journal*. (2021)

Chapter 5: A version of this chapter is published as a research paper: Narvan, Morteza, et al. "Laser powder bed fusion of functionally graded bi-materials: Role of VC on functionalizing AISI H13 tool steel." *Materials & Design* (2021): 109503.

To my parents,

I owe you everything.

Acknowledgments

First and foremost, I would like to extend my most sincere gratitude to my supervisor Dr. Mohamed Elbestawi who has been a tremendous mentor and teacher. I would like to thank you for your support and patience along the way in this four-year journey. Your guidance has been and will be an invaluable asset in my academic life.

I would also like to extend my gratitude to my supervisory committee: Dr. André Phillion and Dr. Hatem Zurob, for interesting discussions, insightful comments, and guidance.

The XRD measurements pertaining to chapter 4 in this thesis were supported and performed in American Stress Technologies Inc. PA, USA. I would like to thank our collaborators from American Stress Technologies Inc., Stephen Kendrish and Jonathan Mohan, who provided insight and expertise that greatly assisted the research. The optical absorption measurements in chapter 5 were performed at the Department of Materials Engineering, KU Leuven, Belgium. I would also like to thank Suraj Dinkar Jadhav and Dr. Kim Vanmeensel for providing us with these measurements.

I would like to show my appreciation to my colleagues in the AMG group at McMaster University, for the discussions, presentation rehearsals, and fruitful group meetings.

Contents

List of Figures

List of Tables

Introduction

1.1 Background

Since its advent in the late 1980s, additive manufacturing (AM) technology has experienced years of development and is currently one of the rapidly growing advanced manufacturing techniques in the world [1, 2]. Contrary to the traditional manufacturing routes, AM implements a different path in achieving the final geometry of the part. AM encompasses shaping and consolidation of feedstock (predominantly powder materials) to arbitrary configurations in a layer-wise fashion, using a computer-controlled energy resource [3]. Initially, the computer aided design (CAD) model of the part to be produced is sliced into thin layers. The final geometry is then created by selective consolidation of the deposited material layers with a scanning laser energy source. Each shaped layer represents a cross-section of the sliced CAD model. Additive manufacturing technology, which involves a comprehensive integration of materials science, mechanical engineering, and laser technology, is regarded as an important revolution in manufacturing industry [4].

According to ASTM F2792-12a [5], AM technologies have been categorized into seven distinct groups. These techniques are used to print parts from a variety of materials including metals, polymers, and ceramics across a multitude of industries [6]. Powder Bed Fusion (PBF) process belongs to a category of AM processes that is widely used for fabrication of metallic components. In this process, a powder bed of predefined thickness is spread by raking the powder across the substrate. The heat source (electron beam or laser beam) delivers energy to the surface of the bed melting/sintering the powder on the specific

locations based on the data from the sliced CAD model. Once processing of the layer is accomplished, the substrate moves downwards one nominal layer thickness and the recoater spreads another powder layer for processing. The heat source engages to process the freshly spread layer. These steps would continue until the final shape of the component is achieved. The advantages of this system include its ability to produce high resolution features, internal features, and maintain dimensional control [7].

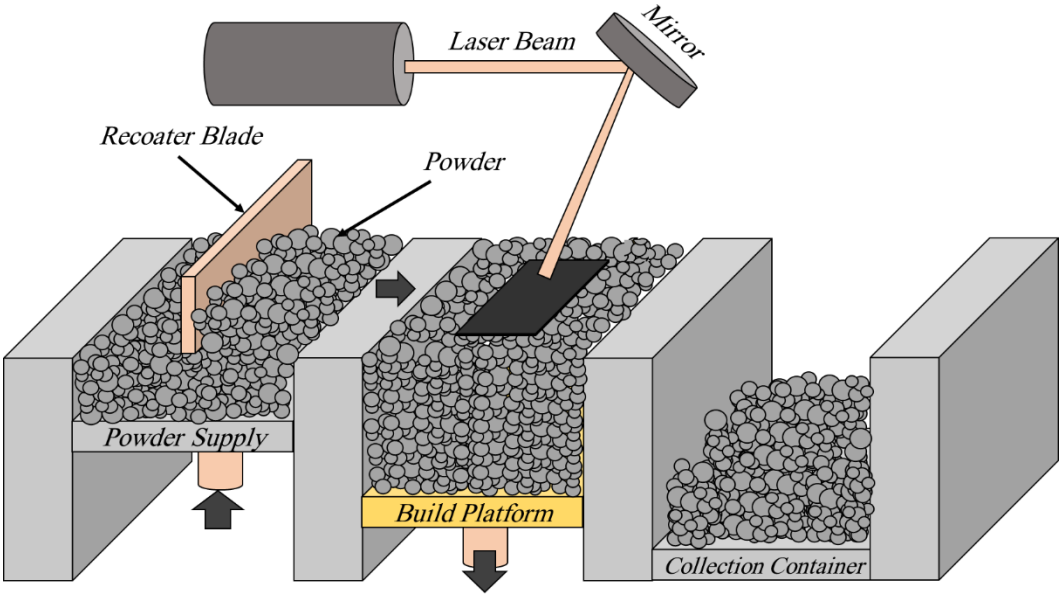

Figure 1-1 Illustration od a typical LPBF process.

One of the fields that LPBF process has greatly influenced is the possibility of applying a concept namely–"conformal cooling systems" to the dies and molds [8-10]. The main idea behind a conformal cooling system is that the cooling lines in the mold "conform" to the contours of the part leading into shorter cycle times and lower scrap rate originating from uniform cooling. However, the application of such a concept via conventional manufacturing routes might be challenging, if not impossible. The geometric freedom in

design that is brought readily by AM paves the way for application of such cost-saving ideas into real tooling applications.

Notwithstanding, full-scale implantation of such beneficial concepts might be hurdled by other determining factors. Materials aspect has always been a challenge in metal AM [11]. The presence of concentrated heat source (laser spot size in the order of hundredths of microns) in tandem with fast scanning speeds cause fast heating/cooling rates (in the order of ~10^5-10^6 K/s [12]). Such an adverse conditions experienced during the process leads into emerging a whole list of defects that might render the resultant parts useless. Currently, merely a few alloys can be printed reliably, AlSi10Mg, Ti6Al4V, CoCr, and IN718, to name a few [13]. Due to development of undesirable microstructures, large columnar grains (anisotropic properties), and periodic cracks, a vast majority of more than 5500 industrial alloys cannot be processed with AM [14-16].

AISI H13 tool steel, in specific, is a Cr-Mo hot work tool steel that has found its way in a wide variety of technological fields owing to its high wear resistance, outstanding thermal fatigue stability, superior strength at elevated temperatures and cost advantages [17-20]. The excellent balance of these properties has introduced H13 tool steel as a prime candidate in many applications including, plastic injection molding, die casting, and hot-extrusion industries [21-24]. In the context of AM, LPBF processing of H13 tool steel could be quite challenging. H13 tool steel has been designed to be processed via conventional manufacturing routes, like machining processes. H13 tool steel exhibits poor printability with LPBF process (as well as low weldability) due to its high hardenability. Once the laser moves away from the location of interest, the material in that location undergoes fast cooling, and hence, hardens. Such a transformation brings about stresses since the consolidated material is highly constrained, with a concomitant risk for cracking [25]. To

make matters worse, the as-built parts usually suffer from pores, rough surfaces, distortions originating from residual stresses, and loss of alloying elements [7], should the process parameters are not chosen carefully. It is worthwhile mentioning that full-scale implementation of AM technologies such as LPBF process in the tooling and die making industry requires close attention.

As discussed above, freedom in design is enabled by the capabilities of AM technology. However, the word "design" does not exclusively refer to the "geometric design". Materials with changing composition, microstructure, or porosity across the bulk of the material could be fabricated with AM technology. The design of functional materials is also a strength of AM technology. Fabrication of Functionally Graded Materials (FGMs) by implementing AM technology is a prime example of such capability. For instance, owing to its low heat conduction coefficient, H13 is not efficient from a thermal management perspective for certain part geometries. The use of functionally grading scheme to disperse copper (as a highly conductive material) to specific regions of the die could lead to enhanced heat dissipation [26].

It is worth mentioning that currently the materials used for tools, dies and equipment in automotive industry have performed adequately for many years, thus, their application represents a weak link to the current objectives related to increasing manufacturing efficiency and reducing energy consumption. In many applications, monolithic tooling materials have reached the limit of their usefulness. Tooling failures due to the low wear performance reduce tool life, and in turn, impose reduced machine uptime and reduced overall plant efficiency [27]. The possible solution to this shortcoming could be fabrication of FGMs utilizing AM technology.

The present thesis sets out to investigate processability of H13 tool steel in the context of LPBF process. The flaw development of the alloy including, densification behavior, cracking, surface roughness, and residual stresses will be investigated in detail. Such an effort will eliminate the barriers in front of the reliable printing of H13 tool steel in tooling industry. As mentioned above, freedom in geometric design is not the sole stronghold of AM technology. In order to materialize the full scope of AM capabilities in the tooling and die making industry, FGM will be fabricated targeting improvement in wear performance of the H13 tool steel.

1.2 Motivation

Canadian companies have always dominated the North American tool and mold manufacturers. In early November 2019, Michigan-based research firm Harbour Results released a report predicting that North American automotive tooling spending would worth roughly $6.5 billion to $8 billion per annum in the next five years [28].

Considering such huge market values on one hand, and the fact that current tools, dies and processing equipment used in industry are inefficiently manufactured using antiquated high energy processes and tooling materials developed in the 1940's and 1950's on the other hand, developing more robust techniques and materials for tool and die making industry is imperative.

1.3 Research objectives

The core aim of the current research is to use the full scope of additive manufacturing technology in tool and die making in automotive industry. AISI H13, as one of the most commonly used tool steels, will be the central focus of the current thesis. The objective of this work could be refined into the followings:

1) Develop a cost-effect solution to eradication of cracks in LPBF processing of H13 tool steel.
2) Characterize the different defect types in H13 tool steel components developed during the LPBF process.
3) Assess the Process-Structure-Property (PSP) relationships of H13 tool steel. By studying the effect of volumetric energy density and LPBF process parameters on the quality of H13 tool steel parts.
4) Characterize the residual stresses developed during the process and gain a clear understanding of the nature and the origin of such stresses. Investigating the effect of preheating on the status of the residual stresses in the LPBF process.
5) Develop Functionally Graded Materials (FGMs) to improve the wear performance of the H13 tool steel for the applications that wear resistance is highly demanded.

1.4 Thesis outline

Overall, the main results of this thesis have been prepared into three journal papers and a conference paper, in which two journal papers have already been published. One of the three journal papers is still under review. The thesis is comprised of the following chapters:

Chapter 1 introduces the background, motivation, and objectives of the research, to frame the scope of the thesis.

Chapter 2 entails summary of a conference paper that deals with an industrial project on the application of conformal cooling channels. The feasibility of application of conformal cooling channels into an existing die in the automotive industry has been investigated. This case study highlights the potential benefits of AM technology in the tooling and die making in automotive industry.

Chapter 3 is the first published journal article. This chapter targets Process-Structure-Property relationships for the H13 tool steel. Unlike alloying method, preheating of the substrate is suggested as a cost-effective solution to eradicate the cracking problem in the as-built H13 tool steel. The chapter describes in detail defect characterization of LPBF-processed samples. Moreover, the chapter presents the effect of different volumetric energy density (VED) on the quality of printed samples.

Chapter 4 is an under-review research that deals with in depth characterization of the residual stresses developed during the LPBF process. It helps to gain a clear understanding of the nature and the origin of such stresses in the as-built parts. Investigating the effect of preheating on the status of the residual stresses in the LPBF process was the other focus of this chapter.

Chapter 5 is the third accepted journal article. The chapter discusses the feasibility of creating FGM via implementing capabilities of AM to address a need in wear resistance in the case of H13 tool steel. Moreover, it presents thorough explanation on the hardening mechanisms that led to the improvement in the wear performance of the H13 tool steel.

Chapter 6 summarizes the main conclusions and contribution of the thesis, highlights the strength and limitations, and presents some suggestions for future work. Finally, it defines the contribution of this thesis to the literature.

1.5 References

[1] S.A.M. Tofail, E.P. Koumoulos, A. Bandyopadhyay, S. Bose, L. O'Donoghue, C. Charitidis, Additive manufacturing: scientific and technological challenges, market uptake and opportunities, Materials Today 21(1) (2018) 22-37.

[2] W. Gao, Y. Zhang, D. Ramanujan, K. Ramani, Y. Chen, C.B. Williams, C.C. Wang, Y.C. Shin, S. Zhang, P.D. Zavattieri, The status, challenges, and future of additive manufacturing in engineering, Computer-Aided Design 69 (2015) 65-89.

[3] W.E. Frazier, Metal additive manufacturing: a review, Journal of Materials Engineering and performance 23(6) (2014) 1917-1928.

[4] D.D. Gu, W. Meiners, K. Wissenbach, R. Poprawe, Laser additive manufacturing of metallic components: materials, processes and mechanisms, International materials reviews 57(3) (2012) 133-164.

[5] A. Standard, Standard terminology for additive manufacturing technologies, ASTM International F2792-12a (2012).

[6] A.J. Pinkerton, Lasers in additive manufacturing, Optics & Laser Technology 78 (2016) 25-32.

[7] T. DebRoy, H.L. Wei, J.S. Zuback, T. Mukherjee, J.W. Elmer, J.O. Milewski, A.M. Beese, A. Wilson-Heid, A. De, W. Zhang, Additive manufacturing of metallic components – Process, structure and properties, Progress in Materials Science 92 (2018) 112-224.

[8] M. Mazur, P. Brincat, M. Leary, M. Brandt, Numerical and experimental evaluation of a conformally cooled H13 steel injection mould manufactured with selective laser melting, The International Journal of Advanced Manufacturing Technology 93(1-4) (2017) 881-900.

[9] C.-C. Kuo, Z.-F. Jiang, X.-Y. Yang, S.-X. Chu, J.-Q. Wu, Characterization of a direct metal printed injection mold with different conformal cooling channels, The International Journal of Advanced Manufacturing Technology (2020) 1-16.

[10] C. Tan, D. Wang, W. Ma, Y. Chen, S. Chen, Y. Yang, K. Zhou, Design and additive manufacturing of novel conformal cooling molds, Materials & Design 196 (2020) 109147.

[11] T.D. Ngo, A. Kashani, G. Imbalzano, K.T.Q. Nguyen, D. Hui, Additive manufacturing (3D printing): A review of materials, methods, applications and challenges, Composites Part B: Engineering 143 (2018) 172-196.

[12] I.A. Roberts, C. Wang, R. Esterlein, M. Stanford, D. Mynors, A three-dimensional finite element analysis of the temperature field during laser melting of metal powders in additive layer manufacturing, International Journal of Machine Tools and Manufacture 49(12-13) (2009) 916-923.

[13] J.H. Martin, B.D. Yahata, J.M. Hundley, J.A. Mayer, T.A. Schaedler, T.M. Pollock, 3D printing of high-strength aluminium alloys, Nature 549(7672) (2017) 365-369.

[14] J. Dudas, Preventing weld cracks in high strength aluminum alloys, Welding journal 45 (1966) 3.

[15] N. Kaufmann, M. Imran, T.M. Wischeropp, C. Emmelmann, S. Siddique, F. Walther, Influence of process parameters on the quality of aluminium alloy EN AW 7075 using selective laser melting (SLM), Physics procedia 83 (2016) 918-926.

[16] H. Zhang, H. Zhu, T. Qi, Z. Hu, X. Zeng, Selective laser melting of high strength Al–Cu–Mg alloys: Processing, microstructure and mechanical properties, Materials Science and Engineering: A 656 (2016) 47-54.

[17] A.I.H. Committee, ASM Handbook: Properties and selection, Asm International1990.

[18] D. Papageorgiou, C. Medrea, N. Kyriakou, Failure analysis of H13 working die used in plastic injection moulding, Engineering Failure Analysis 35 (2013) 355-359.

[19] R. Mertens, B. Vrancken, N. Holmstock, Y. Kinds, J.-P. Kruth, J. Van Humbeeck, Influence of powder bed preheating on microstructure and mechanical properties of H13 tool steel SLM parts, Physics Procedia 83 (2016) 882-890.

[20] M. Wang, W. Li, Y. Wu, S. Li, C. Cai, S. Wen, Q. Wei, Y. Shi, F. Ye, Z. Chen, High-temperature properties and microstructural stability of the AISI H13 hot-work tool steel processed by selective laser melting, Metallurgical and Materials Transactions B 50(1) (2019) 531-542.

[21] M. Mazur, M. Leary, M. McMillan, J. Elambasseril, M. Brandt, SLM additive manufacture of H13 tool steel with conformal cooling and structural lattices, Rapid Prototyping Journal (2016).

[22] M. Katancik, S. Mirzababaei, M. Ghayoor, S. Pasebani, Selective laser melting and tempering of H13 tool steel for rapid tooling applications, Journal of Alloys and Compounds 849 (2020) 156319.

[23] L. Robert, Norton Machine Design; An Integrated Approach, Prentice-Hall, 1996.

[24] S. Taktak, Some mechanical properties of borided AISI H13 and 304 steels, Materials & design 28(6) (2007) 1836-1843.

[25] M. Narvan, K.S. Al-Rubaie, M. Elbestawi, Process-Structure-Property Relationships of AISI H13 Tool Steel Processed with Selective Laser Melting, Materials 12(14) (2019) 2284.

[26] V. Beal, P. Erasenthiran, N. Hopkinson, P. Dickens, C. Ahrens, The effect of scanning strategy on laser fusion of functionally graded H13/Cu materials, The International Journal of Advanced Manufacturing Technology 30(9-10) (2006) 844-852.

[27] L. Lherbier, D. Novotnak, D. Herling, J. Sears, Development of Functionally Graded Materials for Manufacturing Tools and Dies and Industrial Processing Equipment, Carpenter Powder Products-Bridgeville, PA, 2009.

[28] C. MetalWorking, Die/Mould Sector Report, 2020. https://www.canadianmetalworking.com/canadianmetalworking/article/covid19/diemould-sector-report.

Chapter 2

Conformal Cooling Channels: A Case study

Complete Citation:

Narvan, M., and M. A. Elbestawi. "Metal Additive Manufacturing for Automotive Applications." *VMPT conference* (2018), Hamilton, Canada.

Abstract:

Tooling is currently one of the promising applications of metal additive manufacturing in the automotive industry. Cooling is an important stage in injection molding processes. Cooling channels that conform to the geometry of the cavity feature better thermal management and consequently shorter cycle times and improved quality of parts. In the current work, four interior parts of an automobile were studied by the means of simulations using Moldex3D software. The current configuration of cooling channels was simulated and validated against the data from the experiment. Afterwards, the current cooling configuration was replaced with the devised conformal cooling channels. The results revealed, on the average, %28 reduction in cycle time and % 54 reduction in the warpage.

Keywords:

Additive Manufacturing, Conformal Cooling System, Productivity, Plastic Injection molding

1.1 Introduction

Automotive Industry has been a fertile ground for AM to be adopted as a manufacturing route to fabricate a variety of components addressing a plethora of needs. The automotive industry is one of the most competitive business arenas where mitigating time-to-tooling and time-to-market without having significant impact on the costs and lead time is paramount [1, 2]. Automotive companies are developing new models and concept designs every day, motivated by new design trends and technological evolution where aesthetics, aerodynamics, safety, and weight reduction of the vehicle are key issues [3]. Additive manufacturing has proven to be one of the most promising answers concerning rapid responses to market requirements. Other than the numerous advantages that AM has made possible on design grounds; it can contribute to increasing the productivity of the tooling used in the conventional manufacturing routes as well. For instance, one of the most noticeable applications of AM in tooling industry is the feasibility of incorporating conformal cooling channels. Conventional cooling channels are drilled in straight lines into the body of the die. In the case of freeform parts with complex geometries, these cooling channels fail to provide efficient cooling in the manufacturing process. Due to lack of uniform cooling across the part, long cycle time and warpage, result in appreciable increase in the scrap rate [4-6]. Moreover, conformal cooling channels follow the contours of the part leading to more efficient thermal management in the die and consequently better productivity.

Conformal cooling channels are gaining more attention as the AM technology continues to find its way into practical applications in industry. The current chapter summarizes the results of an industrial project dealing with the potential application of AM technology in automotive industry. An existing conventional design of cooling system was replaced an

appropriate conformal cooling design for a plastic injection mold. The cycle time and warpage status of the parts cooled with conventional and conformal case was compared.

2.1 Conformal cooling channels for a die in automotive industry: A case study

One of the most promising applications of additive manufacturing in automotive industry is the ability of incorporating conformal cooling system into the die. Injection molding has been the most popular method for making plastic products due to high efficiency and manufacturability. The injection molding process includes three significant stages: filling and packing stage, cooling stage, and ejection stage. Among these stages, the cooling stage is very important because it affects the productivity and molding quality. Normally, 70-80% of the molding cycle is taken up by the cooling stage. An appropriate cooling channels design can considerably reduce the cooling time and increase the productivity of the injection molding process. In addition, an efficient cooling system which achieves a uniform temperature distribution can minimize the undesired defects that influence the quality of molded part such as hot spots, differential shrinkage, thermal residual stress, and warpage. Moldex3D software was used to simulate and analyze the effect of conformal cooling application. The problem at hand is coupled-CFD analysis. It helps the user to define the thermal cycle of the molds, analyze the cycle time, and estimate the warpage.

2.1.1 Governing equations

In Moldex3D, the fluids are considered to be incompressible, Newtonian (for coolant) or generalized Newtonian (for the molten polymer). The governing equations for 3D transient non-isothermal motion are [7]:

$$\frac{\partial \rho}{\partial t} + \nabla . \rho \boldsymbol{u} = \mathbf{0} \quad \text{Eq.1}$$

$$\frac{\partial}{\partial t}(\rho \boldsymbol{u}) + \nabla . (\rho \boldsymbol{u}\boldsymbol{u} + \boldsymbol{\tau}) = -\nabla \boldsymbol{p} + \rho \boldsymbol{g} \quad \text{Eq.2}$$

$$\rho \boldsymbol{C_p} \left(\frac{\partial \boldsymbol{T}}{\partial \boldsymbol{t}} + \boldsymbol{u} . \nabla \boldsymbol{T}\right) = \nabla(\boldsymbol{\kappa} \nabla \boldsymbol{T}) + \boldsymbol{\eta} \dot{\boldsymbol{\gamma}}^{\mathbf{2}} \quad \text{Eq.3}$$

where $\boldsymbol{u}$ is velocity vector, T is temperature, t is time, p is pressure, τ is stress tensor, ρ is density, η is viscosity, k is thermal conductivity, Cp is specific heat and is shear rate. For the polymer melt, the stress tensor can be expressed as:

$$\boldsymbol{\tau} = -\boldsymbol{\eta}(\nabla \boldsymbol{u} + \nabla \boldsymbol{u}^{\boldsymbol{T}}) \quad \text{Eq.4}$$

The modified-Cross model with Arrhenius temperature dependence is employed to describe the viscosity of polymer melt:

$$\boldsymbol{\eta}(\boldsymbol{T}, \dot{\boldsymbol{\gamma}}) = \frac{\boldsymbol{\eta_0}(\boldsymbol{T})}{\mathbf{1} + \left(\frac{\boldsymbol{\eta_0}\dot{\boldsymbol{\gamma}}}{\boldsymbol{\tau^*}}\right)^{\mathbf{1}-\boldsymbol{n}}} \quad \text{Eq.5}$$

$$\boldsymbol{\eta_0}(\boldsymbol{T}) = \boldsymbol{B exp}\left(\frac{\boldsymbol{T_B}}{\boldsymbol{T}}\right) \quad \text{Eq.6}$$

where n is the power law index, η_0 is the zero-shear viscosity, τ^* is the parameter that describes the transition region between zero shear rate and the power law region of the viscosity curve. For the flow inside cooling channels, an incompressible Raynolds-averaged Navier-Stoke (RANS) model was applied [8].

2.1.2 Model description and results

The model used in this study was four plastic parts belonging to interior design of an automobile. The average dimensions of the parts were 425mm (L) ×82mm. The major thickness of the part was 5mm. Figure 2-1 illustrates the conventional and the devised conformal cooling systems layout. As it is apparent in Figure 2-1(a), the conventional design consists of straight cooling lines and baffles. The A 5-layer boundary layer meshing (BLM) scheme was adopted for the cooling channels and the part to capture the thermal and flow-related features in the process. The whole model consisted of 2682600 solid mesh elements. The parts were made up of ABS, (Lustran ABS PG298 marketed by INEOS Styrolution). All required material-related properties were extracted from material library of Moldex3D. For both cases, the process parameters were as follows (In accordance with actual process parameters used in the plant to manufacture the parts): The filling time was 1.46 seconds. Maximum injection pressure was 60MPa. Melt temperature at sprue entrance was 240°C. Packing time and maximum packing pressure were 25 seconds and 90MPa, respectively. Ejection temperature was 63°C. According to the experimental the total cycle time was around 73.7 seconds; the 40 seconds of which was cooling time. Initial mold temperature was 55°C. Mold open time was 5 seconds and air temperature were considered 25°C. The mold material was H13; a common tool steel used in injection molding industry. At last, the temperature and flow rate of the water in the cooling system were 50°C and 120cm^3/s respectively.

As the initial step, the current configuration of the die was simulated making sure that simulation results match up the experimental results. Figure 2-2 shows the simulated 3 cycles of the current design and the one with conformal cooling channels. The simulated results for the conventional design are consistent with the ones obtained in practice (cycle

time in actual practice≈ 73 seconds). As it is evident from the simulated results, parts under conformal cooling system experience much lower average peak temperatures. This contributes to significant improvements in the final quality of the produced parts.

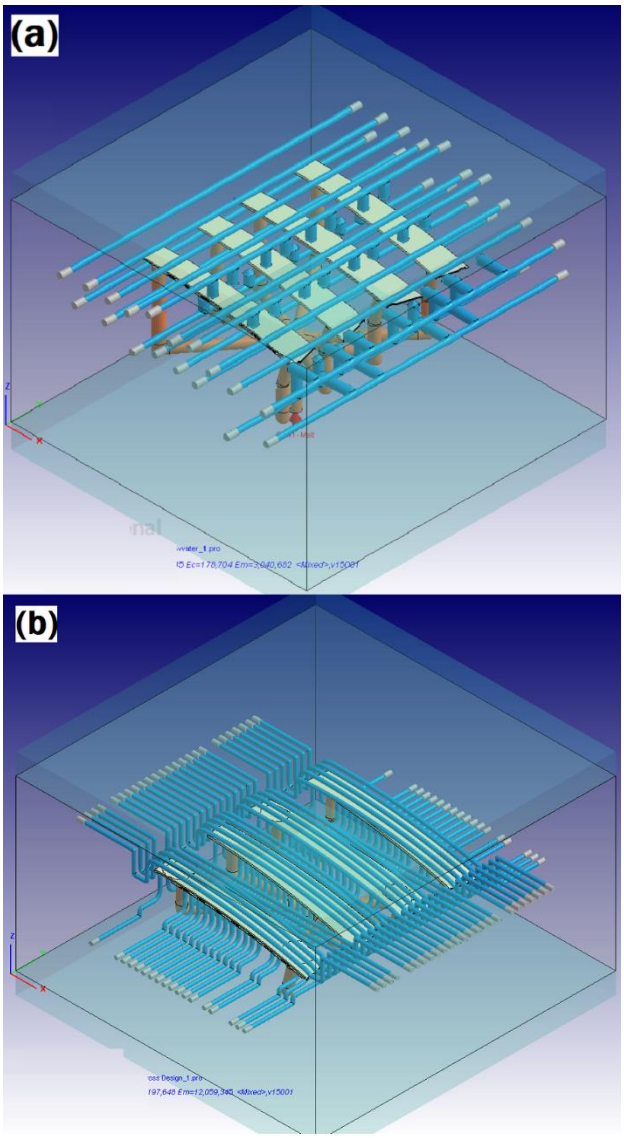

Figure 2-1 a) Conventional cooling system of the current design b) Devised conformal cooling system.

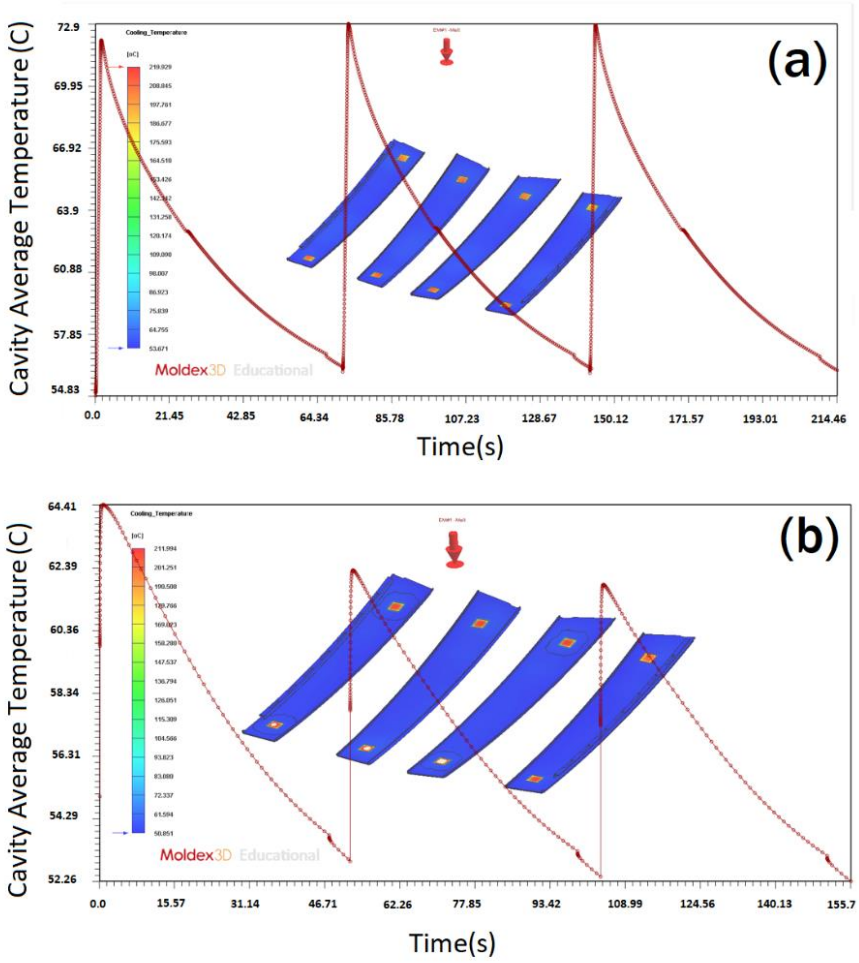

Figure 2-2. simulated results for 3 cycles in a) Current design b) Design with conformal cooling

Figure 2-3 presents the total displacement modified die and the original design. The modified design features total displacement range between 0.267-1.74 mm corresponding to an average amount of 0.616 mm, as opposed to the original design with displacement of 0.428-4.36 mm averaging to 1.34 mm. Through drawing comparison between two designs, it is clear that conformal cooling system, by creating a much more uniform and lower temperature distribution across the part, improves the warpage status by %54. Residual stresses are the stresses remaining inside the moulded product under condition of no

external loads. Internal stresses are frozen inside the part in the moulding process. Residual stresses affect a part similarly to externally applied stresses and are the main cause of part shrinkage and warpage. The average thermally induced residual stress in the modified design decreased from 3.1 MPa in the initial design down to 1.7 MPa which explains the improvement in the warpage status.

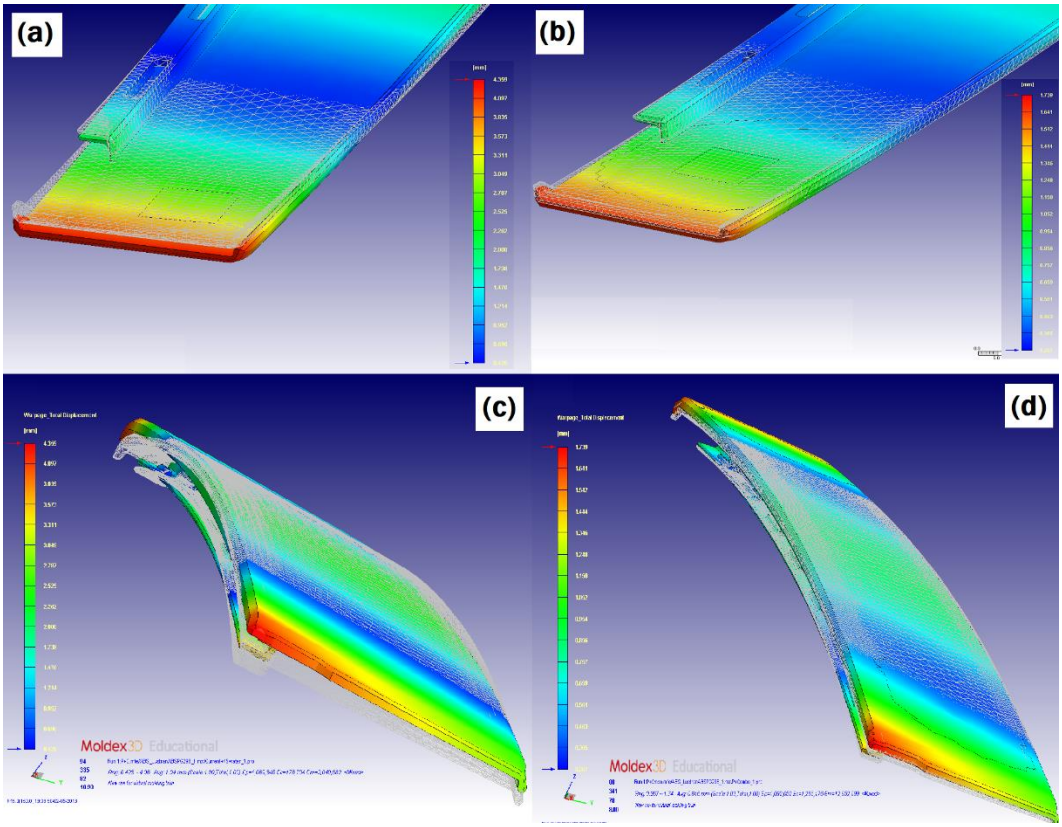

Figure 2-3 Warpage status (a, c) the total displacement in the conventional cooling system (b, d) total displacement in the conformally cooled part.

2.2 Conclusions

This research work evaluates the feasibility of the incorporation of conformal cooling system into an existing plastic injection molding die with conventional cooling system to manufacture automobile parts made of ABS. A three-dimensional numerical scheme was implemented to prove the advantages of the application of the conformal cooling system. The results revealed, on the average, %28 reduction in cycle time and % 54 reduction in the warpage. This is attributable to improved heat dissipation and uniform cooling provided by the conformal cooling system.

2.3 References

[1] R. Leal, F. Barreiros, L. Alves, F. Romeiro, J. Vasco, M. Santos, C. Marto, Additive manufacturing tooling for the automotive industry, The International Journal of Advanced Manufacturing Technology 92(5-8) (2017) 1671-1676.

[2] S.G. Sarvankar, S.N. Yewale, Additive manufacturing in automobile industry, Int. J. Res. Aeronaut. Mech. Eng 7(4) (2019) 1-10.

[3] C. Costa, J. Aguzzi, Temporal shape changes and future trends in European automotive design, Machines 3(3) (2015) 256-267.

[4] M.S. Shinde, K.M. Ashtankar, Additive manufacturing–assisted conformal cooling channels in mold manufacturing processes, Advances in Mechanical Engineering 9(5) (2017) 1687814017699764.

[5] C.-C. Kuo, W.-C. Xu, Effects of different cooling channels on the cooling efficiency in the wax injection molding process, The International Journal of Advanced Manufacturing Technology 98(1) (2018) 887-895.

[6] C.-C. Kuo, Z.-F. Jiang, J.-H. Lee, Effects of cooling time of molded parts on rapid injection molds with different layouts and surface roughness of conformal cooling channels, The International Journal of Advanced Manufacturing Technology 103(5) (2019) 2169-2182.

[7] F. Hsu, K. Wang, C. Huang, R. Chang, Investigation on conformal cooling system design in injection molding, Advances in Production Engineering & Management 8(2) (2013) 107-115.

[8] F.M. White, I. Corfield, Viscous fluid flow, McGraw-Hill New York2006.

Chapter 3

Process-Structure-Property Relationships of AISI H13 Tool Steel Processed with Selective Laser Melting

Complete Citation:

Narvan, Morteza, Kassim S. Al-Rubaie, and Mohamed Elbestawi. "Process-structure-property relationships of AISI H13 tool steel processed with selective laser melting." *Materials* 12.14 (2019): 2284. https://doi.org/10.3390/ma12142284

Abstract:

Due to a good combination of high hardness, wear resistance, toughness, resistance to high operating temperatures, and fairly low material cost, AISI H13 tool steel is commonly used in the manufacture of injection molds. Additive manufacturing (AM) such as selective laser melting (SLM), due to the layer-wise nature of the process, offers substantial geometric design freedom in comparison with conventional subtractive manufacturing methods, thereby enabling a construction of complex near-net shape parts with internal cavities like conformal cooling channels. The quality of SLM-manufactured parts mainly depends on the part geometry, build orientation and scanning strategy, and processing parameters. In this study, samples of H13 tool steel with a size of 10×10×15 mm^3 were SLM-manufactured using a laser power of 100, 200, and 300 W; scanning speed of 200, 400, 600, 800, 1000, and 1200 mm/s; and hatch spacing of 80 and 120 µm. A constant layer thickness of 40 µm, 67° scanning rotation between subsequent layers, and a stripe scanning strategy were maintained during the process. The samples were built considering a preheating of 200°C. The relative density, surface roughness, crack formation, microstructure, and hardness were evaluated. The relative density is shown to increase with increasing the volumetric energy density up to a value of about 60 J/mm^3 and then no significant increase can be pointed out; the maximum relative density of 99.7% was obtained. A preheating of 200°C generally aids to increase the relative density and eliminate the crack formation. The microstructure of built samples shows fine equiaxed cellular-dendritic structure with martensite and some retained austenite. The microhardness of the as-built samples was found to vary from 650 to 689 $HV_{0.2}$, which is comparable to a conventionally produced H13 tool steel.

Keywords:

H13 tool steel; selective laser melting; volumetric energy density; relative density; surface roughness; microstructure.

Acknowledgment:

The authors would like to acknowledge the Materials Property Assessment Lab (MPAL) at McMaster Manufacturing Research Institute (MMRI), and the Centre for Advanced Nuclear Systems (CANS) for their electron microscopy facility.

3.1 Introduction

Owing to the layer-wise nature of the process, additive manufacturing (AM) technology allows with a high degree of accuracy for the manufacture of complex-shape geometries, quite difficult or impossible to obtain using conventional material-removal processes, hence opening significant opportunities up for the design of novel geometries and complex internal structures. The manufacture of a given part using AM technique is based on the slicing its 3D CAD model into multiple layers, creating a tool path for each layer, uploading the data in the AM machine, and building the part up layer by layer, following the sliced model [1, 2]. To build a layer of predefined geometry, the powder is melted by a focused heat source provided by an electron beam, laser, plasma or electric welding arc, etc. The fabrication of a component by AM technology does therefore aid to eliminate the need for molds and dies or any additional fixtures, coolants and cutting tools, with minimal finishing operations, resulting in a significant reduction in lead-time, material wastes, energy, and costs. Due to its vast advantages, AM has become a crucial alternative manufacturing technique for small quantities of components having complex geometries [1]. In addition to polymers, ceramics, and composites, a variety of metallic materials can be fabricated by AM. Of several AM processes, selective laser melting (SLM) has gained an essential role in the field of metallic materials. SLM implies that a laser beam selectively melts and fuses accumulating layers of powder.

The SLM technique has recently attracted the attention of the tool and die manufacturers, owing to the possibility of producing tool inserts with sophisticated features like conformal cooling channels [3-5]. The idea behind the conformal cooling system is to conform the 3D geometry of the cooling channels to the contours of the part, aiming at maximizing heat dissipation, uniform cooling, ultimately, higher productivity. However, the response of the

conventional alloys to the acute conditions experienced in the process could restrict full implementation of conformal cooling systems. In comparison to the traditional manufacturing routes, materials fabricated by SLM display distinctive microstructures, being direct result of the interaction of a focused high energy laser beam with the material that leads to high heating and cooling rates, rapid solidification, and large thermal gradients within the melt pools [6]. By far, despite the high interest in this technology, only few alloys have been processed reliably by the SLM [7] and, in particular, very limited studies have been published on the high strength steels for tooling. Some studies have targeted maraging steels, investigating the material processing and the effects of post-process heat treatments on the microstructure and mechanical properties [8-10]. In other studies, processing parameters and microstructural features of SLM-manufactured M2 high speed tool steel, some grades of cold-work tool steels, and H11 hot-work tool steel have been investigated [11-16].

Due to a good combination of high hardness, wear resistance, toughness, resistance to high operating temperatures and thermal fatigue, and fairly low material cost, AISI H13 hot-work tool steel is commonly used in the manufacture of injection molds. H13 tool steel finds its core applications in processes such as plastic injection molding, die casting, forging, and extrusion [17]. H13 tool steel exhibits a complex processing behavior owing to its high hardenability resulting from the high carbon level and alloying elements. The change in specific volume during phase transformation in the solid state can bring about additional stresses, consequently, promoting crack propagation and distortion.

Although SLM has benefited the industry by providing the designers with a significant freedom in design, its full implementation is restricted by common defects generated during the process. Porosity, cracking, surface roughness, loss of alloying elements, and

residual stresses are commonly known defects in SLM [18]. Understanding the behavior of the material in response to the processing parameters and subsequently finding a safe processing window to avoid these defects is paramount. This work aims to study the behavior of SLM-manufactured H13 hot-work tool steel under a wide variety of processing parameters. Moreover, preheating is investigated as an effective way to diminish the developed defects during the process.

3.2 Experimental procedures

3.2.1 Powder material

The gas-atomized AISI H13 powder used in this work was supplied by LPW Company (United Kingdom). The particle size distribution (PSD) was measured using the laser diffraction wet method via the Master Sizer 3000 (Malvern, Worcestershire, UK) instrument with the powder dispersed in water. PSD is quantified by D (α), which represents the diameter of the measured particle, where α is the volume percentage of the particles that have a smaller diameter than D. The powder morphology was investigated using a TESCAN VP (TESCAN, Brno, Czech Republic) scanning electron microscope (SEM). Figure 3-1 shows the morphology and PSD of the powder material used in this work. The chemical composition of the powder used in this study was measured using ICP-OES by digestion. Table 3-1 shows the chemical composition of AISI H13 powder.

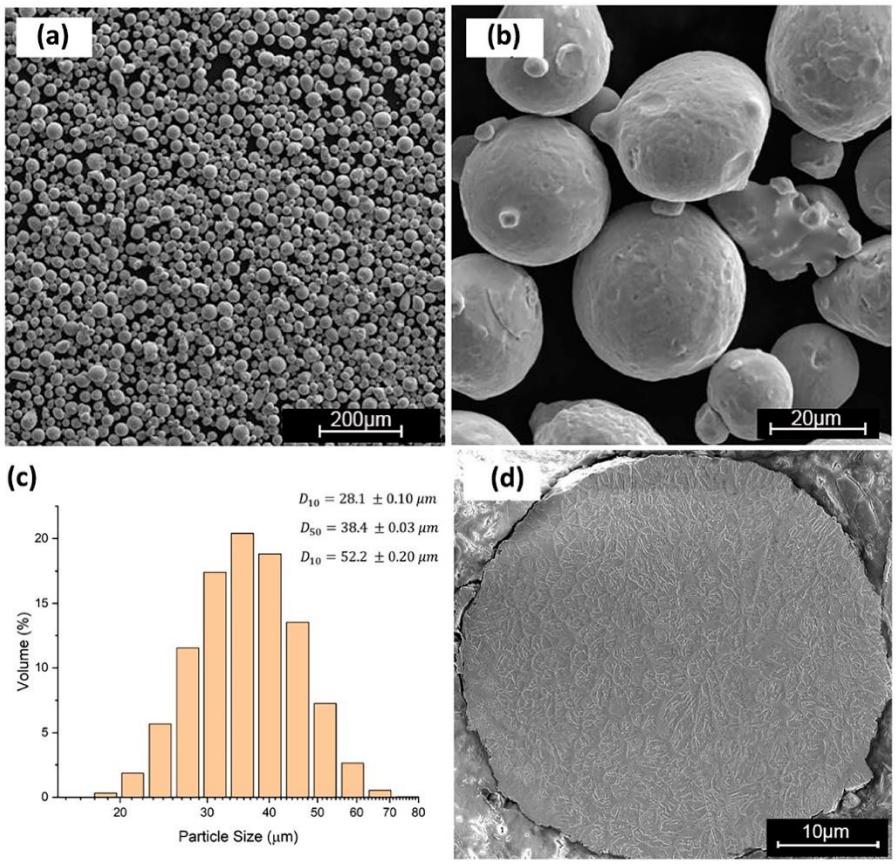

Figure 3-1 Characteristics of H13 powder: (a,b) Powder morphology; (c) particle size distribution (PSD) analysis; and (d) cross-section of the powder particle.

Table 3-1 Chemical composition of AISI H13 powder.

Element (wt.%)	*Cr*	*Mo*	*Si*	*V*	*Mn*	*C*	*Fe*
ASTM-A681	4.75–5.5	1.10–1.75	0.8–1.25	0.8–1.2	0.2–0.6	0.32–0.45	Bal.
Reported by Supplier	5.36	1.38	1.12	1.05	0.42	0.39	Bal.
ICP-OES	5.27	1.34	1.08	0.97	0.40	0.39	Bal.

3.2.2 SLM processing parameters

AISI H13 samples were fabricated using the SLM process on an EOS M280 machine (EOS, Krailling, Germany) equipped with a fiber laser system delivering power levels of up to a maximum of 400 W. An atmosphere of nitrogen gas was applied to reduce the oxygen content in the build chamber to less than 0.1%, hence reducing the oxidation during the melting process. The most important SLM process parameters include laser power, scanning speed, hatch spacing, and layer thickness, as shown in Figure 3-2(a). These parameters can be combined to calculate the volumetric laser energy density using Eq.1:

$$E_v = \frac{P}{v \times h \times t} \left[\frac{J}{mm^3}\right] \quad \text{Eq.1}$$

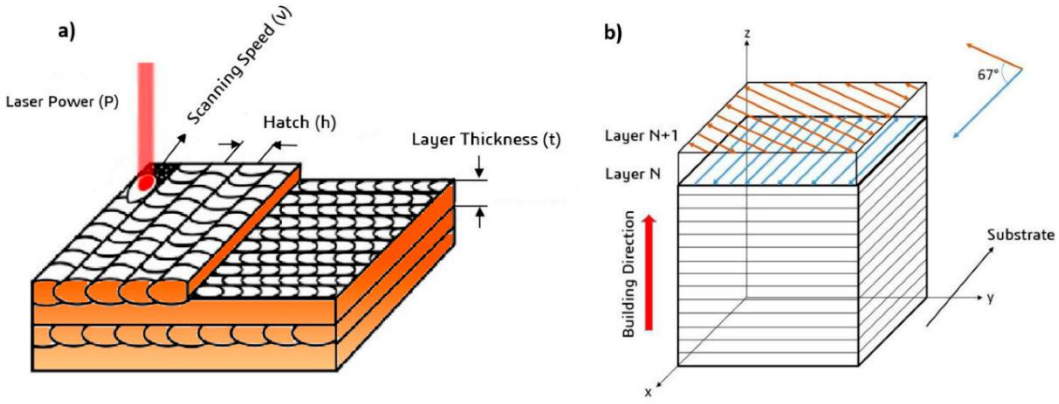

Figure 3-2 Schematic presentation of selective laser melting (SLM) processing: (a) SLM process parameters; and (b) scanning strategy.

where: E_v: Volumetric laser energy density (J/mm^3), P: Laser power (W), v: Scanning speed (mm/s), h: Hatch spacing (mm), and t: Layer thickness (mm).

In this study, samples of H13 tool steel with a size of 10×10×15 mm^3 were SLM-manufactured using a laser power of 100, 200, and 300 W; scanning speed of 200, 400, 600, 800, 1000, and 1200 mm/s; and hatch spacing of 80 and 120 µm. A full factorial

design of experiments (DOE) was adapted to design the experimental matrix. Each run was repeated 3 times. In order to investigate the effect of preheating on the flaw development of the material at hand, the same set of process parameters in the devised DOE was printed applying a preheating of 200°C to the build plate. The samples were produced directly on the build plate and did not undergo any post-processing procedures. A constant layer thickness of 40 µm, 67° scanning rotation between subsequent layers (Figure 3-2(b)), and a stripe scanning strategy were maintained during the process. The contouring, up-skin, and down-skin parameters were deactivated so that only the hatching parameters were considered. Table 3-2 presents the design of test matrix and Figure 3-3 shows the calculated volumetric energy density across the design matrix against scanning speed. The devised design matrix encompasses volumetric energy densities ranging from 17.36–465.75 J/mm^3. The sample codes having the prefix P have been printed with preheating of 200°C.

Table 3-2 Design of experiments implemented in this work.

Sample Code	*P(W)*	*v(mm/s)*	*h(µm)*	*Sample Code*	*P(W)*	*v(mm/s)*	*h(µm)*	*Sample Code*	*P(W)*	*v(mm/s)*	*h(µm)*
A1	100	200	80	**B1**	200	200	80	**C1**	300	200	80
A2	100	200	120	**B2**	200	200	120	**C2**	300	200	120
A3	100	400	80	**B3**	200	400	80	**C3**	300	400	80
A4	100	400	120	**B4**	200	400	120	**C4**	300	400	120
A5	100	600	80	**B5**	200	600	80	**C5**	300	600	80
A6	100	600	120	**B6**	200	600	120	**C6**	300	600	120
A7	100	800	80	**B7**	200	800	80	**C7**	300	800	80
A8	100	800	120	**B8**	200	800	120	**C8**	300	800	120
A9	100	1000	80	**B9**	200	1000	80	**C9**	300	1000	80
A10	100	1000	120	**B10**	200	1000	120	**C10**	300	1000	120
A11	100	1200	80	**B11**	200	1200	80	**C11**	300	1200	80
A12	100	1200	120	**B12**	200	1200	120	**C12**	300	1200	120

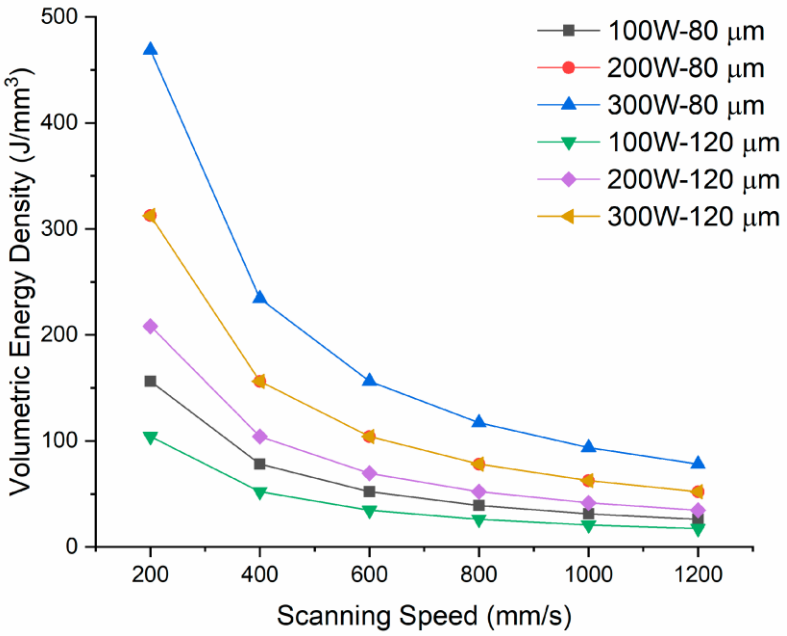

Figure 3-3 Volumetric energy density variation across the design matrix.

3.2.3 Sample characterization methods

The density of the as-built samples was measured using Archimedes principle with the aid of a scale with accuracy of ±0.1 mg. The Keyence (Osaka, Japan) VHX series of digital microscopes, a digital optical microscope, was used to investigate the cracks and observable microstructural features. The Alicona G5 “Infinite Focus” (Bruker alicona, Graz, Austria), a focus variation measuring instrument, was used to quantify the surface roughness of the samples. The Verios XHR scanning electron microscope from Thermo-Fisher Scientific (Waltham, MA, USA) was used to perform electron backscatter diffraction (EBSD) and energy-dispersive X-ray spectroscopy (EDS). To detect the phases present in the microstructure of SLM-manufactured samples, X-ray Diffraction (XRD) was carried out using a Bruker D8 DISCOVER (Billerica, MA, USA) with a DAVINCI design diffractometer equipped with a cobalt sealed tube source (wavelength of 1.7902 Å) and a

VANTEC-500 area detector. For these measurements, a range of 20–130° 2θ with a step size of 0.01° and an acquisition time of 2 s per increment were used. Pattern analysis was performed with the software DIFFRAC.EVA V3.0 (Billerica, MA, USA).

For microstructural analysis, samples were cut via wire-cut EDM along the build direction. Then, the samples were ground using SiC abrasive papers with a mesh of 600, 800, 1200, 2400, and 4000 followed by a polishing process using a diamond paste of a size 6, 3, and 1 µm. In addition, the samples were chemically etched with 4% nital reagent and evaluated using SEM and a Nikon LV100 optical microscope. For EBSD analysis, the aforementioned procedure of the samples was followed by a 5-min polishing on a chemical resistant cloth with a colloidal silica suspension, and finally a 4-h vibratory polishing with the same suspension. Vickers micro-indentations were made using a load of 200 gf. Six measurements on the polished surface of each sample were carried out and the average was used. Moreover, nano-indentations were made using Anton Paar NHT3 nano-indentation tester (Anton Paar, Graz, Austria), in which the testing parameters were as follows: Maximum load used = 50 mN, loading and unloading rate = 100 mN/min, and the dwell time was 5 s.

3.3 Results and discussion

The manufacturing process to build the batch of samples took a continuous 22 h to finish; however, as can be observed in Figure 3-4(a), nine samples failed in every three repetitions. The main reason for this failure was the collision of these 10 samples and the powder recoater. The referenced samples were excluded from the batch in the first hour of the printing operation, since this interference could have resulted in imminent damage to the ceramic recoater, a very fragile component of the machine. The root cause of the printing

failure of these samples is related to the fact that these samples have high laser energy density, ranging from 150 to 480 J/mm^3. Thus, on each layer, the molten material accumulates on the border due to heat and mass transport, resulting in a thick solidified "protrusion", on all four edges of the samples, as indicated in Figure 3-4(b). It is worth mentioning that the same parts, i.e., associated with the volumetric energy densities of above 150 J/mm^3, also failed under preheating condition.

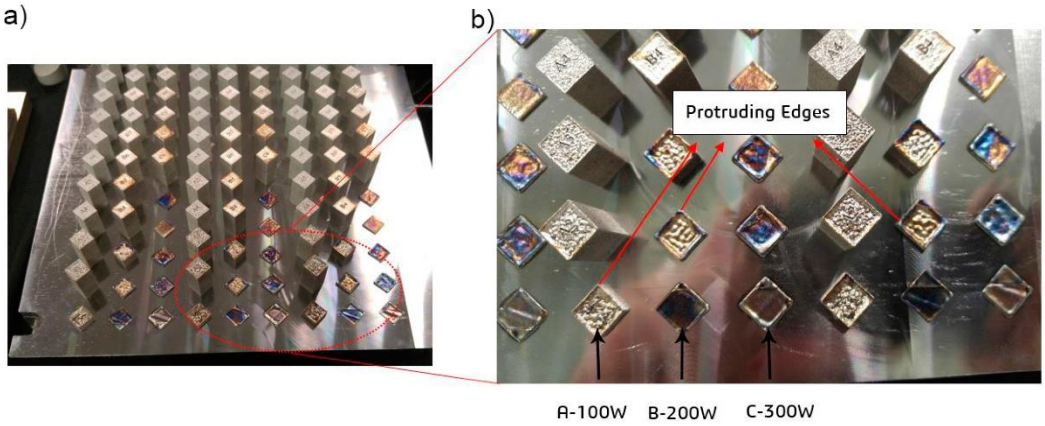

Figure 3-4 SLM-processed samples: (a) Failed parts are within the red ellipse; and (b) protruding edges of the failed parts.

3.3.1 Densification behavior

Figure 3-5 shows the effect of volumetric energy density on the relative density of the SLM-processed H13 parts. With and without substrate preheating of 200 °C, the results showed that increasing the energy density level sharply increases the relative density of the samples in a non-linear fashion up to a value of approximately of 60 J/mm^3 and then no significant increase can be seen. The increase in relative density was found to be higher for the samples with preheating process than those without preheating. The effectiveness of

increasing laser energy density on increasing the relative density has been confirmed for different materials [19-21].

Porosity and lack of fusion are common defects that develop during additive manufacturing processes. If not reduced or eliminated, they could adversely affect the mechanical properties of the components [22]. There are a couple of mechanisms enhancing the development of porosity in additive manufacturing.

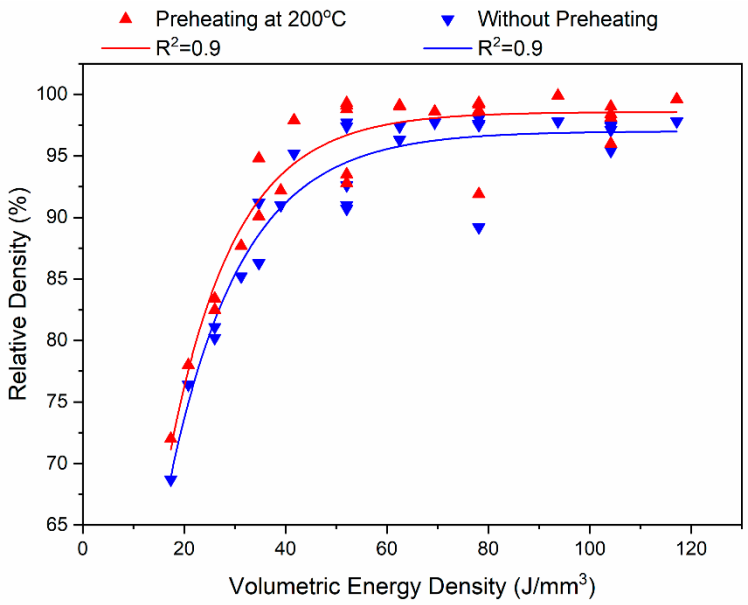

Figure 3-5 Effect of energy density on the relative density of the parts with and without preheating.

Operating in the keyhole mode associated with higher energy densities, entrapped gas porosities inside the powder particles during the atomization process that leave micro-porosities in the part, interaction of the shielding gas or vaporization products with the melt, and lack of fusion defects that are attributed to low energy inputs insufficient to create full melting [18].

Figure 3-6 illustrates the influence of individual process parameters in a one-factor-at-a-time (OFAT) manner. Increasing the scanning speed at the same power level has a negative effect on the relative density of the parts because at higher scanning speeds the laser energy is insufficient for complete melting of the powder bed, thereby resulting in a lack of fusion between layers.

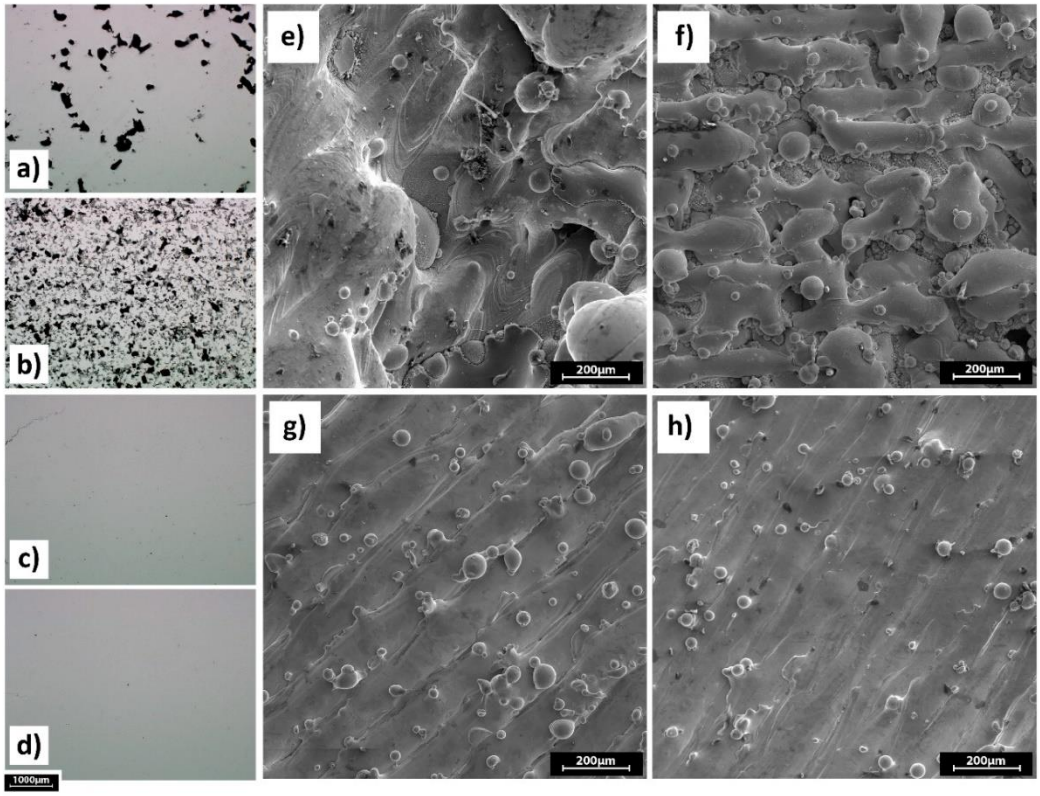

Figure 3-6 Effect of process parameters on the relative density of the samples, optical micrographs of the cross-sections: (a) Sample A2; (b) sample A10; (c) sample C10; and (d) sample C9. SEM micrographs of the top surfaces of samples: (e) Sample A2; (f) sample A10; (g) sample C10; and (h) sample C9.

This lack of fusion leads to increased pores and voids, which in turn tend to decrease the relative density. As it is shown in Figure 3-6(a,b) that corresponds to parts A2 (P = 100 W,

v = 200 mm/s, h = 120 µm) and A10 (P = 100 W, v = 1000 mm/s, h = 120 µm) respectively, sample A10 features more porosity due to incomplete melting which is evident in the Figure 3-6(f). Whereas, sample A2 suffers from severe balling shown in Figure 3-6(e). Figure 3-6(c,d) correspond to parts C10 (P = 300 W, v = 1000 mm/s, h = 120 µm) and C9 (P = 300 W, v = 1000 mm/s, h = 80 µm), respectively. A comparison between Figure 3-6(a–d) clearly shows the influence of increasing laser power on the part quality. In this work, a considerable jump in relative density level was observed in transition from a laser power of 100 W to 200 W. This difference became less significant from 200 W to 300 W. Although hatch spacing is an important factor that could strongly affect the relative density of the SLM-built parts [23], increasing the hatch spacing from 80 and 120 µm brought about no significant difference in the density results. This is because the chosen hatch spacing levels are both equally optimum.

The preheating process can affect the part density, depending on the temperature applied. Upon application of preheating, less heat input is needed from the laser source to melt the powder. That is why, with the use of preheating process, higher scan speeds can be used to produce equally dense parts. In this case, additional post processing may be avoided, thus leading to a more time and cost efficient SLM process [17]. As shown in Figure 3-5, the differences between the relative density values of the preheated and non-preheated parts are not too high. However, significant differences may be expected on increasing the preheating temperature to higher values.

3.3.2 Cracking behavior

Cracking is another commonly encountered defect in additive manufactured parts that, if not accounted for, could seriously limit parts performance in service. When fabricating H13 tool steel by SLM process, high thermal stresses associated with the process can bring about cracking and delamination from the baseplate. Figure 3-7 illustrates the mechanism by which thermal stresses can trigger thermally-induced cracking in each layer during the SLM process. Due to the high temperature in the upper layers of the solid substrate, these upper layers will expand, while the colder underlying solidified layers will restrict this expansion. This induces compressive stresses in the upper layers of the substrate that may rise above the yield strength of the material and cause plastic upsetting in upper layers. When the yield strength is reached, the compressive stresses cause plastic deformation in the upper layers. When these plastically deformed layers cool down, their compressive state is converted into residual tensile stresses. These residual stresses may induce cracking of the part. Furthermore, the melted top layers tend to shrink due to thermal contraction. This deformation is again prohibited by the underlying layers, thus introducing tensile stresses in the top layers, and compressive stresses below [11].

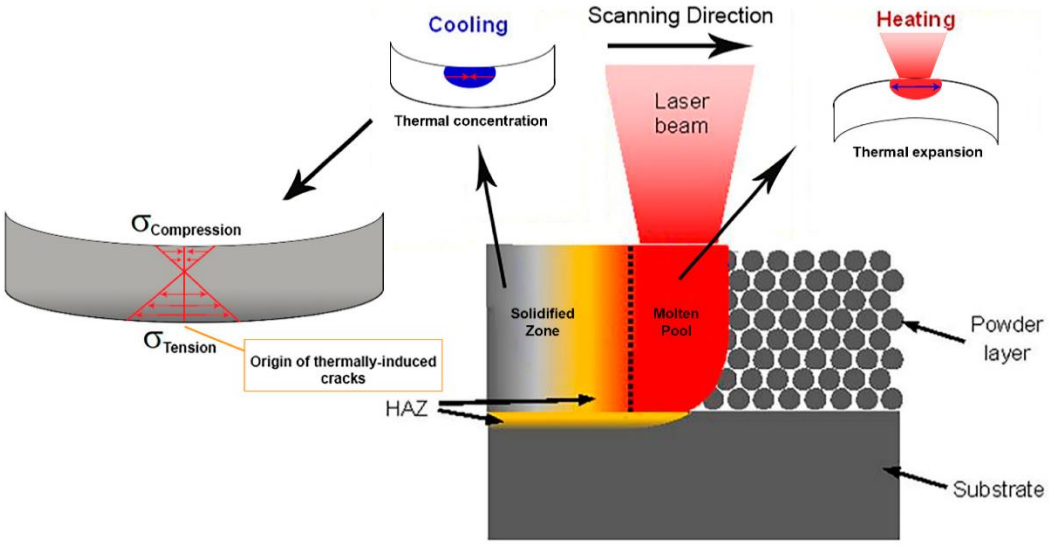

Figure 3-7 Thermal stresses in SLM and origin of thermally induced cracks (adapted from [24]).

Figure 3-8 shows the cracking behavior of some of the parts in the design matrix that already featured acceptable densities. As it is evident from the Figure 3-8, preheating has proved to be effective in eliminating the cracks. Preheating the base plate to reduce the steep thermal gradients has been implemented by many researchers. Kempen et al. [11] used a preheating of 200°C to reduce the extent of cracking and delamination in the case of M2 HSS tool steel. Martens et al. [17] investigated the effect of preheating temperatures of 100, 200, 300, and 400°C on the SLM-fabricated H13 parts. According to their findings, the residual stresses evolve from compressive at low preheating temperatures to tensile stresses as the preheating temperatures increases. However, better mechanical properties including ultimate tensile strength comparable to those of conventionally fabricated and heat-treated parts were achieved. Krell et al. [25] also investigated the effect of preheating on the properties of SLM-produced H13 tool steel. They found a significant reduction in

cracking density by applying preheating of 300°C. Their results revealed that increasing the preheating temperature will lead into more oxygen uptake in the final parts, which might result in weakening of the mechanical properties.

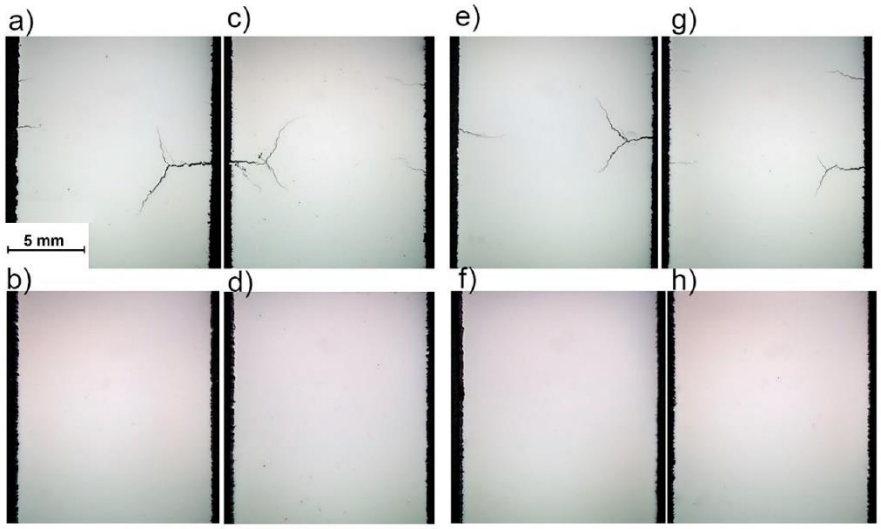

Figure 3-8 Effect of preheating of 200 °C on dense parts: (a) Sample C8; (b) sample PC8; (c) sample C10; (d) sample PC10; (e) sample C9; (f) sample PC9; (g) sample C11; and (h) sample PC11.

The total strain developed in the cooling phase has four major contributors, namely elastic (ε_e), plastic (ε_p), thermal [$\varepsilon_T = \alpha\,(T - T_0)$] in which α is the coefficient of thermal expansion; T is the local temperature; and T_0 is the initial temperature, and phase transformations (ε_{PT}) [26]. Application of a preheating temperature reduces the temperature difference at each point resulting the reduction of thermal contribution to the total strain, and ultimately mitigating the residual stresses. The results of the current study revealed that the direction of the density and thermally-induced cracking improvements are opposite. At laser power of 100 W, little, if any, cracks are present but the material suffers from severe porosity. On the other hand, at higher laser powers, the material possesses good density, while suffering

from aggravated cracking. Preheating of the build plate proved to be a good way of widening the safe processing windows of H13 tool steel.

3.3.3 Surface roughness

Surface roughness is one of the most important features of complex geometries produced by AM. There are two main mechanisms bringing about rough surfaces in additively manufactured parts. “Staircase effect” is one of the mechanisms that finds its roots in the stepped approximation by layers of curved and inclined surfaces in complex geometries [27]. In the current study, because the geometry of the build parts are upright coupons, this effect is absent. The other mechanism, which is related to process parameters, is the insufficient melting of the powder particles on the bed and balling phenomenon [28, 29]. Surface roughness is measured using a profilometer or analyzing the surface morphology using SEM. On the surface, the height of a peak or the depth of a valley (f_n) is measured at N locations along the profile length L. Consequently, the average surface roughness (R_a) is calculated using Eq.2 as [30]:

$$R_a = \frac{1}{N}\sum_{i=1}^{N}|f_n| \qquad \text{Eq.2}$$

Figure 3-9 shows the surface roughness measurements of the samples presented in the design matrix. Samples A3, A2 and A4 (Table 3-2) suffer from severe balling that leaves big lumps of solidified material on the surface, leading into aggravation of surface roughness. The balling effect and insufficient melting of powders in the case of the SLM-parts processed with a laser power of 100 W at all the scanning speeds used seem to be responsible for featuring rough surfaces. Increasing laser power, particularly from 200 to

300 W, at all hatch spacing and scanning speeds led into mitigation of surface roughness, which is in agreement with the literature [31, 32].

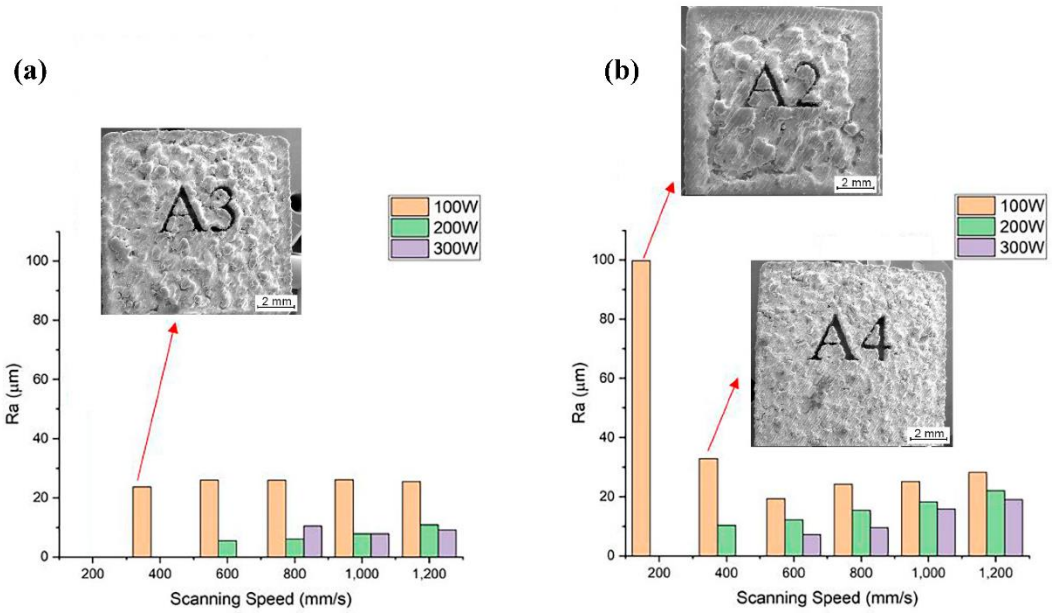

Figure 3-9 Surface roughness measurements: (a) h = 80 µm and (b) h = 120 µm.

The decrease in the average roughness may be attributed to the increase in heat input provided by the laser power which in turn yields a wider melt pool causing a better overlap between adjacent scan tracks. Figure 3-10 shows surface texture scans along with the SEM image and the surface scan of the top surfaces of the samples A9, B9, and C9 built at constant scanning speed of 1000 mm/s and hatch spacing of 80 µm, and a laser power of 100, 200, and 300 W, respectively. The best surface roughness achieved is 6.1 µm. The further improvement of the surface roughness is limited by the large un-melted powders left on the surface (Figure 3-10(e,h)). As may be seen from Figure 3-10, increasing the laser power, when the other process parameters are kept unchanged, generally tends to

decrease the surface roughness of SLM-manufactured samples. Preheating of 200°C used in this study has no substantial effect on quality of the obtained surfaces.

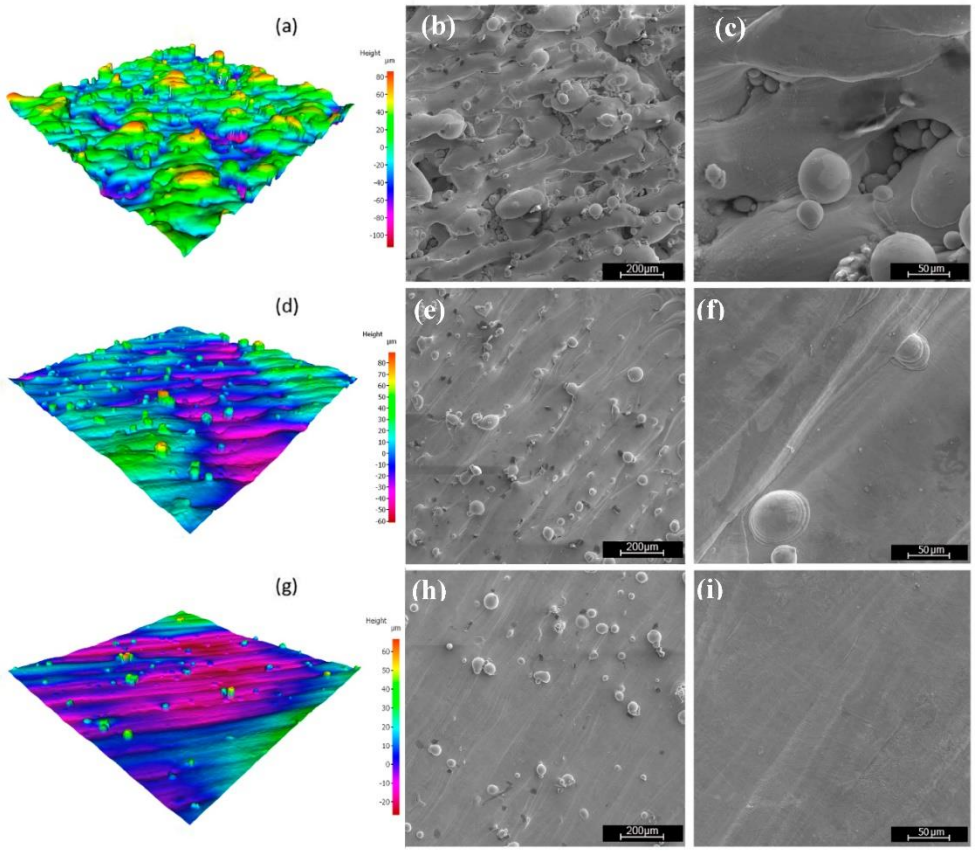

Figure 3-10 Surface texture scan and SEM micrographs: (a–c) Sample A9, (d–f) sample B9, and (g–i) sample C9.

3.3.4 Microstructural analysis

Figure 3-11 depicts the XRD analysis of two SLM-manufactured samples as follows: Sample C9 without preheating (Figure 3-11(a)) and sample PC9 with preheating of 200 °C (Figure 3-11(b)) under the same processing parameters. Both the samples possess a volumetric energy density of 62.5 J/mm^3. Figure 3-11(c)shows the XRD analysis of the as-

cast sample, used for a comparison. For the XRD testing, the cross section of the samples along the build direction were polished and then examined.

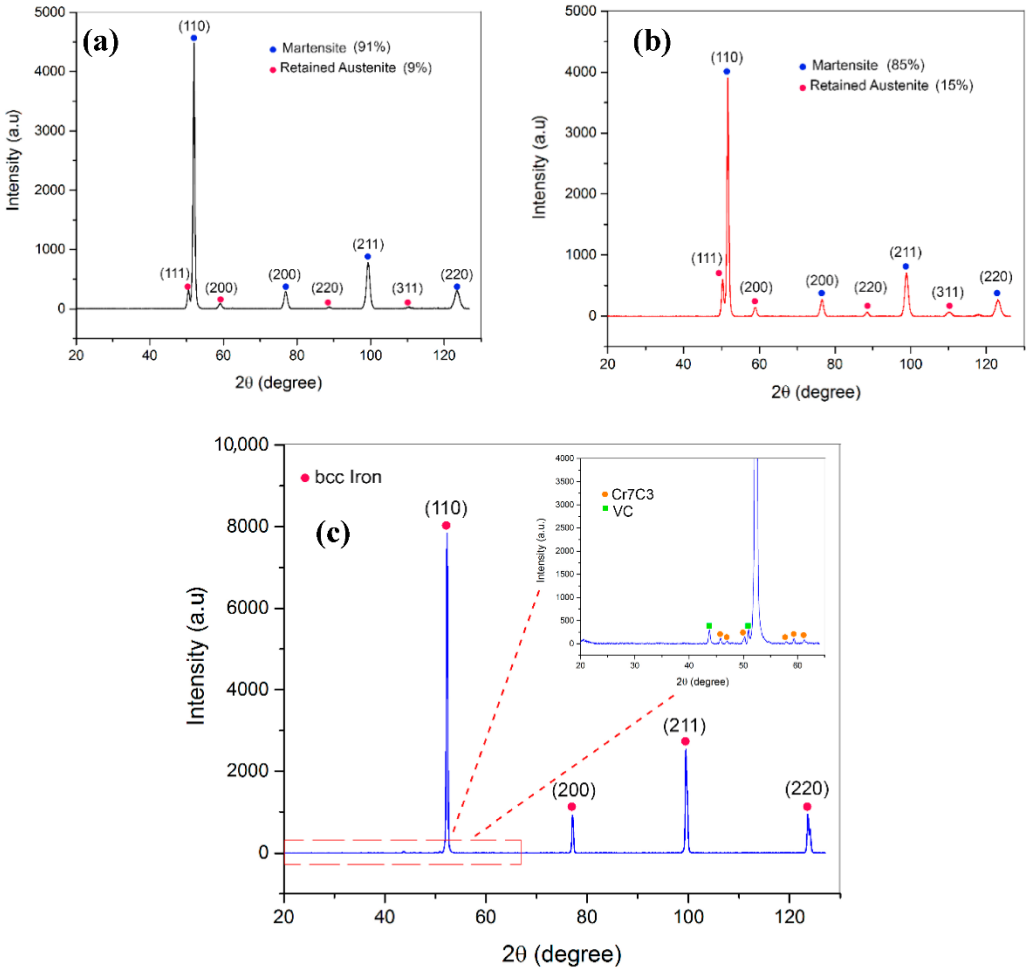

Figure 3-11 XRD analysis: (a) Sample C9 without preheating; (b) sample PC9 with 200 °C preheating; and (c) as-cast sample.

It was found that the as-cast sample contains predominantly α-Fe with vanadium and chromium carbides. Generally, all the SLM-fabricated parts across the design matrix revealed the same phases. The microstructures of as-built samples contain martensite (a = 2.8 Å) as the dominant phase and some amount of retained austenite (a = 3.6 Å) for both printing conditions, with and without preheating. This is consistent with the observations

from the previously studies [17, 33]. Using the Rietveld method, the phase quantification of the XRD patterns was performed. The results showed that the retained austenite content in the matrix of the sample PC9 built with a preheating of 200 °C was about 66% higher than that measured in the matrix of the sample C9 processed without preheating. This may be related with the less fast quenching being occurred with an application of preheating process. Disappearance of the carbides may be attributed to the high cooling rates experienced during the SLM process that significantly restricts the diffusion mechanisms, thereby impeding precipitation of the carbides. However, in conventionally processed H13, these carbides are evident inside and along grain boundaries.

Microstructural analysis was performed on the as-built parts fabricated with the SLM process. Optical microscope observation of etched samples was performed to reveal the melt pool shapes and laser tracks along the build direction (Z direction), as shown in the (Figure 3-12(a)). There are some oddly shaped melt pools in the micrograph due to scanning direction changes 67° in each layer and therefore the micrograph shows the intersection of the melt pool with the sectioning plane along the build direction. The melt pool cross-sectional view reveals curved morphology which reflects the laser's Gaussian energy profile. Figure 3-12(b–d) illustrate the SEM micrographs of the etched sample through which two types of crystals, produced during the solidification process, may be seen. These are equiaxed (Figure 3-12(c)) and columnar crystals (Figure 3-12(c)), irregularly distributed within the structure.

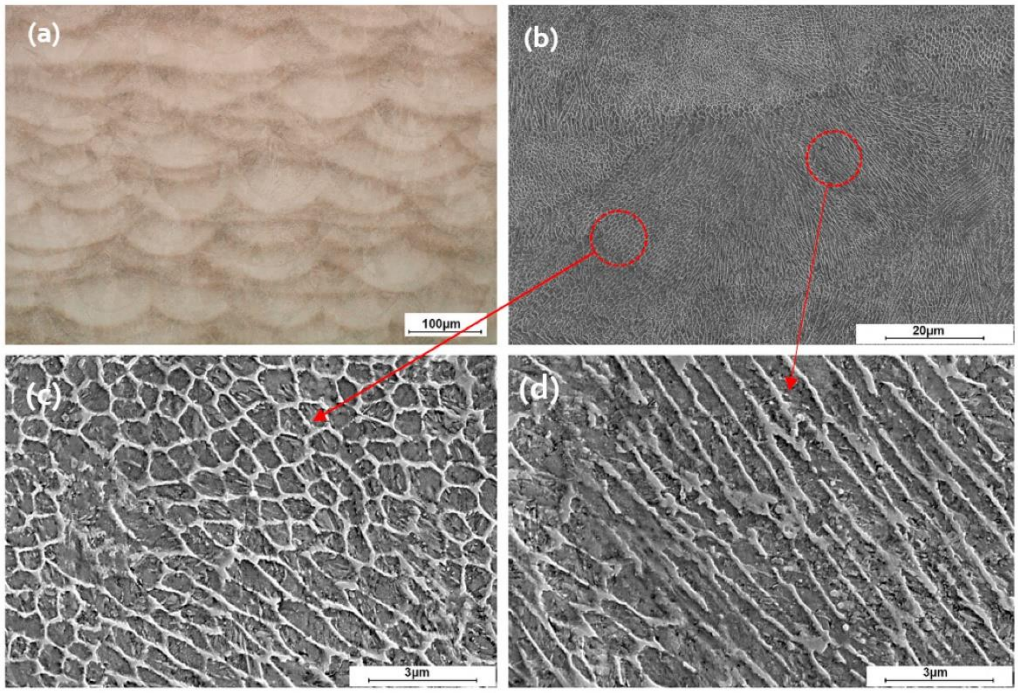

Figure 3-12 Microstructure of SLM-processed sample in as-built condition along the build direction: (a) Optical microscopy of a cross-section; (b) SEM micrograph of a melt-pool; (c) higher magnification of an area showing fine equiaxed dendrite; and (d) higher magnification of an area representing columnar dendrite.

XRD and EBSD measurements were carried out to characterize the phases present in the microstructure. Generally, two phases (bright and dark) may be seen. The bright phase was identified to be primarily fcc (austenite) and the darker phase bcc-structured which is martensite. A dominant cell-like morphology is observed for both preheated and non-preheated samples. The size of these bcc-structures cells varies from 600 nm up to 1 µm, whereas the wall thickness of the fcc structures varies from 100 to 200 nm. In some regions in the melt pool, due to different thermal regime, these cell-like microstructures get stretched (Figure 3-12(d)) along the direction of maximum thermal gradient. The results of the microstructural investigation revealed that, other than the amount of martensite and

retained austenite, the preheating process of 200°C has no significant effect on the cellular structure in comparing with that of the non-preheated samples. These results are consistent with those findings on the processing of H13 tool steel cited in [17, 25]. Considering high cooling rates experienced in SLM, it is expected to have a fully martensitic microstructure at room temperature. However, a considerable amount of retained austenite is detected using XRD and EBSD methods. Two mechanisms may be adapted to explain the presence of some amount of austenite in the structure of SLM-processed H13. The first is given by Holzweissig et al. [33]. They postulated that SLM process is similar to Quench and Partitioning (Q + P) process in which the martensitic structure evolves as a result of high cooling rates associated with the SLM process. Upon melting of next layer, the previously solidified microstructure gets austenitized and quenched again. In this process, due to diffusion of carbon, which is a strong austenite stabilizer, some austenite is stabilized and remains in the room-temperature microstructure. The second mechanism, suggested by Zhong et al. [34], for the case of SLM-manufactured 316 L stainless steel, is related to a segregation during solidification that accounts for local stabilization of austenite in the microstructure.

In order to identify the elemental composition of the formed morphologies of SLM-processed H13 tool steel, SEM-EDS analysis was performed on six points, as shown in Figure 3-13(a). Three points were located inside the cells (1, 3, and 5) and the other three were on the walls of the cells (2, 4, and 6). Table 3-3 presents the composition of the measured points. Figure 3-13(b–f) illustrates the EDS maps of the major alloying elements, C, Si, V, Mo, and Cr, respectively.

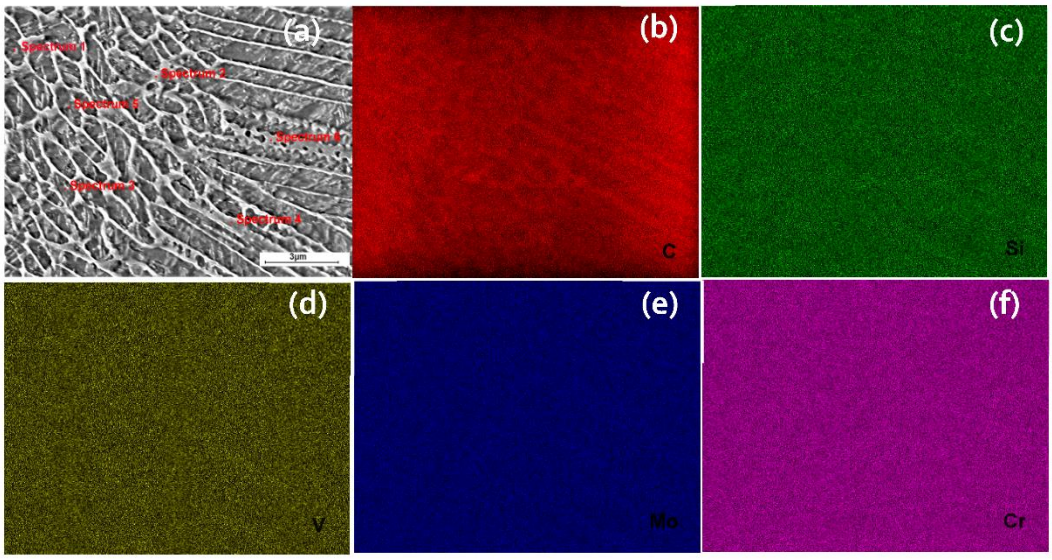

Figure 3-13 Energy-dispersive X-ray spectroscopy (EDS) maps of the formed morphologies along the build direction: (a) Location of points; (b) C element; (c) Si element; (d) V element; (e) Mo element; and (f) Cr element.

Table 3-3 EDS analysis, composition (wt %) of the tested points.

Element	*Point 1*	*Point 2*	*Point 3*	*Point 4*	*Point 5*	*Point 6*
C	6.17	7.42	5.84	7.58	6.17	7.24
Si	0.92	1.01	1.01	0.9	0.99	1.02
V	1.06	1.00	1.13	1.01	0.95	1.14
Mo	1.29	1.53	1.61	1.62	1.69	1.67
Cr	5.15	5.28	5.12	5.4	5.09	5.34
Fe	85.41	83.76	85.29	83.49	85.11	83.59
Total	100	100	100	100	100	100

As it is evident from the Figure 3-13(b) and Table 3-3, the concentration of C is much higher in the cell walls, where the austenite phase is present, than inside the cell. Such a

high carbon concentration may explain the stabilization of austenite phase at room temperature, since C is a strong austenite stabilizer. The other alloying elements (Si, V, Mo, and Cr) are seen from Figure 3-13(c–f) and Table 3-3to partition about equally inside the cells and in the walls of the cells.

Figure 3-14(a,b) depict the color maps obtained by electron-backscatter diffraction (EBSD) from cross sections along the build direction (Z) for the samples PC9 and C9 (Table 3-2). Figure 3-14(c,d) show the phases detected by EBSD over a relatively small part of the as-built samples (scan step size: 150 nm). As discussed earlier, a considerable amount of retained austenite is present in the SLM-processed H13 tool steel. Comparing the morphologies of the retained austenite shown in Figure 3-12 and Figure 3-14, it is evident that the morphology in the Figure 3-12 is continuous and that in Figure 3-14 is found to be discontinuous. The reason behind it is the low amount of certainty index (CI) in the unprocessed data that is related to the high density of dislocations in the microstructure limiting the quality of the Kikuchi patterns. The post-processing of data excludes the data points with low CI, leaving the morphologies discontinuous in the phase maps. The cross sections show a fine grain structure with an average size of 0.52 μm as a result of the rapid solidification. The microstructure when viewed from the side, shows epitaxial columnar grains oriented along the SLM building direction. These grains formed during the solidification of the previous layer elongated toward the building direction of heat conduction through the laser scan with the same orientation. Rotation of the scanning direction by 67° usually breaks up the defined epitaxial columnar structure [35].

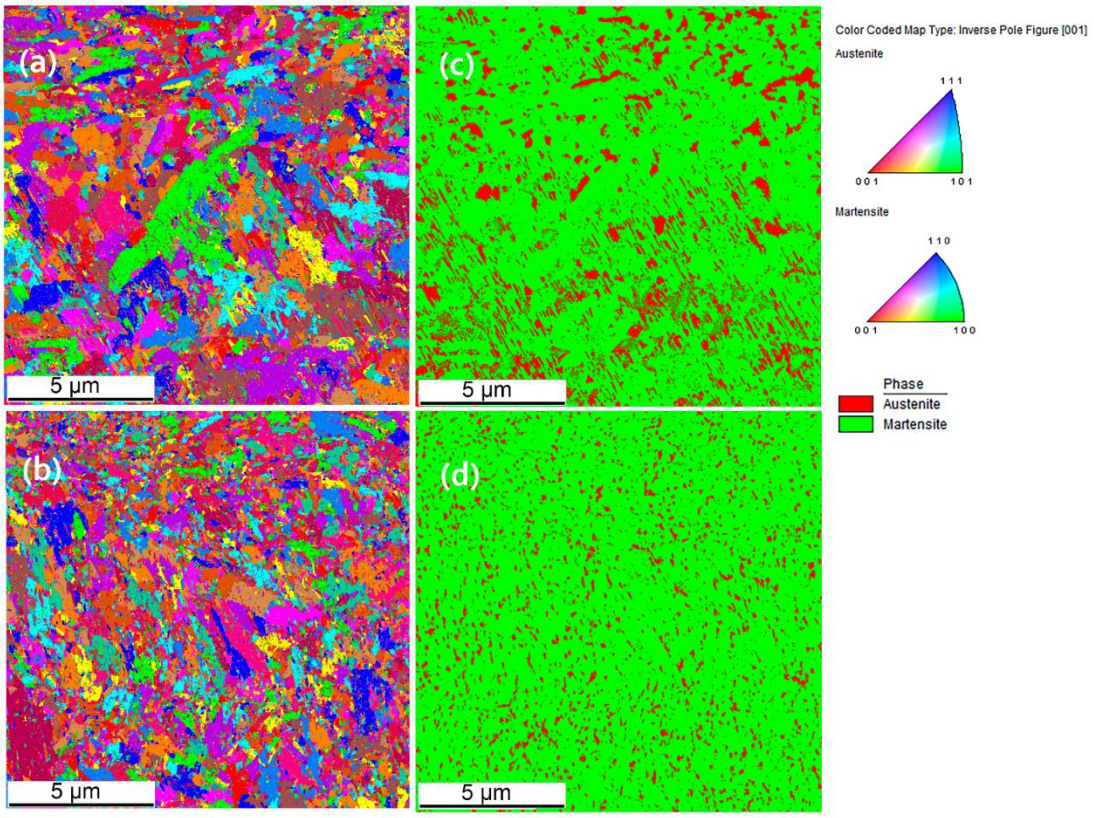

Figure 3-14 Electron backscatter diffraction (EBSD) grain orientation maps of the sections along the build direction: (a) Sample PC9 and (b) sample C9. Spatial distribution of phases: (c) Sample PC9 and (d) sample C9.

3.3.5 Hardness

Hardness is one of the most commonly used for the characterization of mechanical properties because hardness measurements are quick, relatively inexpensive and provide insight to other properties such as yield strength and wear resistance [36, 37]. Micro-hardness tests were conducted on the samples representing different process parameters. No significant difference was found in the hardness of the samples and its value ranged from minimum of 650 to 689 $HV_{0.2}$. This may be due to the high cooling rates during the

process that leaves the martensitic phase in large portions. Apart from that, the size of the grains also plays a role in the high and uniform values of hardness. Such fine and uniform structures reflect in little differences in the microhardness values of the as-built samples. Figure 3-15 shows the microhardness indentations made in the top most layer of the PC9 sample, targeting the height of the melt pool (Figure 3-15(a)), re-melted region between two adjacent melt-pools (Figure 3-15(b)), and heat affected zone (HAZ) region (Figure 3-15(c)). On the average, the whole set of points yields 618 $HV_{0.2}$ (~56 HRC). The uniform distribution of the hardness in the as-built samples can be attributed to the high amount of martensite phase.

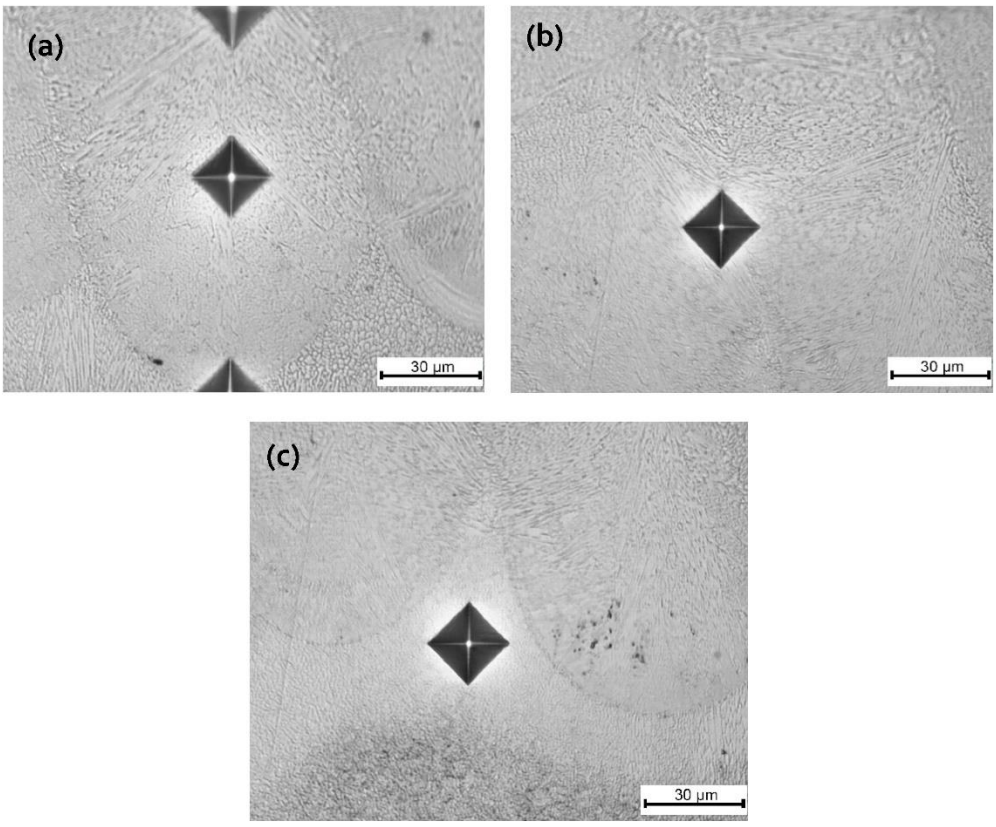

Figure 3-15 Vickers microhardness indentations in the topmost layer of PC9 sample along the build direction: (a) Along the melt-pool; (b) re-melted boundary; and (c) heat affected zone (HAZ).

Local mechanical properties including nano-hardness and Young's modulus of the as-built samples were measured via nano-indentation. The indenter was a Berkovich diamond three-sided pyramid with a nominal angle of 65.3° and a radius of about 100 nm. The maximum load used was 50 mN. The loading and unloading rate were 100 mN/min and the dwell time was 5 s. The nano-indenter precisely measured the continuous displacement and force of the indenter towards and into the specimen, with displacement and force errors about 1 nm and 1 μN, respectively. The hardness and modulus values were calculated from the load–displacement curve for each indentation using Eq.3 [36]:

$$E_r = \frac{S\sqrt{\pi}}{2\beta\sqrt{A}} \ , \ \frac{1}{E_r} = \frac{1-v^2}{E} + \frac{1-v_i^2}{E_i} \qquad \text{Eq.3}$$

where S, is the slope of the unloading curve at the maximum depth; E_r is the reduced modulus; E and v are the Young's modulus and Poisson ratio of the material, respectively, and E_i and v_i are those for the indenter tip; β is a constant dependent on the indenter geometry (β = 1.034 for a Berkovich indenter); A is the projected contact area, which is a function of contact depth ($A = 24.5\ h^2_c$). The relationship between contact depth h_c and the maximum depth, h_{max} is given in Eq.4 as:

$$h_c = h_{max} - h_d = h_{max} - \varepsilon\frac{P_{max}}{S} \qquad \text{Eq.4}$$

where h_d is the depth of elastic deflection, ε is a constant dependent on the indenter geometry, and P_{max} is the peak load. The hardness H defined as the applied load divided by the projected area of contact can be calculated according to Eq.5 as:

$$H = \frac{P_{max}}{A(h_c)} \qquad \text{Eq.5}$$

Figure 3-16 shows the distribution of nano-hardness and Young's modulus in the designated area in the picture located at the surface of the sample PC9 (P = 300 W, v = 1000 mm/s, and h = 80 µm) processed with a preheating temperature of 200 °C. The map contains 100 indentations. As seen in the figure, the greatest nano-hardness values were obtained at the top layers of the sample. This may be attributed to the formation of hard martensite in each newly solidified layer due to high cooling rates during SLM process. The hardness significantly decreased when moving away from the top surface and the lowest hardness was found to be 575. Such a decrease in hardness may be related to the tempering of martensite. These findings are in a good agreement with those found by Mertens et al. [17].

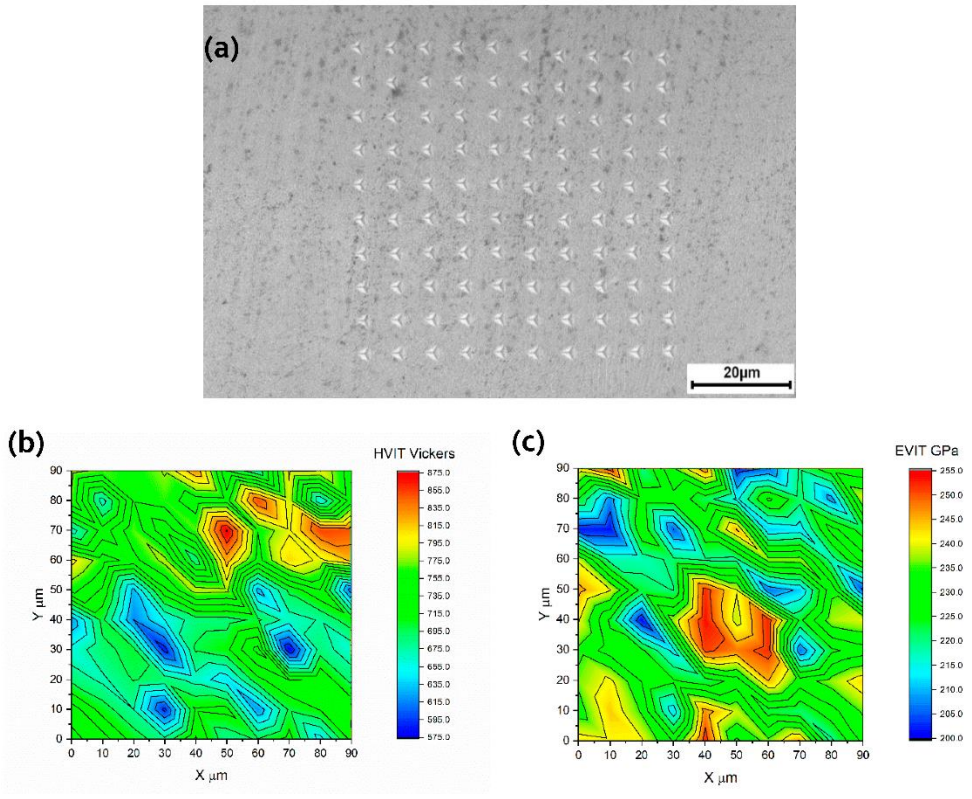

Figure 3-16 Mechanical properties of the PC9 sample along the build direction: (a) Indention array; (b) distribution of nano-hardness; and (c) Young's modulus distribution.

3.4 Conclusions

In this study, samples of H13 tool steel with a size of 10 × 10 × 15 mm^3 were SLM-manufactured using a laser power of 100, 200, and 300 W; scanning speed of 200, 400, 600, 800, 1000, and 1200 mm/s; and hatch spacing of 80 and 120 µm. A constant layer thickness of 40 µm, 67° scanning rotation between subsequent layers, and a stripe scanning strategy were maintained during the process. A preheating process of 200 °C was considered. The main conclusions can be drawn as follows:

(i) The relative density of the as-built material, processed with and without preheating of 200 °C, increased non-linearly with increasing the volumetric energy density up to a value of about 60 J/mm^3 and then no significant increase was seen.

(ii) The relative densities of the samples processed with preheating were relatively higher when compared with those of the non-preheated samples; a relative density of 99.7% was achieved.

(iii) Application of the preheating process not only enhanced the relative density, but also it helped in eliminating the thermally-induced cracks. In fact, preheating of the base plate broadens the safe processing window of SLM-manufactured H13 tool steel.

(iv) The best surface roughness achieved in this work was 6.1 µm, corresponding to the sample B5 (P = 200 W, v = 600 mm/s, and h = 80 µm). Due to un-melted powders, further improvements in the surface roughness were not possible and parts need to go through post-processing in case better finishes are required.

(v) The microstructure of the as-built samples showed fine equiaxed cellular-dendritic structure (600 nm up to 1µm). All the samples studied showed both a dominant

martensite and varying retained austenite contents. The preheating temperature of 200 °C led to an increase in the amount of retained austenite. For example, the amount of retained austenite in a preheating sample PC9 was found to be 66% higher when compared to that of the non-preheated sample C9.

(vi) The microhardness of the as-built samples was found to vary from 650 to 689 HV 0.2, which is comparable to a conventionally produced H13 tool steel.

3.5 References

[1] M. Brandt, Laser additive manufacturing: materials, design, technologies, and applications, Woodhead Publishing2016.

[2] C.Y. Yap, C.K. Chua, Z.L. Dong, Z.H. Liu, D.Q. Zhang, L.E. Loh, S.L. Sing, Review of selective laser melting: Materials and applications, Applied physics reviews 2(4) (2015) 041101.

[3] M. Mazur, M. Leary, M. McMillan, J. Elambasseril, M. Brandt, SLM additive manufacture of H13 tool steel with conformal cooling and structural lattices, Rapid Prototyping Journal (2016).

[4] M. Mazur, P. Brincat, M. Leary, M. Brandt, Numerical and experimental evaluation of a conformally cooled H13 steel injection mould manufactured with selective laser melting, The International Journal of Advanced Manufacturing Technology 93(1-4) (2017) 881-900.

[5] A. Armillotta, R. Baraggi, S. Fasoli, SLM tooling for die casting with conformal cooling channels, The International Journal of Advanced Manufacturing Technology 71(1-4) (2014) 573-583.

[6] S.A. Khairallah, A.T. Anderson, A. Rubenchik, W.E. King, Laser powder-bed fusion additive manufacturing: Physics of complex melt flow and formation mechanisms of pores, spatter, and denudation zones, Acta Materialia 108 (2016) 36-45.

[7] J.H. Martin, B.D. Yahata, J.M. Hundley, J.A. Mayer, T.A. Schaedler, T.M. Pollock, 3D printing of high-strength aluminium alloys, Nature 549(7672) (2017) 365-369.

[8] C. Tan, K. Zhou, W. Ma, P. Zhang, M. Liu, T. Kuang, Microstructural evolution, nanoprecipitation behavior and mechanical properties of selective laser melted high-performance grade 300 maraging steel, Materials & Design 134 (2017) 23-34.

[9] J. Mutua, S. Nakata, T. Onda, Z.-C. Chen, Optimization of selective laser melting parameters and influence of post heat treatment on microstructure and mechanical properties of maraging steel, Materials & Design 139 (2018) 486-497.

[10] S. Bodziak, K.S. Al-Rubaie, L. Dalla Valentina, F.H. Lafratta, E.C. Santos, A.M. Zanatta, Y. Chen, Precipitation in 300 grade maraging steel built by selective laser melting: Aging at 510 C for 2 h, Materials Characterization 151 (2019) 73-83.

[11] K. Kempen, B. Vrancken, S. Buls, L. Thijs, J. Van Humbeeck, J.-P. Kruth, Selective Laser Melting of Crack-Free High Density M2 High Speed Steel Parts by Baseplate Preheating, Journal of Manufacturing Science and Engineering 136(6) (2014).

[12] F. Huber, C. Bischof, O. Hentschel, J. Heberle, J. Zettl, K.Y. Nagulin, M. Schmidt, Laser beam melting and heat-treatment of 1.2343 (AISI H11) tool steel–microstructure and mechanical properties, Materials Science and Engineering: A 742 (2019) 109-115.

[13] O. Hentschel, C. Scheitler, A. Fedorov, D. Junker, A. Gorunov, A. Haimerl, M. Merklein, M. Schmidt, Experimental investigations of processing the high carbon cold-work tool steel 1.2358 by laser metal deposition for the additive manufacturing of cold forging tools, Journal of Laser Applications 29(2) (2017) 022307.

[14] J. Sander, J. Hufenbach, L. Giebeler, H. Wendrock, U. Kühn, J. Eckert, Microstructure and properties of FeCrMoVC tool steel produced by selective laser melting, Materials & Design 89 (2016) 335-341.

[15] J. Boes, A. Röttger, C. Mutke, C. Escher, W. Theisen, Microstructure and mechanical properties of X65MoCrWV3-2 cold-work tool steel produced by selective laser melting, Additive Manufacturing 23 (2018) 170-180.

[16] R. Casati, M. Coduri, N. Lecis, C. Andrianopoli, M. Vedani, Microstructure and mechanical behavior of hot-work tool steels processed by Selective Laser Melting, Materials Characterization 137 (2018) 50-57.

[17] R. Mertens, B. Vrancken, N. Holmstock, Y. Kinds, J.-P. Kruth, J. Van Humbeeck, Influence of powder bed preheating on microstructure and mechanical properties of H13 tool steel SLM parts, Physics Procedia 83 (2016) 882-890.

[18] T. DebRoy, H.L. Wei, J.S. Zuback, T. Mukherjee, J.W. Elmer, J.O. Milewski, A.M. Beese, A. Wilson-Heid, A. De, W. Zhang, Additive manufacturing of metallic components – Process, structure and properties, Progress in Materials Science 92 (2018) 112-224.

[19] M. Yakout, A. Cadamuro, M. Elbestawi, S.C. Veldhuis, The selection of process parameters in additive manufacturing for aerospace alloys, The International Journal of Advanced Manufacturing Technology 92(5-8) (2017) 2081-2098.

[20] M.M. Attallah, R. Jennings, X. Wang, L.N. Carter, Additive manufacturing of Ni-based superalloys: The outstanding issues, MRS Bulletin 41(10) (2016) 758.

[21] T. Peng, C. Chen, Influence of energy density on energy demand and porosity of 316L stainless steel fabricated by selective laser melting, International Journal of Precision Engineering and Manufacturing-Green Technology 5(1) (2018) 55-62.

[22] H.D. Carlton, A. Haboub, G.F. Gallegos, D.Y. Parkinson, A.A. MacDowell, Damage evolution and failure mechanisms in additively manufactured stainless steel, Materials Science and Engineering: A 651 (2016) 406-414.

[23] N.T. Aboulkhair, N.M. Everitt, I. Ashcroft, C. Tuck, Reducing porosity in AlSi10Mg parts processed by selective laser melting, Additive Manufacturing 1 (2014) 77-86.

[24] C. Fu, Y. Guo, 3-dimensional finite element modeling of selective laser melting Ti-6Al-4V alloy, 25th Annual International Solid Freeform Fabrication Symposium, 2014, pp. 1129-1144.

[25] J. Krell, A. Röttger, K. Geenen, W. Theisen, General investigations on processing tool steel X40CrMoV5-1 with selective laser melting, Journal of Materials Processing Technology 255 (2018) 679-688.

[26] J.J. Yan, D.L. Zheng, H.X. Li, X. Jia, J.F. Sun, Y.L. Li, M. Qian, M. Yan, Selective laser melting of H13: microstructure and residual stress, Journal of Materials Science 52(20) (2017) 12476-12485.

[27] K. Mumtaz, N. Hopkinson, Selective laser melting of Inconel 625 using pulse shaping, Rapid Prototyping Journal (2010).

[28] D. Gu, Y. Shen, Balling phenomena in direct laser sintering of stainless steel powder: Metallurgical mechanisms and control methods, Materials & Design 30(8) (2009) 2903-2910.

[29] J.-P. Kruth, L. Froyen, J. Van Vaerenbergh, P. Mercelis, M. Rombouts, B. Lauwers, Selective laser melting of iron-based powder, Journal of materials processing technology 149(1-3) (2004) 616-622.

[30] G. Strano, L. Hao, R.M. Everson, K.E. Evans, Surface roughness analysis, modelling and prediction in selective laser melting, Journal of Materials Processing Technology 213(4) (2013) 589-597.

[31] T. Yang, T. Liu, W. Liao, E. MacDonald, H. Wei, X. Chen, L. Jiang, The influence of process parameters on vertical surface roughness of the AlSi10Mg parts fabricated by selective laser melting, Journal of Materials Processing Technology 266 (2019) 26-36.

[32] A.H. Maamoun, Y.F. Xue, M.A. Elbestawi, S.C. Veldhuis, Effect of selective laser melting process parameters on the quality of al alloy parts: Powder characterization, density, surface roughness, and dimensional accuracy, Materials 11(12) (2018) 2343.

[33] M.J. Holzweissig, A. Taube, F. Brenne, M. Schaper, T. Niendorf, Microstructural Characterization and Mechanical Performance of Hot Work Tool Steel Processed by Selective Laser Melting, Metallurgical and Materials Transactions B 46(2) (2015) 545-549.

[34] Y. Zhong, L. Liu, S. Wikman, D. Cui, Z. Shen, Intragranular cellular segregation network structure strengthening 316L stainless steel prepared by selective laser melting, Journal of Nuclear Materials 470 (2016) 170-178.

[35] L. Thijs, M.L.M. Sistiaga, R. Wauthle, Q. Xie, J.-P. Kruth, J. Van Humbeeck, Strong morphological and crystallographic texture and resulting yield strength anisotropy in selective laser melted tantalum, Acta Materialia 61(12) (2013) 4657-4668.

[36] H. Attar, S. Ehtemam-Haghighi, D. Kent, I. Okulov, H. Wendrock, M. Bönisch, A. Volegov, M. Calin, J. Eckert, M. Dargusch, Nanoindentation and wear properties of Ti and Ti-TiB composite materials produced by selective laser melting, Materials Science and Engineering: A 688 (2017) 20-26.

[37] J.S. Keist, T.A. Palmer, Development of strength-hardness relationships in additively manufactured titanium alloys, Materials Science and Engineering: A 693 (2017) 214-224.

Chapter 4

Part Deflection and Residual Stresses in Laser Powder Bed Fusion of AISI H13 Tool Steel

Complete Citation:

Morteza Narvan, Ali Ghasemi, Eskandar Fereiduni, Stephen Kendrish, Mohamed Elbestawi " Part Level Deflection and Residual Stresses in Laser Powder Fusion of AISI H13 Tool Steel." *Materials & Design journal*, accepted.

Abstract

This study aims at a comprehensive investigation of the residual stresses in laser powder bed fusion processing of H13 tool steel through experiment and part-level simulation. Twin-cantilever beams and cubic coupons were printed in a wide range of process parameters to characterize the nature of residual stresses and contributing factors under preheated and non-preheated conditions. The residual stresses were assessed using X-ray diffraction method (XRD) as a direct way of getting the residual stress figures at distinct spots and along the depth of cubic coupons. Moreover, the level of beam deflection, as an indication of the magnitude of residual stresses, were both measured and simulated to gain an insight into the accuracy of the part-level simulation. The XRD and beam deflection measurement results revealed the significant role of martensitic phase transformation, process parameters, densification level, and preheating condition on the final residual stress regime and consequently beam deflections. Neglecting the martensitic phase transformation and defects in the deflection modelling introduced a discrepancy between the predictions and experimental measurements. The knowledge gained from the microstructure and residual stress characterizations unraveled that 200°C of preheating eliminates not only the cracks but also the need for stress-relief post-processing.

Keywords:

Laser powder bed fusion; H13 tool steel, residual stress, deflection, martensitic phase transformation, XRD analysis.

Acknowledgment:

The XRD measurements in this research study were supported and performed in American Stress Technologies Inc. We would like to thank our collaborators from American Stress Technologies Inc., especially Jonathan Mohan, who provided insight and expertise that greatly assisted the research.

Graphical Abstract:

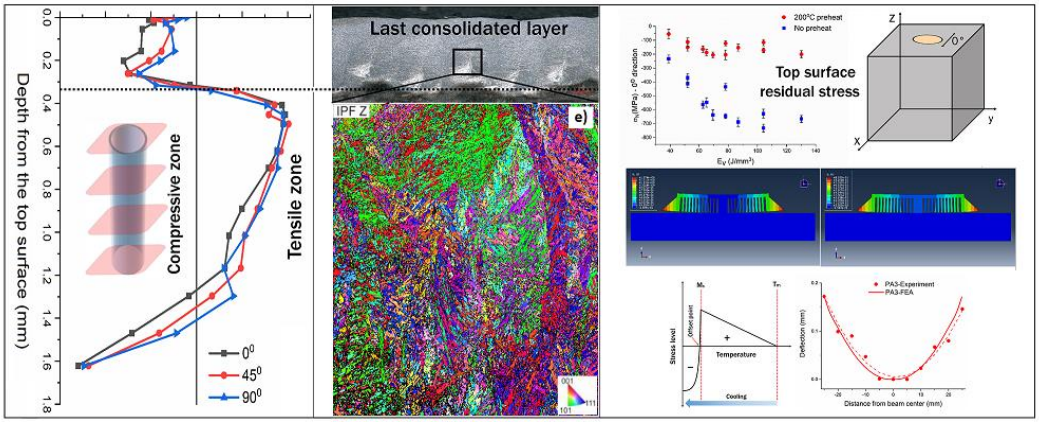

4.1 Introduction

Tool steels are considered as novel engineering alloys with tailorable properties, meeting a part of the growing industrial demands. AISI H13 tool steel, in specific, is a Cr-Mo hot work tool steel that has found its way in a wide variety of technological fields owing to its high wear resistance, outstanding thermal fatigue stability, superior strength at elevated temperatures and cost advantages [1-4]. The excellent balance of these properties has introduced H13 tool steel as a prime candidate in many applications including, plastic injection molding, die casting, and hot-extrusion industries [5-9]. To meet these service requirements, H13 components need to be free from not only defects but also the tensile residual stress. While defects adversely affect the mechanical properties by acting as crack nucleation sites, the tensile residual stress increases the overall stress applied to the component, which leads to the premature failure during static and dynamic loadings [10-12].

Although the influence of conventional processing and post-processing routes on the densification level, residual stress, and properties of H13 alloy has been intensively explored, developed, and documented in the literature, fabrication of parts with complicated geometries as well as fine features is difficult or impossible through these techniques [13, 14]. This can be solved by the application of powder bed fusion additive manufacturing (PBF-AM) techniques as the production method. Laser powder bed fusion (LPBF), with a PBF nature, is the most promising AM technique, which has drawn a great deal of attention in recent years for fabricating complex shape, custom-designed, and cost-effective components through a layer-by-layer manner [15-18]. However, the development of thermal stresses caused by the temperature gradient during the sample built up is

believed to be one of the most important obstacles toward the commercialization of the LPBF-manufactured components [19].

The underlying concept behind the formation of thermal stress can be explained by considering the formation of a random track during the LBPF process (Figure 4-1). As it is evident, a localized laser beam melts the powder bed along a specific line to create a single track having a reasonable overlap with the adjacent track and the previously consolidated layer. During the heating stage and formation of the melt pool, not only the temperature of the area underneath the laser beam but also the temperature of the surrounding material increases, since the formation of the melt pool takes place in a conductive metallic medium [20]. During the cooling stage (Figure 4-1(b)), the newly consolidated track shows a higher contraction propensity than the surrounding area owing to its larger temperature drop. However, the contraction of the consolidated track is restrained by the cooler regions further away from the track (i.e., adjacent tracks and layers) due to the lower likelihood of contraction caused by their lower temperature. This leads to the creation of a thermally-induced internal tensile stress opposing the further contraction of the solidified track, which cannot be dissipated since the track is in the solid form [21, 22]. The level of the stress at ambient temperature is known as the "residual stress" which is usually in the order of the yield strength of the material.

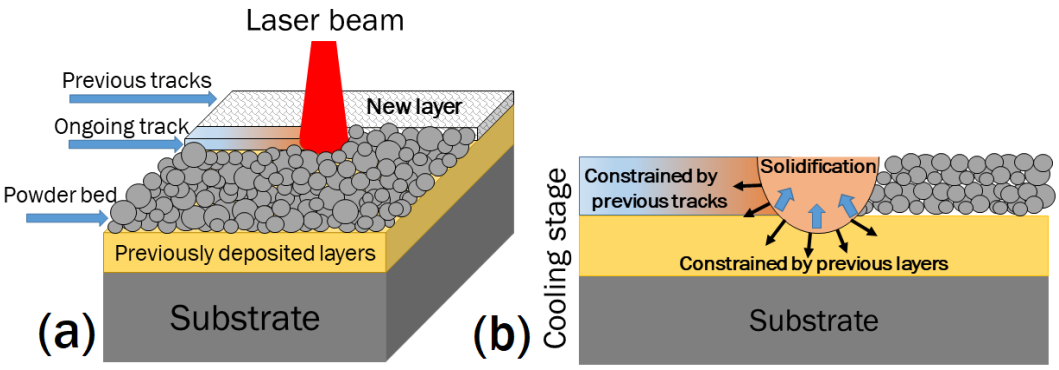

Figure 4-1 The overview of the LPBF process. The development of tensile thermal stresses during the cooling stage due to the presence of constraints is shown in (b).

The developed thermal stresses, coupled with the metallurgical factors, make the LPBF processing of H13 tool steel rather difficult and challenging. To clarify, the rapid solidification of the localized melt pool during the LPBF process results in the formation of the non-equilibrium martensite phase with negligible plastic deformability in the microstructure of the H13 tool steel. Henceforth, the material fails to deform under the applied thermally-induced tensile stresses, and macro-cracks, known as "cold cracks," are formed [23, 24]. According to a previous research study conducted by the same authors [23], the formation of these cracks can be mitigated by preheating the build plate up to 200°C prior to the printing. However, still, the residual stresses are present, and the distortion may play a role depending on the scanning strategy, geometry, and height of the LPBF-fabricated component. Since the level of the residual stress is a dominant factor dictating whether or not the stress-relief treatment is required, its in-depth analysis and characterization are essential.

According to the literature, the analysis of the residual stresses developed in the LPBF-processed parts is carried out through experimental and numerical methods [25-28]. From the experimental standpoint, one of the efficient ways of investigating the magnitude of the

residual stresses is to print a beam geometry (e.g. cantilever or bridge) that would deflect upon cutting from specific locations, the magnitude of which is indicative of the magnitude of the residual stresses stored in the part during the LPBF processing [29, 30]. It is worth noting that although several other methods are also available to directly measure the magnitude of residual stresses, they all fail to present a comprehensive picture of the status of residual stresses on part level. Currently, experimental methods are facing expensive trial and errors through manipulation of the process variables to achieve a condition with minimal residual stresses. This implies high manufacturing costs [31]. Hence, predictive methods such as numerical studies are crucial to predict and control the residual stresses even at the design stage.

Thermo-mechanical modelling of AM processes is a useful tool to efficiently deal with these challenges in a cost-effective manner. AM process simulation is a multiscale problem in both time and space. The simulation scale and the solution fidelity can be controlled by choosing an appropriate time incrementation and mesh size. In general, there are two types of simulation at different ends of the fidelity spectrum: process-level simulations (high fidelity) versus part-level simulations (low fidelity). Detailed process-level simulations were performed on Iron-based alloys [27, 28, 32, 33] by using a small time increment and a fine mesh with at least one element per printing layer thickness and a few elements across an action zone where fusion occurs. Simulations in this scale capture the rapidly evolving temperature, and high-temperature gradients typically found within and near action zones and, thus, provide accurate predictions of both residual stresses and distortions. A process-level simulation can model detailed physics of AM processes and provide accurate results, but it typically has a high computational cost and can be affected by convergence difficulties due to the use of temperature-dependent nonlinear material properties under

rapidly changing temperature conditions. Moreover, the process-level simulations are currently restricted to scanning volume of 100 mm3 [34]. On the other hand, a part-level simulation is performed by appropriately averaging (lumping) the time sequence of events and using coarser meshes. For example, the model could have an element size that is a few times larger than the physical printing layer thickness and uses only one or several time increments for printing one element layer. Although the part-level simulations are accompanied by major simplifications, they enable part-level deflection analysis which is directly indicative of the magnitude of the residual stresses in the printed parts [30, 35].

While the literature lacks a systematic study on the residual stress characterization of H13 tool steel, other materials such as Ti-6Al-4V [35-38], AlSi10Mg [39-41], Ni-based superalloys [29, 42-44], Maraging steels [44, 45] have been widely investigated. However, the effect of the following factors still remains a vacancy in the literature:

(i) Process parameters: Most of the research studies have targeted the characterization of the residual stresses in parts manufactured by the optimum process parameters. Even when the effect of process parameters was concerned, a relatively narrow range of process parameters was investigated [21]. It is worth noting that a different combination of process parameters might lead to optimum parts in terms of densification level with different status of residual stresses that has been neglected in the literature. These facts clearly show the necessity of studying the residual stresses in a wide range of process parameters.

(ii) Defects and densification: With a few exceptions, the literature lacks a systematic study exploring the effect of cracks and porosities on the residual stress status and part-level deflections of the LPBF-manufactured parts. Although it is well known that the presence of porosities and cracks in the parts reduces the magnitude of the

residual stresses, their contribution in altering the residual stress regime has not been yet fully understood.

(iii) Phase transformations: One of the key contributors to the status of the residual stresses is the phase transformations which happen on a microscopic scale [46, 47]. Including such a phenomenon in the part-level simulations of residual stresses is computationally expensive. The majority of the research dealing with the simulation of the residual stresses has been done on materials featuring no phase transformations in which the simulation results underestimate those of the experiment. On the other hand, the potential of the part-level simulation methods to predict residual stresses and deflections in the case of the materials with high strain transformations (e.g., low-temperature martensitic transformation in high carbon steels) is still unknown.

This study aims at a systematic understanding of the cumulative residual stress profile in the LPBF-processed H13 tool steel with a part-level approach. ABAQUS software is utilized to obtain the temperature field during the LPBF process and calculate the resulting strain field by using a thermo-mechanical coupling model, the output of which is the beam deflection. An experimental methodology is applied to measure the resultant deflections and validate the model. The residual stresses are also directly measured on the top surface and along the depth of the printed components using the X-ray diffraction method, according to the ASTM E915-96/E1426-98 standard [48]. The link between the beam deflections and residual stress magnitude was established. The effect of a wide range of process parameters on the residual stresses and part-level deflection were studied, and the contribution of developed defects, including porosities and cracks, was highlighted. Moreover, the impact of preheating on the regime of the residual stress and magnitude of

beam deflections was scrutinized. The discrepancy between the experimental and numerical outcomes was attributed to the martensitic phase transformation in LPBF-processed H13 tool steel. By providing a comprehensive insight into the residual stress formation and important contributing factors, this research work reinforces the idea that the end-use H13 parts could be manufactured with no excessive post-processing by application of a suitable preheating temperature.

4.2 Materials and methods

4.2.1 LPBF process

The powder used in this research was gas atomized AISI H13 alloy with the particle size distribution, chemical composition, morphology and microstructure reported in [23]. As previously discussed, this study aims to investigate the effect of process parameters and preheating on the part-level beam deflection and the residual stress of LPBF manufactured test samples. For this purpose, two sets of samples, including cantilever beams and cubic coupons, were printed using various process parameters with or without preheating the substrate. Each set contained 12 cubic samples with a size of 10×10×10 mm^3 and 12 cantilever beams. As listed in Table **4-1**, the hatch spacing (h) and the powder layer thickness (t) were kept constant, while the laser power (P) and the scanning speed (v) were changed, leading into various volumetric energy densities (E_v) calculated based on Eq. 1 [49]:

$$E_v = \frac{P}{vht} \left(\frac{J}{mm3}\right) \quad \text{Eq. 1}$$

The same set of samples as those listed in Table 4-1 were also printed with the application of 200°C preheating to the build plate. The prefix "P" refers to these samples throughout this chapter.

The LPBF machine used in this study was EOSIN M280 equipped with a Yb-fiber laser with a spot size of 100 µm and a maximum power of 400 W. An atmosphere of N_2 gas was applied to reduce the oxygen content in the build chamber to less than 0.8%, hence reducing the oxidation during the melting process. Scanning of layers was conducted using a continuous laser mode according to a stripe hatching pattern alternating 67° between two successive layers, as illustrated in Figure 4-2. For the build with preheating, the preheating temperature was selected to be 200 °C based on [23] to avoid cracking.

Table 4-1 Process parameters employed in this study to fabricate test samples.

Sample	*P (W)*	*v (mm/s)*	*h (mm)*	*t (mm)*	*E_v (J/mm^3)*
A1	300	1000	0.12	0.04	62.5
A2	300	600	0.12	0.04	104.2
A3	300	800	0.12	0.04	78.1
B1	250	800	0.12	0.04	65.1
B2	250	600	0.12	0.04	86.8
B3	250	400	0.12	0.04	130.2
C1	200	800	0.12	0.04	52.1
C2	200	600	0.12	0.04	69.4
C3	200	400	0.12	0.04	104.2
D1	150	800	0.12	0.04	39.1
D2	150	600	0.12	0.04	52.1
D3	150	400	0.12	0.04	78.1

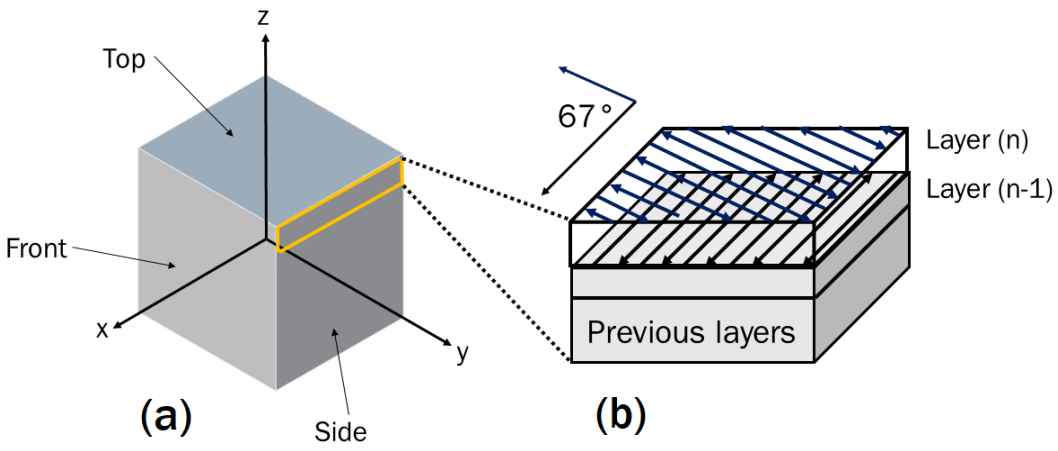

Figure 4-2 Schematic view of: (a) the stripe hatching pattern scanning strategy with 67° rotation between successive layers, and (b) the SLM-fabricated cubic parts showing x-y (top), y-z (front) and x-z (side) views.

Schematic illustration of the cantilever geometry is provided in Figure 4-3. As observed, twin cantilevers are printed with supports in the overhang area. Due to its geometry, the twin cantilever is highly sensitive to distortion, and therefore, can be adopted to investigate the magnitude of deflections and residual stresses in the additively manufactures components. The LPBF fabricated cantilevers were marked at 11 different points (5 on each side) after the printing process along the middle axis of each beam with a spacing of 5 mm between every two adjacent points. In order to visualize and measure the amount of deflection caused by the thermally induced residual stresses, the LPBF fabricated twin cantilevers were separated from the supports by wire electrical discharge machining. The difference between the Z positions of points before and after the separation of cantilevers from the substrate was measured to characterize the deflection magnitude along the length of the twin cantilevers. These measurements were made using the Zeiss Eclipse CMM equipment. The measurements were accomplished in accordance with the guidelines for

calibration and traceability as per the National Institute of Standards and Technology (NIST).

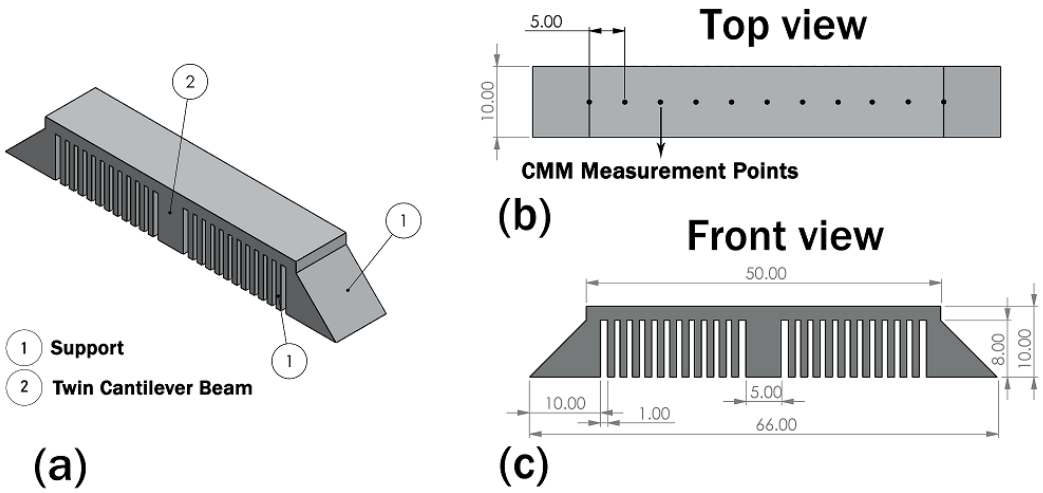

Figure 4-3 The geometry of a twin-cantilever beam (all dimensions are in mm) implemented to study the beam deflection.

4.2.2 Residual stress

The residual stress of the cubic samples was measured using X-ray Diffraction (XRD) on a Stresstech Xstress DR45 diffractometer equipped with a Cr-K_α radiation source, tube power of 3 KeV at 9 mA, and the exposure time of 0.1 s. Equipment used a modified χ as the measurement geometry, and the exposures were made at 4 tilts in both the positive and negative ψ directions. The residual stress measurements were carried out at a spot located at the center on the top surface of all samples. Note that each surface measurement was repeated three times without removing the sample to ensure repeatability. For three samples of each set (with and without preheating) the residual stress profile was measured along the Z-direction starting from the top surface as illustrated in Figure 4-4. The profile measurements were made by continuous electro-polishing of a tiny spot on the surface to

avoid the residual stress being affected or released. The large volume of the part relative to the removed material retains the residual stresses, and the electrochemical material removal does not introduce any new stresses. The measurements, including normal stress (σ_N), shear stress, and full width at half maximum (FWHM) were made at three different orientations of 0, 45, and 90 degrees.

The density of the as-built samples was measured using the Archimedes method with the aid of a scale with an accuracy of ± 0.1 mg. Front sections of the cubic parts were ground and polished according to the standard metallography procedure. The defects of the cubic parts were characterized by observing the non-etched sections using a Keyence VHX digital optical microscope. For microstructural characterizations, the polished sections were chemically etched using 4% Nital reagent and were evaluated using a Verios XHR scanning electron microscope (FE-SEM) from Thermo-Fisher Scientific equipped with an electron backscatter diffraction (EBSD).

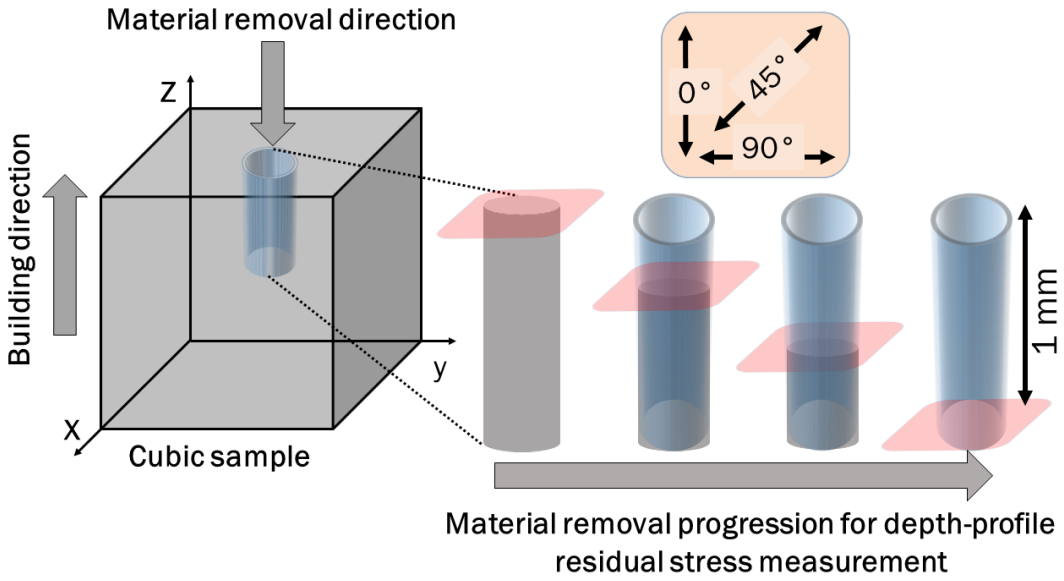

Figure 4-4 The procedure of depth profile residual stress measurement of the LPBF-manufactured cubic samples. The measurements were performed in a step-wise manner by removing a small spot via electro-polishing along the Z-direction. At each step, the residual stress measurements were made at three different orientations of 0, 45, and 90˚. The residual stress was quantified up until the maximum depth of 1 mm.

4.3 Finite element modeling method

4.3.1 Thermomechanical simulation of LPBF process

A sequential thermal-stress analysis of LPBF process consists of a transient heat transfer analysis of thermal loads introduced by the process on a printing part followed by a static structural analysis that is driven by the temperature field from the thermal analysis. The analysis can also include support structures (if required for the build) and a substrate where the part and support are built to consider their influences on thermal conduction, part deflections, and residual stresses. Due to the inability of the process-level simulation approach to predict macro-scale deflections and residual stresses, a part-level simulation

approach was implemented in this study to characterize the deflections and residual stresses using the scheme provided in Figure 4-5. The part-level simulation is computationally efficient for the prediction of deflections and stresses in printing parts with reasonable accuracy [50]. In this approach, the heat transfer analysis can usually capture far-field temperature evolutions (away from action zones) as long as the thermal energy balance of progressive heating and cooling is modeled correctly. However, the simulation may not capture local rapid temperature evolutions properly because the specified sequence of concentrated, fast-moving heat sources is lumped over both time and space. In other words, the temperature results do not usually contain an accurate history of melting and solidification. In this case, to model the annealing or melting effects in the stress analysis correctly, an initial temperature representing a relaxation temperature above which thermal straining induces negligible thermal stress in the printing part must be assigned. Upon element activation, the relaxation temperature is the temperature from which the initial thermal contraction occurs.

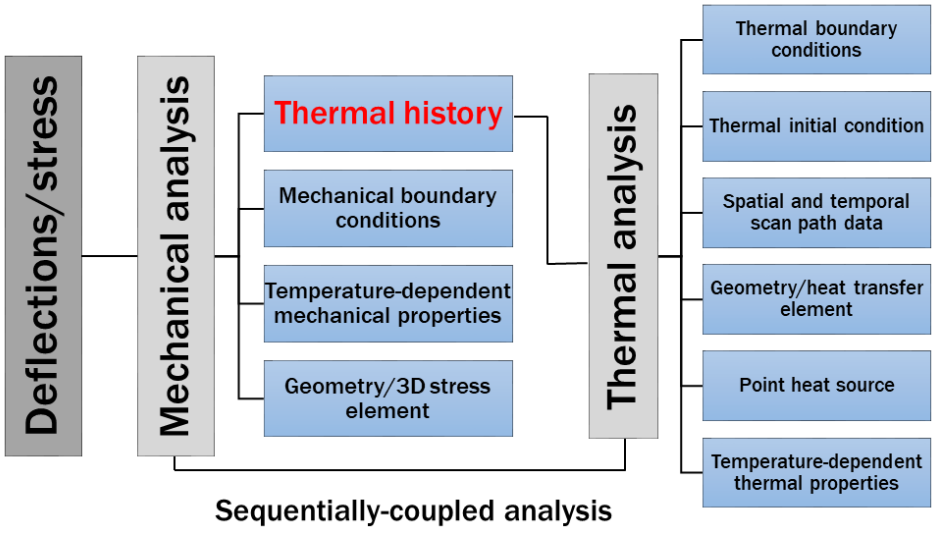

Figure 4-5 The overview of the sequentially coupled thermomechanical analysis.

4.3.2 Governing equations

The governing equation for thermal analysis in the detailed process simulation is the heat conduction equation [42]:

$$\rho c_p \frac{\partial T}{\partial t} = \frac{\partial}{\partial x}\left(\kappa \frac{\partial T}{\partial x}\right) + \frac{\partial}{\partial y}\left(\kappa \frac{\partial T}{\partial y}\right) + \frac{\partial}{\partial z}\left(\kappa \frac{\partial T}{\partial z}\right) + Q \quad \text{Eq.2}$$

where ρ is the material density, T is the temperature, c_p is the temperature-dependent heat capacity, t is time, k is the temperature-dependent thermal conductivity of the material, and Q is the point heat input term. Initial condition and boundary conditions of the governing equation

are shown in Eqs. 3–5, respectively:

$$T(x, y, z, t_0) = T_0, \quad (x, y, z) \in \Omega \quad \text{Eq. 3}$$

$$T = \bar{T}, \quad (x, y, z) \in \partial\Omega_D \quad \text{Eq. 4}$$

$$-\kappa \nabla T.n = h(T - T_0), \ (x, y, z) \in \partial\Omega_R \quad \text{Eq. 5}$$

where T_0 denotes the initial temperature. Since in this study the analysis is performed under two conditions of with and without preheating, the initial temperature was set to 200 °C and 25 °C in detailed process modeling. Eqs. 4 and 5 define the Dirichlet boundary ($\partial\Omega_D$) and Robin or convection boundary ($\partial\Omega_R$), respectively, and $\partial\Omega = \partial\Omega_D \cup \partial\Omega_R$. The heat loss due to the radiation is given by Eq. 6:

$$-\kappa \nabla T.n = \sigma\zeta(T^4 - T_0^4) \quad \text{Eq. 6}$$

where σ is the Stephan-Boltzmann constant and ζ is the emissivity.

A quasi-static mechanical analysis is conducted in sequential thermal load steps using the temperature history obtained to solve the mechanical response. The governing equation for the mechanical analysis is the stress equilibrium equation written as:

$$\nabla.\sigma + \rho b = 0 \qquad \text{Eq. 7}$$

where σ is the stress tensor and b is the body force per unit volume. The boundary condition is defined as:

$$U = \bar{U}, \qquad (x, y, z) \in \partial\Gamma_u \qquad \text{Eq. 8}$$

$$\sigma.n = \bar{t}, \quad (x, y, z) \in \partial\Gamma_t \qquad \text{Eq. 9}$$

where the displacement vector U on boundary $\partial\Gamma_u$ is specified as $\bar{U}$ and the surface vector on boundary $\partial\Gamma_t$ is defined as $\bar{t}$. In the mechanical analysis, the material constitutive model is assumed to be elastic and perfect plastic with von Mises plasticity law:

$$\sigma = C : \varepsilon_{elastic} \qquad \text{Eq. 10}$$

$$\varepsilon_{total} = \varepsilon_{elastic} + \varepsilon_{plastic} + \varepsilon_{thermal} \qquad \text{Eq. 11}$$

$$\varepsilon_{thermal} = \alpha.\Delta T \qquad \text{Eq. 12}$$

$$f^{yield} = \sqrt{\frac{3}{2}\sigma_{ij}\sigma_{ij} - \frac{1}{2}\sigma_{kk}\sigma_{kk}} - \sigma_Y \qquad \text{Eq. 13}$$

where C is the fourth-order stiffness tensor, and $\boldsymbol{\varepsilon}_{\text{elastic}}$ is the elastic strain tensor. The stress tensor can be expressed as the double-dot product of the stiffness tensor and elastic strain tensor. Total strain $\boldsymbol{\varepsilon}_{\text{total}}$ is the sum of elastic strain $\boldsymbol{\varepsilon}_{\text{elastic}}$, plastic strain $\boldsymbol{\varepsilon}_{\text{plastic}}$ and thermal strain $\boldsymbol{\varepsilon}_{\text{thermal}}$. α is the temperature-dependent coefficient of thermal expansion (CTE), and ΔT denotes the change in temperature. When $f^{yield} = 0$, yielding occurs and then generates plastic strains.

4.3.3 Model description

ABAQUS software was utilized to carry out the modeling. The part geometry for simulation of the deflections and residual stresses is a simple twin-cantilever structure of dimensions 50 mm, 10 mm, and 10 mm in length, width, and height, respectively (Figure 4-3).

For each build process, 12 parts were built on the same substrate. However, as spacing is sufficient between parts such that the build of an adjacent part has a negligible effect on the thermal history of the current part, the model is reduced to a single part, saving on computation time. Nevertheless, it is important to consider the entire build layout when calculating the cooling time between layers (120 s), as this will have a first-order impact on the thermal history of the part and consequently the residual strain field. The reduced model is a single part, mounted on a section of the substrate. The section is taken to be 100 × 45 × 15 mm^3 (length × width× height).

In order to achieve a structured mesh, the build part was partitioned. Throughout the thermal analysis, linear hexahedron (DC3D8) elements were implemented. An identical mesh was used in the structural analysis, to allow the analysis to take place on a compatible mesh. The characteristic element size of the build was 0.20 mm (Figure 4-6). Hence, each element accounted for approximately 10 real layers. Single element layers were unfeasible due to the large number of layers within the model. The element size was chosen as a compromise between accuracy and run time. The partial integration and homogenization modeling techniques in the ABAQUS 2019 solver were leveraged to mitigate the discrepancy between element size and layer thickness.

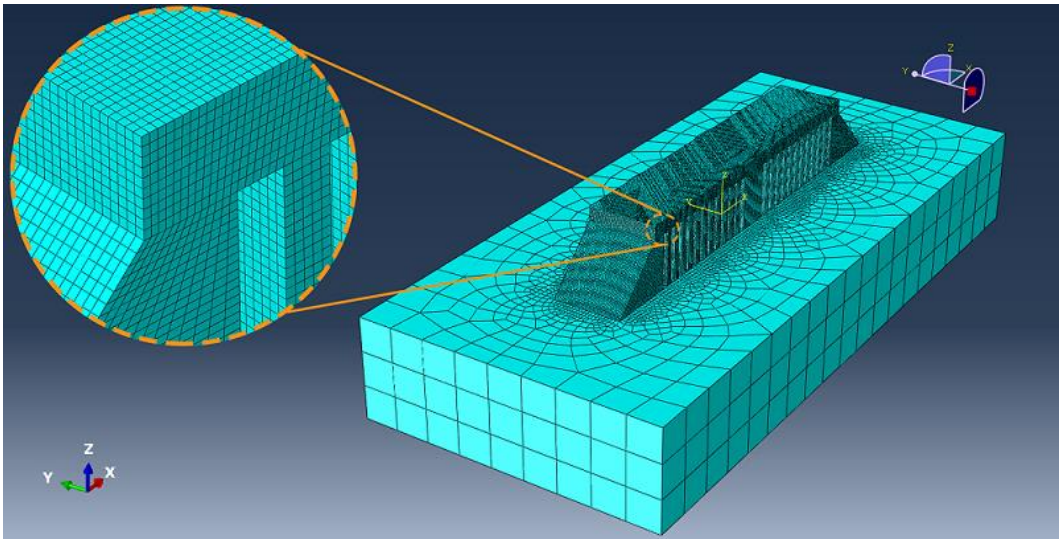

Figure 4-6 Illustration of the twin-cantilever beam with structured mesh shown in the inset.

Figure 4-7 gives the values of the temperature-dependent properties of H13 tool steel, including thermal conductivity, specific heat capacity, Young's modulus, Poisson's ratio, and coefficient of thermal expansion (CTE). In general, for manufacturing process simulations, the temperature-dependent plasticity behavior of the material under consideration is required. For example, temperature-dependent stress-strain curves should be implemented in the finite element solver to accurately account for the softening response at elevated temperatures. However, due to the range of temperatures that are experienced by the material as a result of the time integration method used, the plastic behavior exhibits only a small dependency on temperature. The room temperature plastic properties of the LPBF-manufactured H13 tool steel in as-build condition as per [6] were used in the simulation. The rest of the parameters used in the simulation are listed in Table 4-2. In this study, the relaxation temperature was taken as 70% of the H13 tool steel annealing temperature, which amounts to 800 K.

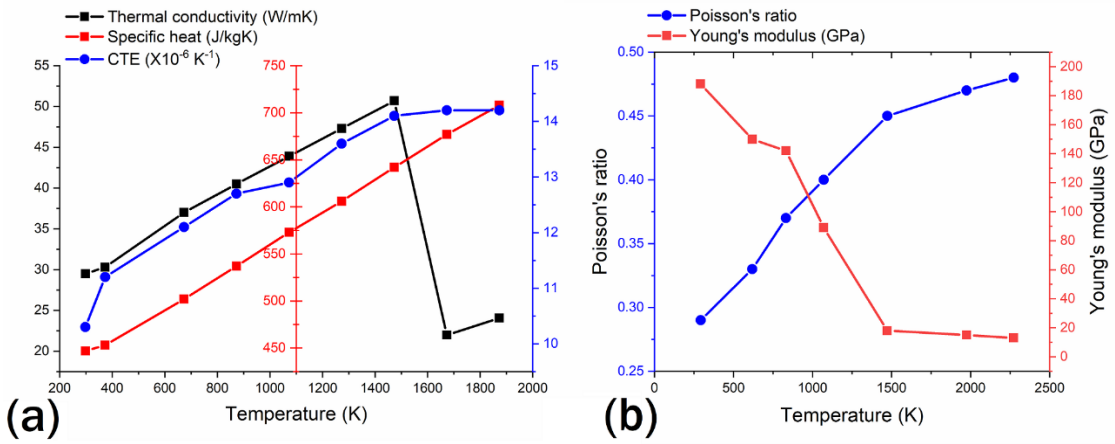

Figure 4-7 Temperature-dependent properties of H13 tool steel (a) thermo-physical and (b) mechanical [51]

Table 4-2 List of parameters used in the simulation for H13 tool steel.

Parameters	*Values*
Laser Power (W)	300
Scan speed (mm/s)	800
Hatch spacing (mm)	0.12
Absorption efficiency (%)	60
Thermal initial condition (K)	298, 498
Relaxation temperature (K)	800, 550
Emissivity	0.85 [52]
Convection coefficient ($W/m^{-2}K$)	20 [52]

4.4 Experimental results

4.4.1 Densification level-volumetric energy density relationship

Figure 4-8 shows the variation in the density as a function of the employed Ev. As being observed, the density showed an ascending trend with enhancing Ev up to about 80 J/mm3,

followed by a slight decrease. The process parameters leading to the highest densification level were introduced as the optimum condition, referring to samples A3 and PA3 with Ev of 78.1 J/mm3 featuring relative densities of 98% and 99.2%, respectively. It is self-evident that samples subjected to the preheating benefit from densities higher than those of the no preheat condition, regardless of the employed Ev. According to the cross-sectional optical micrographs presented in Figure 4-8, the Ev lower (Figure 4-8(b), (e)) and higher (Figure 4-8(d), (g)) than the optimum value resulted in the decreased densification level. The difference in size, shape, and volume fraction of the defects formed in parts gives evidence of their significant dependence on the applied E_v. For instance, while the samples fabricated with relatively low E_v suffer from irregular-shape defects, those with extremely high E_v are characterized by their spherical voids. Except for D1 sample, cracks are perceptible in the no preheat scenario. However, the application of preheating eradicated the cracking in all samples.

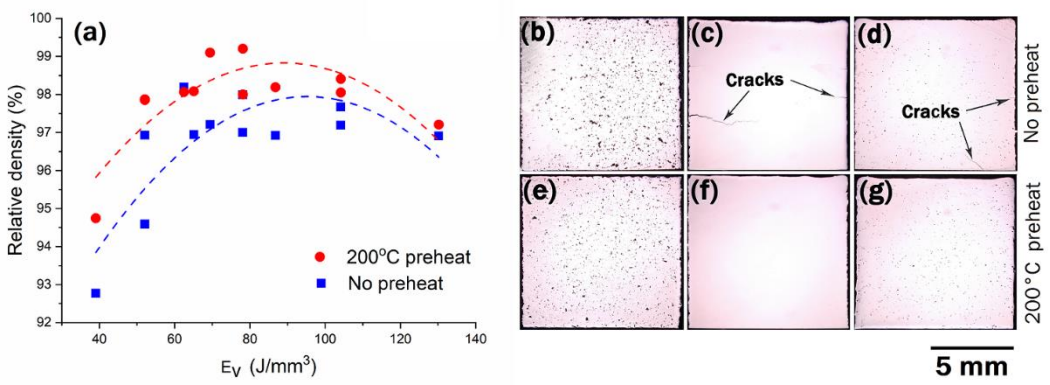

Figure 4-8 The variation in the relative density of the LPBF-fabricated H13 tool steel parts versus the volumetric energy density (E_v) for "preheat" and "no preheat" conditions. (b-g) show cross-sectional optical micrographs of: (b) D1, (c) A3, (d) B3, (e) PD1, (f) PA3, and (g) PB3 samples.

4.4.2 Beam deflection and residual stress measurements

After cutting the supports from the substrate, CMM measurements were conducted on all of the cantilevers along their length at 11 distinct points in the Z-direction. Figure 4-9(b) and (c) represents examples of such measurements on deflection curves obtained. The maximum deflection of twin-cantilever beams measured at a point located either on the utmost right or left of the beams are shown in Figure 4-9(a). As it is evident from Figure 4-9(a), the maximum deflection is significantly smaller for almost all preheated samples compared to their non-preheated counterparts. The few anomalies observed may be attributed to the presence of cracks and subsequent release of residual stresses in the non-preheated beams. The maximum and minimum beam deflections in the non-preheated scenario were for A1 and B3 samples, respectively. On the other hand, those for the preheated case were A2 and C2 samples, respectively.

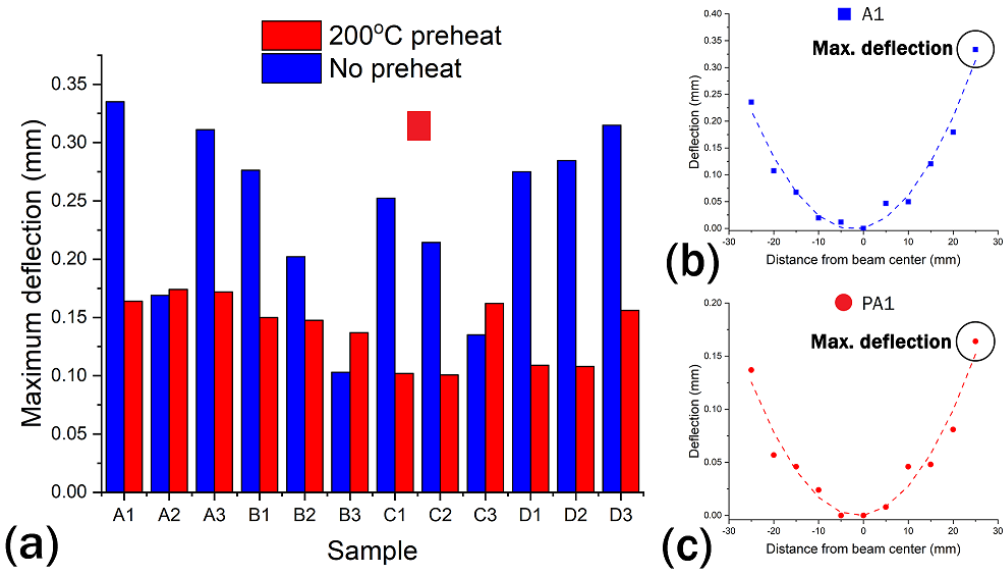

Figure 4-9 (a) Maximum deflection of twin-cantilever beams along the Z-direction in different samples for both preheat and no preheat conditions. Deflection curves along the length of the twin-cantilevers for A1 and PA1 samples are shown in (b) and (c), respectively.

The results of normal residual stress measured at the center of the top surface for all cubic coupons in three distinct orientations of 0, 45 and 90° are presented in Figure 4-10. Regardless of process parameters and preheating condition employed, almost all samples featured compressive residual stress on their top surface. The measurements in all orientations suggest that the magnitude of compressive stress is conspicuously larger in the non-preheated condition compared to the preheated scenario. For non-preheated samples (C3 and D1) with a low magnitude of compressive stress, the residual stress regime changed to tensile upon preheating. It is worth noting that although the residual stress measurement results in different orientations follow the same trend, the difference in their magnitudes gives evidence of in-plane anisotropy on the top surface.

Based on density measurement results and optical microscopy observations provided in Figure 4-8, three samples with low (D1, PD1), optimum (A3, PA3), and high (B3, PB3) E_v were selected for depth profile residual stress measurements in both preheat and no preheat conditions. Figure 4-11(a-c) shows the depth profile of the residual stresses up to 1 mm below the top surface of cubic coupons in three different orientations (0, 45, and 90°). The minimum and maximum principal stresses, along with the absolute value of the equivalent residual stresses were derived from the measurements in different orientations and are shown in Figure 4-11(d-f). It is self-evident that the nature of residual stresses changes from compressive to tensile immediately below the top surface (~0.1 mm) of the test coupons for highly porous samples (D1, PD1) fabricated at low E_v. However, entering the tensile zone lags behind by increasing the Ev. For highly dense samples (A3, PA3) and those printed with comparatively higher Ev (B3, PB3), the residual stresses transform from compressive to tensile at a depth corresponding to ~0.2 and ~0.3 mm, respectively.

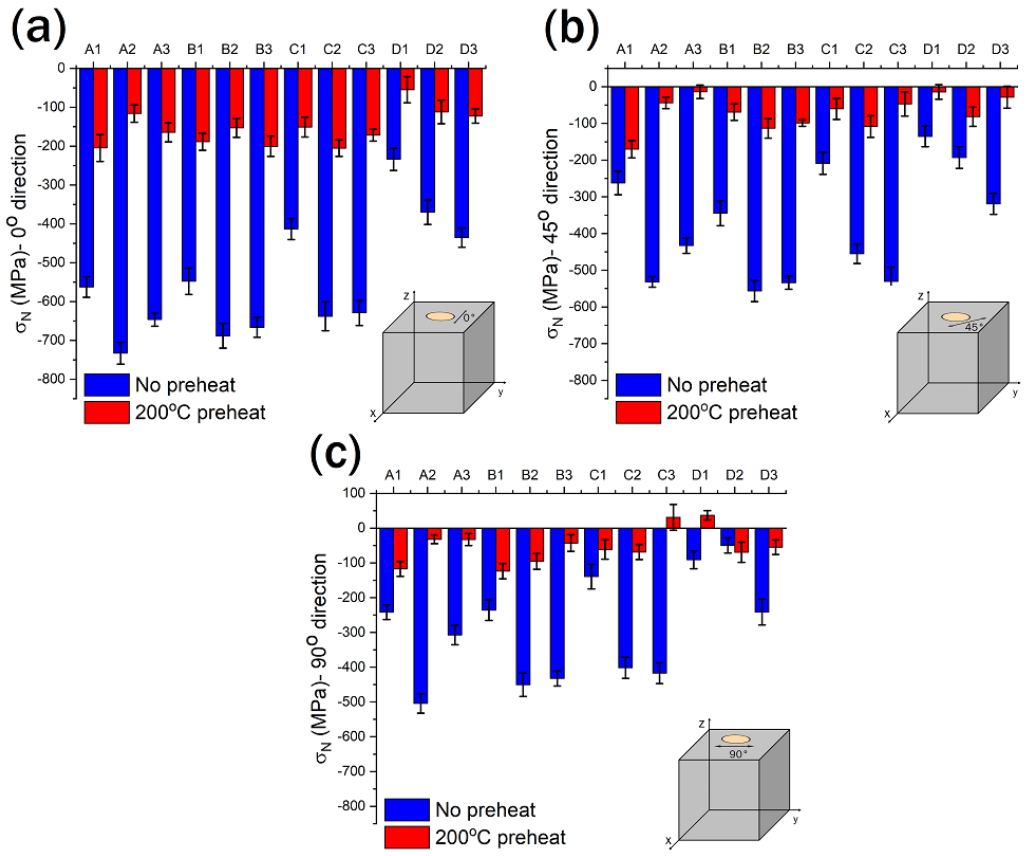

Figure 4-10 Normal residual stress measurement results on the top surface of cubic coupons at orientations of: (a) 0°, (b) 45°, and (c) 90°. The test is performed at the center of the top surface designated by the yellow spot in the figures.

After transforming from compressive to tensile, the nature of residual stresses remains tensile up to 1 mm below the top surface. This trend holds for all measured and derived residual stresses shown in Figure 4-11. In the compressive zone, the magnitude of residual stresses for parts subjected to preheating was lower than the corresponding ones printed without preheating, while the opposite is perceptible in the tensile zone. In other words, preheating led to higher residual stresses in the tensile zone. It is of note that except for the D1 and PD1 samples, the difference between the residual stresses for with and without

preheating conditions is highly significant. However, such a difference is less pronounced in the tensile zone.

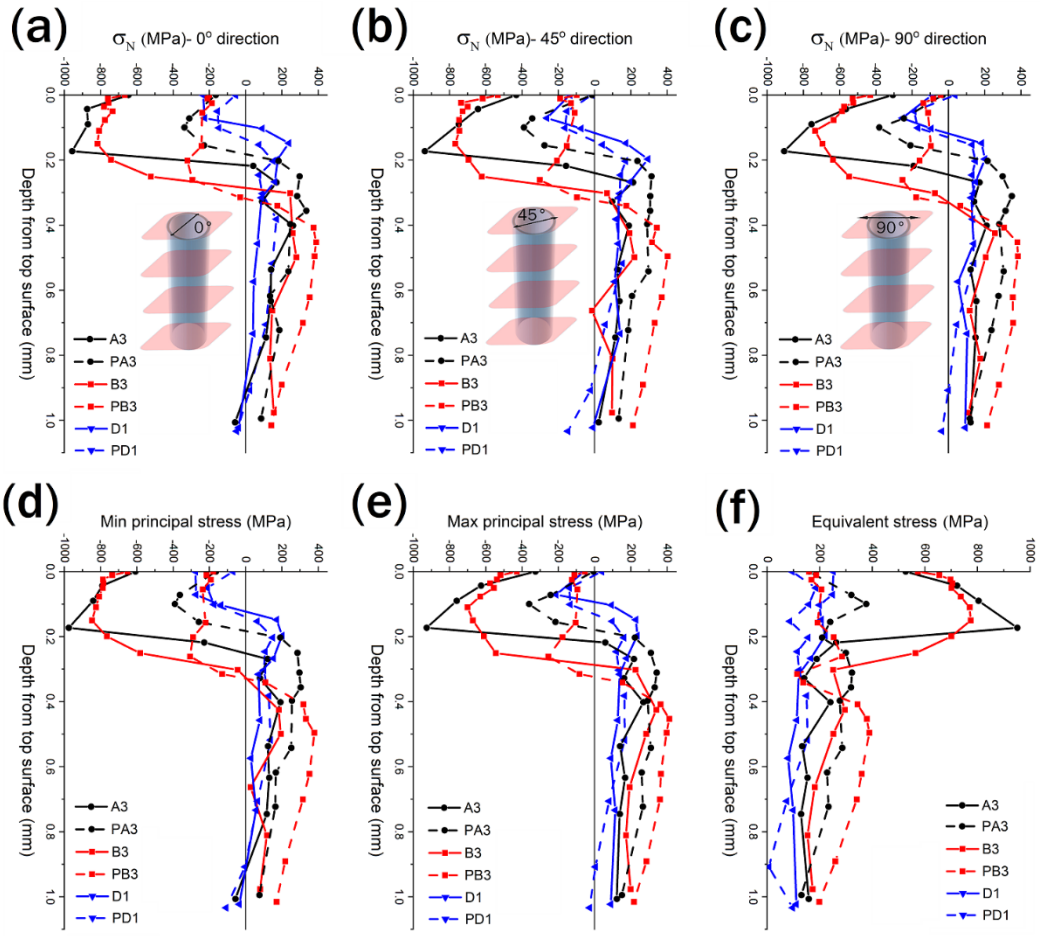

Figure 4-11 Depth profile residual stress measurement results of cubic coupons at orientations of (a) 0°, (b) 45°, and (c) 90°. The test is performed along the Z-axis in orientations designated by the black arrows in the figures. The derived minimum and maximum principal stresses along with the absolute equivalent stress are shown in (d), (e) and (f), respectively.

4.5 Simulation results

Beam deflections of samples in both preheat and no preheat conditions were simulated to investigate the ability of the model to predict the magnitude of deflections. The process parameters that led to almost fully dense samples (A3, PA3) were used for the simulation to mitigate the influence of the defects on the prediction outcomes. Figure 4-12 shows the results of the beam deflections in the Z-direction along the length of the twin-cantilever beam when the relaxation temperature was set to be 800 K. As it is evident, the magnitude of the beam deflection in the case of the preheating is noticeably lower than that of the non-preheated condition.

The maximum deflection decreased from 0.75 mm to 0.45 mm upon applying 200 °C preheat, which is attributable to the lower temperature gradients and consequently reduced residual stresses in the latter scenario. In order to accomplish a part-level simulation for H13 tool steel, the model excludes the influence of defects and martensitic phase transformation. Their absence in the model, martensitic phase transformation, in particular, caused the model overestimating the magnitude of deflections compared to those of measurements made by CMM.

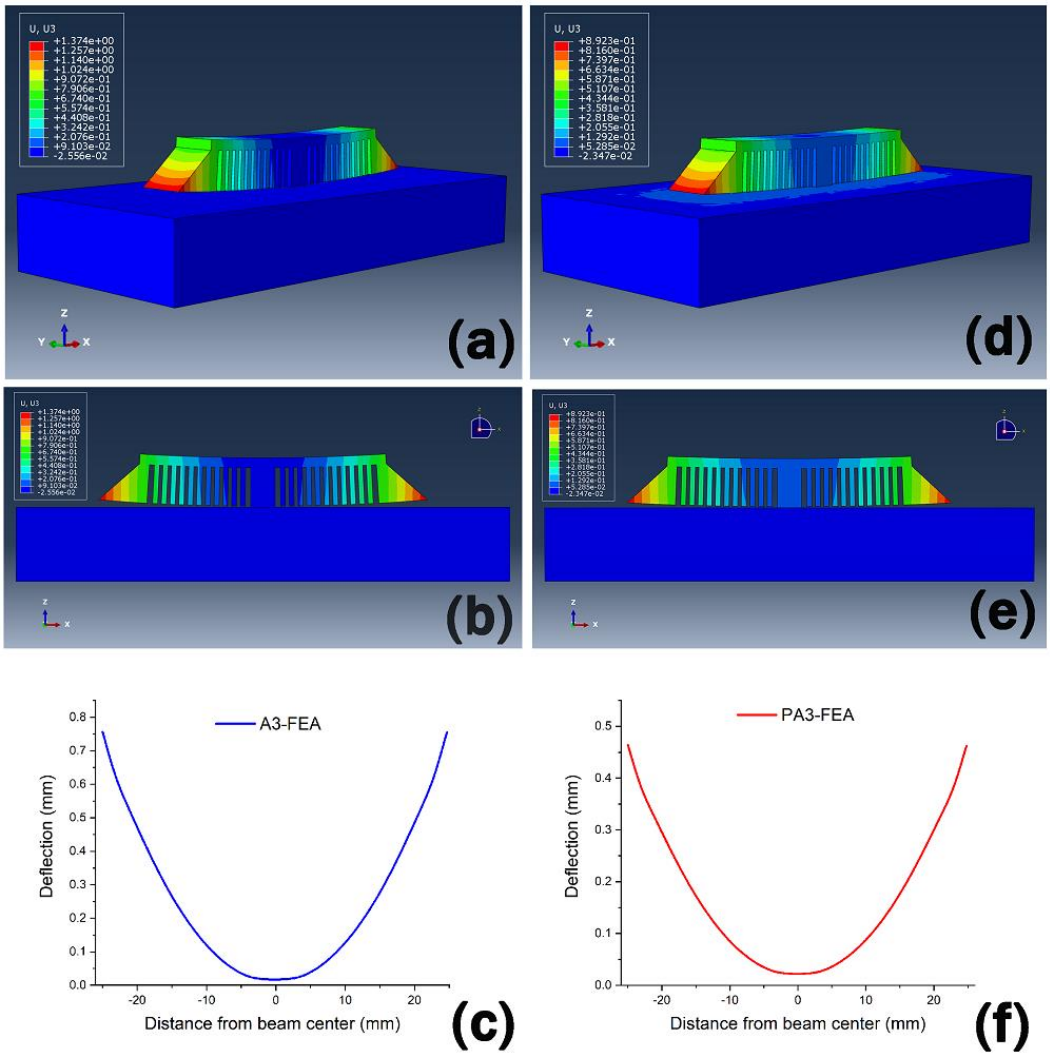

Figure 4-12 Finite element analysis (FEA) results of the twin-cantilever beam displacement field in the Z-direction (U3) showing: (a) and (d) the overview after cutting, (b) and (e) the front view of the deflection in the ZX plane, (c) and (f) deflection profiles along the length of the beams in (b) and (e), respectively. (a-c) sample A3 and (d-f) sample PA3. The implemented relaxation temperature was 800 K.

4.6 Discussion

As mentioned before, the layer-wise nature of the LPBF process introduces large thermal gradients, which in turn causes the formation of residual stresses in the final printed parts. There are multiple contributing factors that would affect the status of the developed residual stresses and consequently beam deflections of LPBF processed H13 tool steel, namely, preheating condition, densification level, process parameters, and martensitic phase transformation. These factors are simultaneously affecting the status of residual stresses and could not be isolated to be investigated individually. However, in the wide range of processing window implemented in this study, there are a few occasions in which one factor is significantly contributing while the others are constant or have a negligible impact. In the following sections, the role of each factor will be discussed to understand the general trends regardless of the influence of the other involving factors. This helps to justify the residual stress and beam deflection measurement results when only one contributing factor plays a crucial role. For other cases, the combination of all contributing factors will be taken into account to elucidate the obtained results.

4.6.1 Role of martensitic phase transformation

According to Figure 4-1, the contractions associated with the liquid to solid transformation as well as the decrease in the temperature during the cooling stage will be constrained by the surrounding consolidated tracks and layers, which results in the development of tensile residual stresses on the top surface. However, as it is apparent in Figure 4-10 and Figure 4-11, the nature of the residual stresses on the top surface is compressive for almost all cases in the H13 tool steel. This unexpected result could be explained by taking the

influence of the martensitic phase transformation into consideration. During LPBF processing of H13 tool steel (with 0.39 wt.% C), the material experiences the following solidification path [53]:

$L \rightarrow \gamma + L \rightarrow \gamma \rightarrow M + \gamma'$

in which L, γ, M, and γ′ denote the liquid, austenite, martensite and retained austenite phases, respectively. The microstructural observations provided in Figure 4-13(a) and (b) reveals a cellular microstructure in which the core of the cells and the cell boundaries are composed of martensite and retained austenite, respectively. EBSD results shown in Figure 4-13(c) as well as the XRD results [23] confirm that martensite is the predominant phase in the microstructure of LPBF-processed H13 tool steel. The transformation of the already solidified austenite to martensite is accompanied by a volume expansion of 1.03% [47], which will be constrained by the surrounding solid material with a martensitic microstructure. This, consequently, leaves behind compressive residual stress in the material.

According to the abovementioned discussion, the nature of the resultant residual stresses is determined by the competition between two opposing phenomena: (i) tensile residual stress caused by the contraction during solidification as well as the temperature drop, and (ii) compressive residual stress due to the expansion originating from the martensitic phase transformation. Given the fact that almost all the measured residual stresses were compressive on the top surface, the dominancy of the latter is deduced.

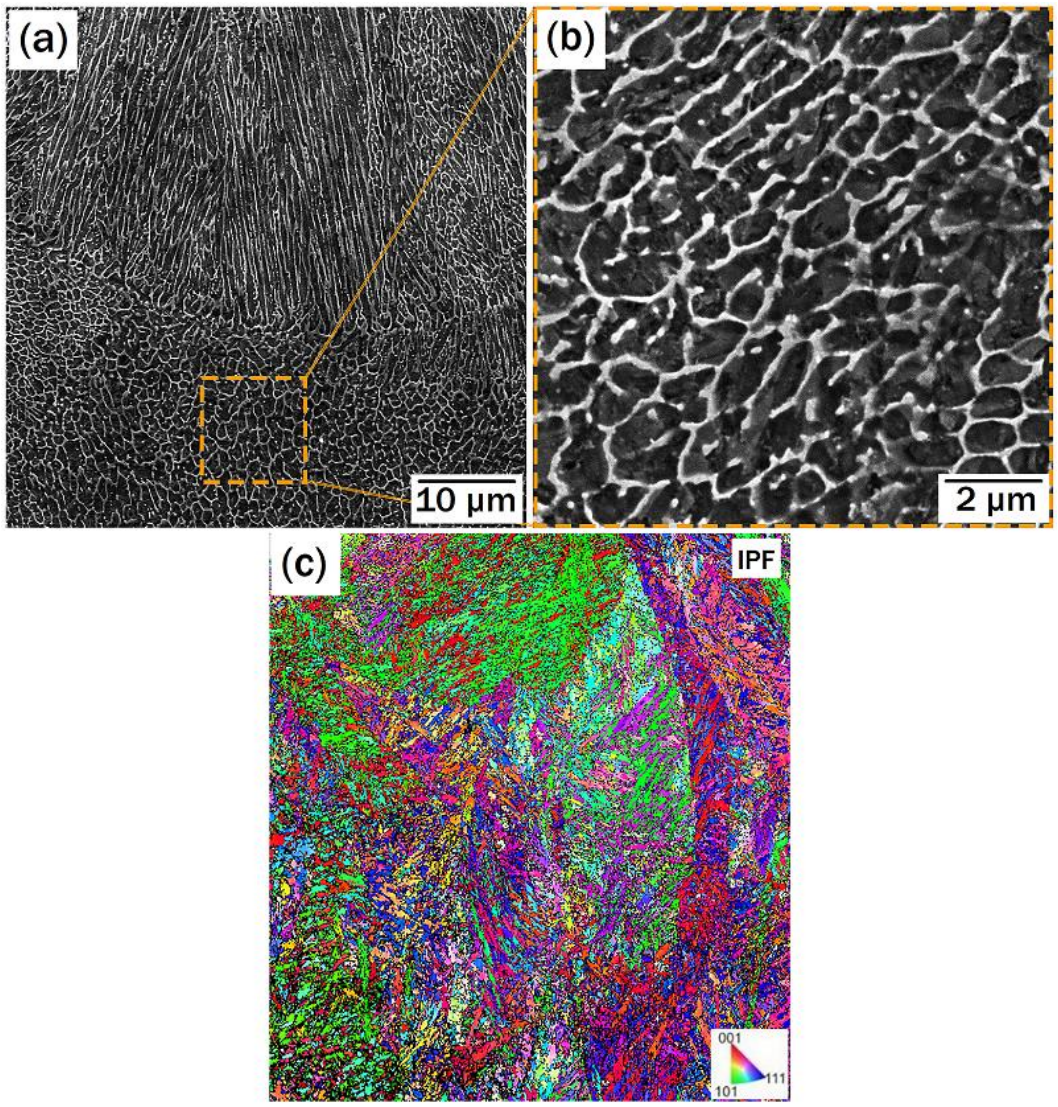

Figure 4-13 (a) and (b) SEM micrographs of the LPBF-processed H13 tool steel showing a cellular microstructure with the cell cores and boundaries being martensite (M) and retained austenite (γ), respectively.

According to Figure 4-11, the compressive residual stresses shift to tensile residual stresses immediately below the top surface. It is interesting to highlight that there is a correlation between this transition depth and the E_v for both preheated and non-preheated scenarios. For E_v levels corresponding to 39.1 (D1, PD1), 78.1 (A3, PA3), and 130.2 J/mm^3 (B3, PB3), the transition depth is approximately 0.1, 0.2, and 0.3 mm, respectively. Figure 4-14

shows the last consolidated layer for the non-preheated scenario. As it is apparent, the transition depth is almost identical to the thickness of the last consolidated layer. Therefore, the residual stresses are only compressive at the last layer and would enter the tensile zone immediately upon adding the next layer on top of them.

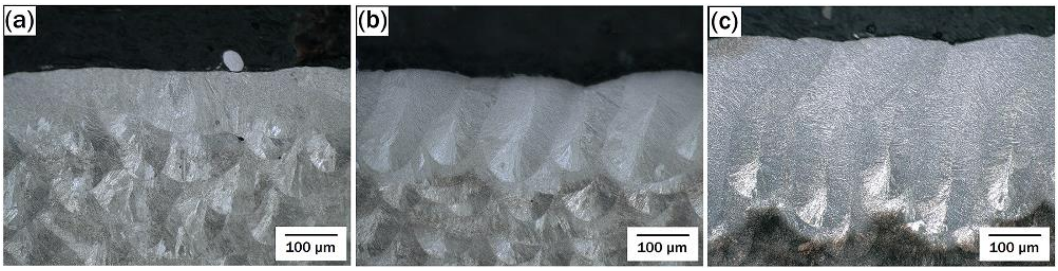

Figure 4-14 Optical micrographs showing the front views of: (a) D1, (b) A3, and (c) B3 samples.

This sharp transition from compressive to tensile residual stresses could be elaborated based on the schematic provided in Figure 4-15. As shown in Figure 4-15(a), the residual stresses in an as-consolidated layer (layer (n-1)) are compressive due to the dominancy of compressive residual stresses caused by the martensitic phase transformation. Upon adding a new layer (layer (n)), the same compressive residual stresses would be generated in the new layer (Figure 4-15 (b)). However, due to the expansion associated with the martensitic phase transformation, layer (n) exerts tensile stress to previous layers acting as a constraint on it. According to Figure 4-11, not only this tensile stress could cancel out the previously formed compressive stresses but also led to the creation of tensile residual stresses below the last consolidated layer. Although all samples have only tensile residual stresses up to 1 mm below the last layer, the nature of the residual stresses might change further down. This is attributed to the complex thermal cycling of LPBF process.

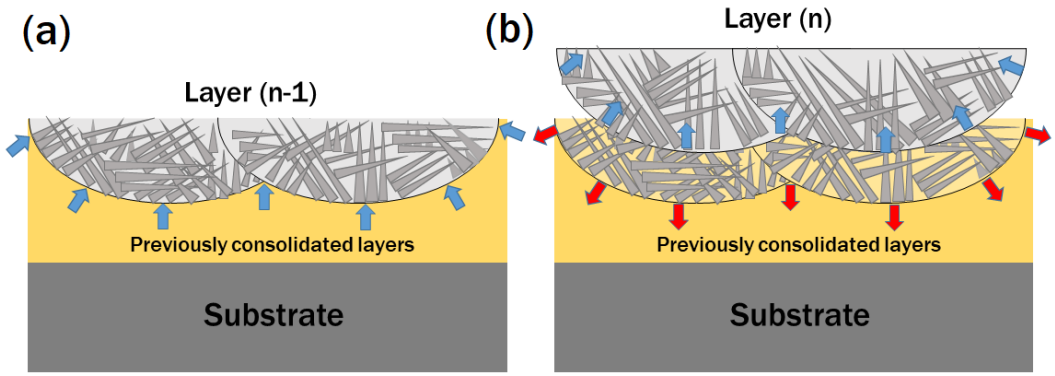

Figure 4-15 Schematic illustration of: (a) compressive residual stresses generated the LPBF process for the last two layers.

4.6.2 Role of preheating

Referring to Figure 4-10 and Figure 4-11, much lower magnitudes of compressive residual stresses are perceptible in the preheat scenario. In H13 tool steel, the martensitic phase transformation starts (M_S) and finishes (M_f) at 285°C [24] and 50°C, respectively [54]. When no preheat is applied, H13 cools down rapidly to the ambient temperature (below M_f) which provides an opportunity for the full transformation of γ to M. Although the recent research studies performed on LPBF processing of H13 tool steel have shown the existence of a small amount of γ′in the final microstructure [23, 55], they have all confirmed an almost fully martensitic microstructure. 200°C of preheating, on the other hand, limits the progression of martensitic phase transformation owing to this fact that the minimum temperature during processing is noticeably higher than M_f. Therefore, a lower magnitude of compressive residual stresses is expected to be generated due to the lower fraction of M formed in the consolidated layer during the LPBF process. The fraction of martensite as a function of temperature can be expressed based on the Koistinen–Marburger (KM) equation [56]:

$$f = 1 - \exp\left(-\alpha_m (T_{KM} - T)\right) \quad \text{Eq. 14}$$

where f, α_m, and T_{KM} are the volume fraction of martensite, rate parameter, and the theoretical martensite-start temperature (lower than M_S), respectively. The α_m, and T_{KM} terms can be calculated as follows [57]:

$$\alpha_m(K^{-1}) = 0.0224 - 0.0107x_C - 0.0007x_{Mn} - 0.00005x_{Ni} - 0.00012x_{Cr} - 0.0001x_{Mo} \quad \text{Eq. 15}$$

$$T_{KM}(°C) = 462 - 273x_C - 26x_{Mn} - 16x_{Ni} - 13x_{Cr} - 30x_{Mo} \quad \text{Eq. 16}$$

By substituting the chemical composition of the H13 tool steel used in this study [23] into Eq. 15 and Eq. 16, the α_m and T_{KM} were calculated to be $0.017K^{-1}$ and 234°C, respectively. Using Eq. 14, the volume fraction of martensite (f) was determined 97% at room temperature and 44% at 200°C. The significantly lower volume fraction of martensite in the preheated condition (53%) is the main reason behind the lower magnitudes of compressive residual stresses in this case. Although the martensitic phase transformation continues by further cooling of the material from 200°C to room temperature, almost no additional thermally induced compressive residual stresses will be generated. This can be ascribed by considering the absence of mechanical constraints in this stage since the whole printed part and the attached substrate experience this drop in the temperature simultaneously.

It should be borne in mind that unlike the no preheat scenario, the parts printed with the application of 200°C of preheating cool down to this temperature rather than room temperature, which in turn results in shallower temperature gradients and consequently lower thermal strains ($\Delta\varepsilon^T = \alpha(T - T_0)$). As mentioned in section 4.6.1, the temperature

gradient during the laser-wise fabrication in LPBF process is responsible for the creation of tensile residual stresses. Therefore, compared to the non-preheated case, 200°C of preheating brings about lower thermal strains and tensile residual stresses. Therefore, both tensile and compressive residual stresses decreased when 200°C of preheating was applied. However, the reduction in compressive residual stresses is more noticeable than the tensile ones, as suggested by Figure 4-10 and Figure 4-11.

The results of the maximum beam deflections measured by CMM are provided in Figure 4-9. Since the residual stresses are more compressive on the top surface of non-preheated samples, they are expected to feature a lower magnitude of deflections. However, the contrary is the case. This can be justified based on the results shown in Figure 4-16, in which the residual stress profile measurements have been extended to a higher depth of 1.6 mm for PB3 cubic coupon in three different orientations (0, 45, and 90°). As it is evident, although the top surface residual stresses in the case of preheated samples are less compressive compared to their non-preheated counterparts (Figure 4-9), the residual stresses are highly compressive in the bulk of the preheated ones. Due to the fact that the beam deflections reflect the overall residual stresses in the whole part, the depth profile residual stress measurements (Figure 4-16) are a better representative of the deflection state of the parts. In conclusion, despite the fact that the top surface residual stresses are a suitable criterion for comparing beam deflections of the samples in the same category (preheat and no-preheat), they might be misleading when it comes to inter-category comparison.

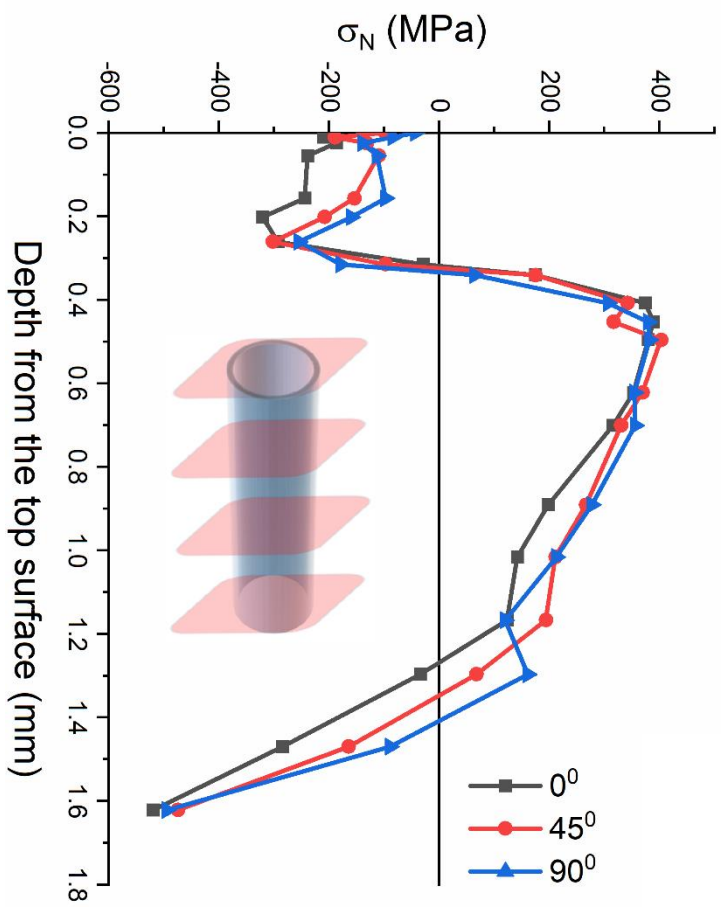

Figure 4-16 Depth profile residual stress measurement results along the Z-axis of PB3 cubic coupon at orientations of 0°,45°, and 90°.

4.6.3 Role of process parameters

In this study, a wide range of process parameters was applied by changing the laser power and scanning velocity, while the other parameters (e.g., hatch spacing and powder layer thickness) were kept constant. The process parameters are combined into Ev, represented by Eq. 1. Figure 4-17 illustrates the variation of normal residual stress (on one spot at the top surface) in terms of Ev for three orientations of 0, 45, and 90°. As could be seen, the residual stresses on the top surface of almost all test coupons are compressive due to the

martensitic phase transformation. In general, the normal residual stresses continuously grow compressive as the Ev increases for no preheat condition. As mentioned earlier, the residual stress in the LPBF-processed H13 tool steel consists of tensile and compressive components. Since the microstructure of all non-preheated samples is mainly comprised of martensite regardless of the process parameters employed, it is reasonable to conclude that the contribution of compressive residual stress remains unchanged with varying Ev. Therefore, the difference in the magnitude of residual stresses across Ev spectrum is attributable to the variations in tensile residual stresses. According to Figure 4-17, the increase in Ev led to larger compressive residual stresses. This can only be traced back to the decrease in the contribution of tensile residual stress constituent in the overall residual stress regime. Since the melt pool forms in a conductive medium during LPBF process, the increase in the E_v would result in larger melt pools, having hotter surrounding material which in turn creates a shallower temperature gradient during the cooling stage. This shallower temperature gradient is responsible for smaller tensile residual stresses which are reflected in larger compressive stresses. It is worth mentioning that although Figure 4-17 depicts the effect of Ev on the top surface residual stresses, the impact of defects is also lurking in the results. Nevertheless, due to the presence of macro-cracks in almost all of the non-preheated test samples (Figure 4-8), it is believed that this factor does not play a major role in the general trends observed. Therefore, Ev could be held accountable for such a variation.

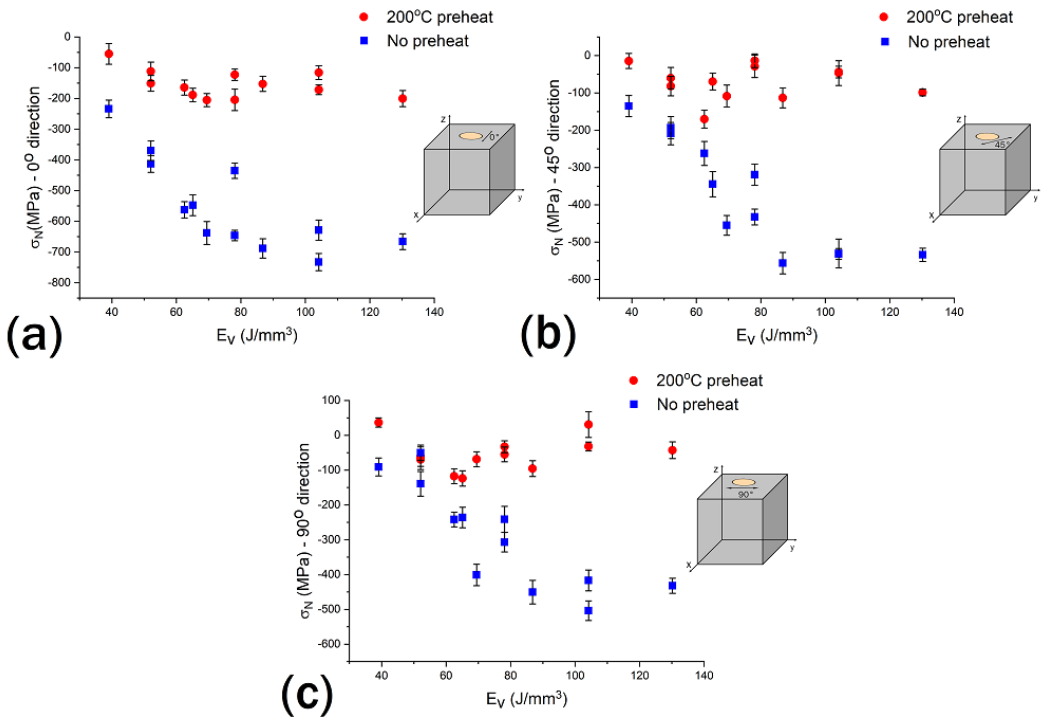

Figure 4-17 The variation in the normal residual stress on the top surface as a function of the Ev at orientations of: (a) 0°, (b) 45°, and (c) 90°. The test was performed at the center of the top surface designated by the yellow spot in the figures.

In comparison to their non-preheated counterparts, the residual stresses of preheated samples reveal no sharp changes across the investigated E_v spectrum. In other words, the differences are not statistically significant. Due to the lower magnitude of residual stresses in the case of preheating, the values seem to be more sensitive to the level of defects compared to the no-preheat condition.

The aforementioned discussion also holds for the magnitude of deflection measured along the length of the beams. Figure 4-18 shows the maximum beam deflections versus the Ev. By comparing Figure 4-17 and Figure 4-18, it can be concluded that larger compressive residual stresses led to lower beam deflections in the no preheat scenario. Similar to the

residual stress-E_v plot of preheated samples, the beam deflections demonstrates no meaningful trend.

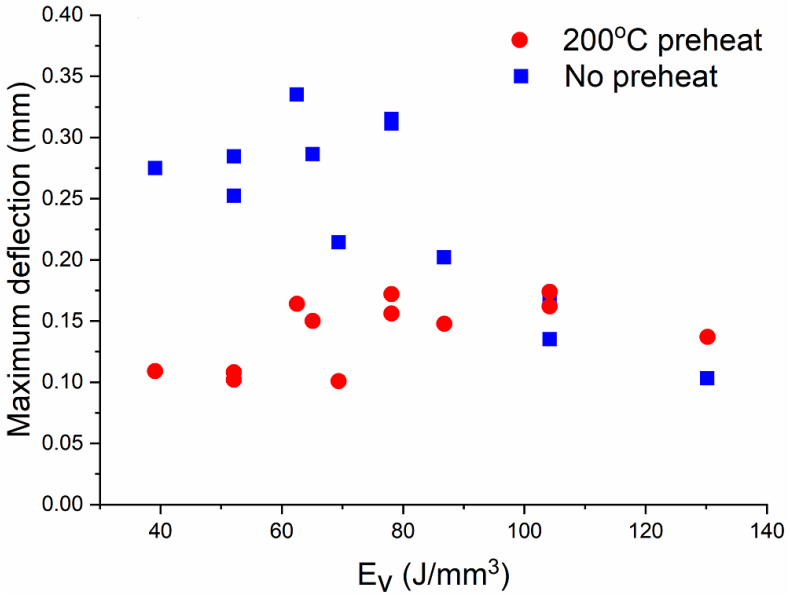

Figure 4-18 The variation of maximum beam deflection as a function of the Ev

4.6.4 Role of defects

The dominant defects in the LPBF-processed H13 tool steel are porosities and cracks. Both of these defects affect the level of residual stresses in the final parts. Porosities that are empty spots in the bulk of the material do not bear loads, which in turn lower the residual stresses based on their extent. Cracks, on the other hand, form as a result of thermal stress accumulation, when exceeding the ultimate tensile strength of the material at any temperature. Crack formation is accompanied by significant stress relieving, causing a drastic change in the residual stress regime. Referring to Figure 4-8(a), the density of the preheated samples is higher than that of the non-preheated ones for any given E_v, meaning that the extent of the defects is greater in the latter. Moreover, all of the non-preheated

samples, except D1, have macro-cracks (Figure 4-8(b-d)) which is a direct indicative of the presence of tensile thermal stresses larger than the ultimate tensile strength of the material during the LPBF process. The lower tensile thermal stresses due to shallower thermal gradients associated with the preheating condition could successfully eradicate the crack formation. However, the porosities still exist in the fabricated parts. The measured residual stresses (Figure 4-10 and Figure 4-11) and maximum beam deflections (Figure 4-9) describe their status after the formation of these defects.

Figure 4-19 shows the variation in the top surface residual stress of the cubic coupons with respect to their relative density at different orientations. In the non-preheated samples with relative densities almost as low as ~93%, the increase in the relative density resulted in the enhancement of the magnitude of the compressive residual stresses, proving the influence of defects on the stress relieving. However, when it comes to densities above 97%, the residual stresses are independent of the relative density. Since the maximum difference between the relative densities of nearly dense samples (densities > 97%) shown in the dashed ovals is only ~1.3%, this finding is justifiable. It should be noted that the magnitude of residual stresses was found to be considerably reliant on the E_v for the non-preheated scenario, revealing the dominancy of this factor over the densification level. For preheated samples in which almost all of the samples possess relative densities higher than ~97.5%, the same discussion provided for the nearly dense samples of the non-preheated case is valid.

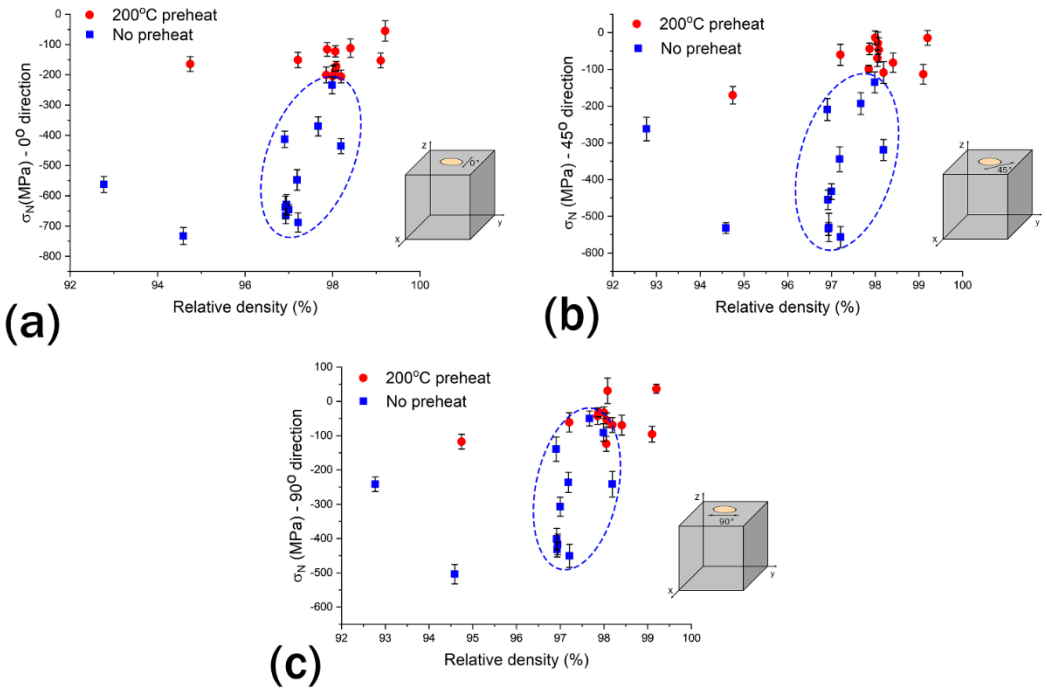

Figure 4-19 The variation in the normal residual stress on the top surface as a function of the relative density at orientations of: (a) 0°, (b) 45°, and (c) 90°. The test was performed at the center of the top surface designated by the yellow spot in the figures.

4.6.5 Aggregate effect of all contributing factors

This section combines all of the abovementioned contributing factors to discuss the measured residual stress profiles shown in Figure 4-11. Nevertheless, the provided arguments are also valid to compare the residual stress state and beam deflection of any other sample. Referring to Figure 4-11, the followings can be inferred:

(i) *Residual stress profile shape*: all of the samples share the same residual stress profile shape up to 1 mm below the top surface, starting from compressive stresses and shifting towards tensile stresses at a specific depth dictated by the employed E_v. Compressive residual stresses are observable at the very top layer in all

samples, meaning that the compressive residual stresses formed as a result of the martensitic phase transformation are dominant over the tensile ones in the currently solidified layer. As the build progresses, the previously consolidated layers with compressive nature of residual stresses undergo a complicated thermal cycle due to the layer-wise fashion of the LPBF process. This continuous thermal cycling of the previous layers will change the regime of residual stresses. That is why the compressive residual stresses turn into tensile below a specific depth dictated by the E_v. The residual stresses may continue to change periodically further from the top surface (Figure 4-16).

(ii) *In-plane isotropic residual stress:* By comparing the residual stress profiles for each sample in different orientations of 0, 45, and 90°, it can be concluded that the magnitude of residual stresses in every single plane of measurement along the Z-axis is independent of measurement orientation. This gives evidence of in-plane residual stress isotropy, which is a direct consequence of choosing a 67° rotation between consequent layers. This scanning strategy is believed to alleviate the formation of intense heating directionality between subsequent layers by repeating the same scanning direction every 180 layers [58].

(iii) *Effect of preheating:* As discussed earlier application of 200°C of preheating eliminated the cracking and improved the densification of the samples in one hand and reduced the contribution of martensitic phase transformation on the other hand. While the former led to the higher tensile residual stresses in the tensile zone, the latter created a lower magnitude of compressive stresses.

(iv) *Residual stress trends in each category:* among the parts D1, A3, and B3, the first one has the lowest magnitude of residual stress in both compressive and tensile

zones. The reason behind the lower compressive stress of this sample is lower E_v in conjunction with a lower level of densification. A3 and B3 samples have almost the same magnitude of the residual stresses in both compressive and tensile zones. From an E_v perspective, the residual stress needs to be more compressive in the B3 sample. However, since having a density lower than that of A3, B3 sample is expected to show a lower magnitude of the residual stresses. The balance of these two opposing factors causes the residual stresses to be close to each other. A parallel discussion is valid for the preheated samples.

4.6.6 Experimental vs simulation results

Figure 4-20 shows the CMM measurement as well as the FEA results of deflection profile in the Z-direction, along the length of the twin-cantilever beams for both with and without preheating conditions (A3 and PA3). Regardless of the preheating condition, the implemented model overestimated the level of beam deflection. It is mainly attributed to ignoring the martensitic phase transformation in the part-level analysis of the beam deflection of H13 tool steel due to the computational infeasibility of incorporating martensitic phase transformation, happening in a micro-scale. As thoroughly covered in section 4.6.1, the martensitic phase transformation causes significant compressive residual stresses (Figure 4-10 and Figure 4-11), especially in the non-preheated case. Absence of these compressive stresses resulted in larger beam deflections in the FEA model compared to the experimental measurements. In addition, the presence of macro-cracks in the A3 sample (Figure 4-8(c)) released some portion of the accumulated residual stresses in the fabricated part, which further increased the discrepancy between the model outcomes and

experimental measurement results. Since the PA3 sample is defect-free (Figure 4-8(f)), the defects cannot play a role in the observed difference between the model and experimental results.

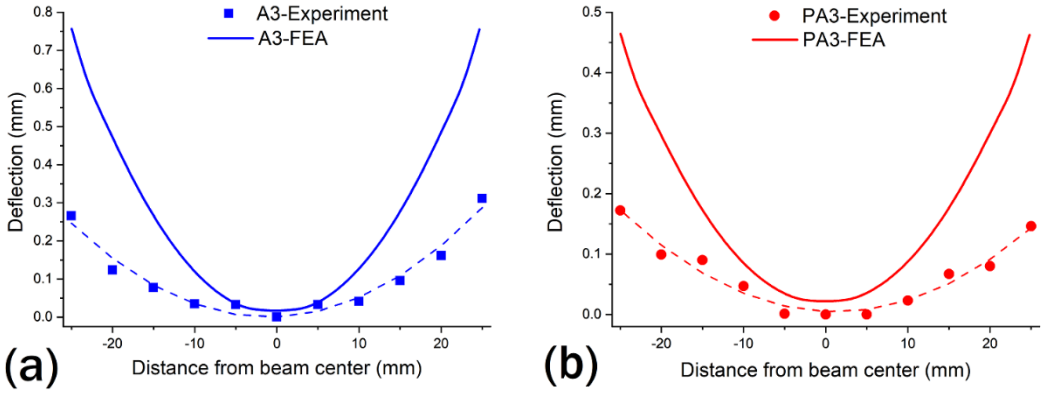

Figure 4-20 Experimental beam deflection measurement results versus the FEA of the twin-cantilever beam displacement in the Z-direction (U3) for (a) A3, and (b) PA3 samples. The implemented relaxation temperature was 800 K.

In the FEA results shown in Figure 4-20, the relaxation temperature, defined as a temperature above which thermal straining induces negligible thermal stress in the printing part, was set to be 800 K (Table 4-2). According to the part-level simulation of a twin-cantilever beam performed in ABAQUS (NIST AM Benchmark 2018 [29]) on IN625, the relaxation temperature was taken as 1023 K which is 70% of the annealing temperature of this alloy. The same percentage of the annealing temperature of H13 (1144 K) was implemented to obtain the FEA results in Figure 4-20. Although such a relation temperature selection worked reasonably well for IN625, it failed in the case of H13 tool steel in which a low-temperature martensitic phase transformation plays a crucial role in the regime of the residual stresses and the beam deflections. Therefore, to resolve the

observed discrepancies between the FEA and experimental results, a new relaxation temperature considering the microstructural evolutions should be introduced. Figure 4-21(a) schematically shows the variation of stress levels as a function of temperature during the cooling stage of the LPBF-processed H13 tool steel. Referring to Figure 4-1(thermal gradient model), the solidification of each track during LPBF process is accompanied by the generation of tensile thermal stresses since the previously consolidated layers oppose the contraction of the as-solidified material. The magnitude of these tensile thermal stresses shows an ascending trend as the temperature drops. When the Ms of H13 tool steel is reached, the further temperature drop is accompanied by the development of compressive stresses due to the martensitic phase transformation (Figure 4-15 (a)). These phase transformation-induced compressive stresses not only offset the tensile thermal stresses but also leave behind relatively large compressive stresses in the as-consolidated layer (Figure 4-10). A transition from tensile zone to the compressive implies a point in which the resultant stress is zero (Figure 4-21 (a)). The temperature at this point which is around the Ms of H13 tool steel could be used as the relaxation temperature for the FEA. As shown in Figure 4-21(b), there is a great agreement between the FEA results implementing this relaxation temperature (550 K) and the experimental measurements for the PA3 sample. This paves the way for a reliable simulation of beam deflection in LPBF processing of steels having low-temperature martensitic phase transformation.

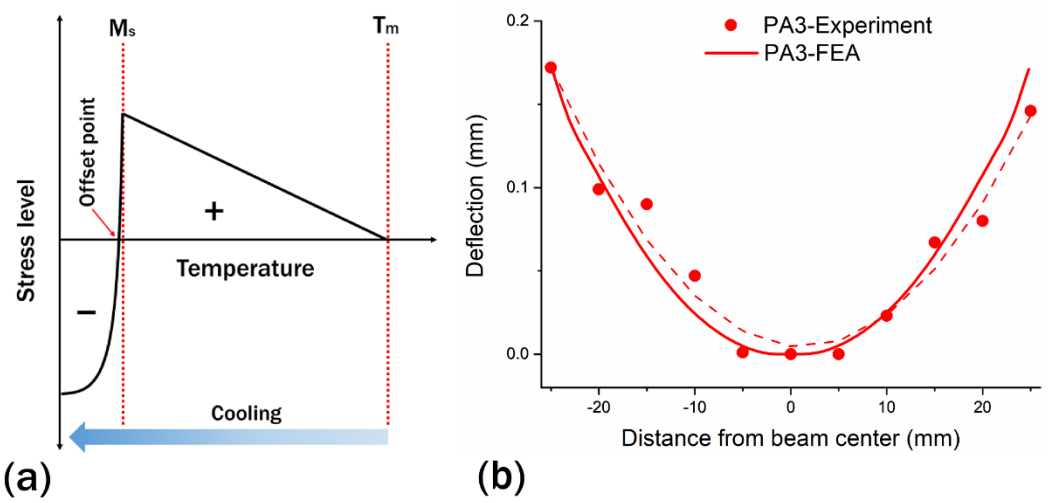

Figure 4-21 (a) Schematic illustration of the stress level as a function of the temperature during the cooling stage of the LPBF-processed H13 tool steel, and (b) experimental beam deflection measurement results versus the FEA of the twin-cantilever beam displacement in the Z-direction (U3) for PA3 sample. The implemented relaxation temperature was 550 K.

4.7 Conclusions

This study targeted the investigation of the residual stresses in the LPBF-processed H13 tool steel through direct (i.e., XRD) and indirect (i.e., twin-cantilever beam deflection) experimental measurements combined with the simulation. The following conclusions were drawn from the experimental and simulation results:

i. *Significant contribution of martensitic phase transformation:* The residual stress in the as-consolidated layer in LPBF process is usually tensile in nature. However, in the case of H13 tool steel, the martensitic phase transformation not only offsets the tensile stresses but also leaves behind a considerable amount of compressive residual stresses, especially in the non-preheated scenario. The impact of

martensitic phase transformation on the residual stress regime gets alleviated when preheating is applied. The complex nature of thermal cycling experienced by each consolidated layer during the build process can change the magnitude or nature of this compressive residual stress. Ignoring the martensitic phase transformation in the part-level simulation caused a discrepancy between the experimental and simulation results of beam deflections.

ii. *Direct proportionality between compressive residual stresses and E_v*: The residual stresses on the top surface of non-preheated test coupons grew more compressive by increasing the E_v in the range studied (40-130 J/mm^3). The shallower thermal gradients associated with higher E_v acts to decrease the tensile component of the residual stress, which in turn leads to the further dominancy of the pre-existing compressive component originating from the martensitic phase transformation.

iii. *Dependency of residual stresses on defects at low densification levels*: Increase in the densification level from 93% up to 97% resulted in larger residual stresses owing to the absence of porosities as empty spots with no load-bearing capability. However, above 97% relative density, the residual stress magnitude was independent of the extent of porosities. The same is valid for almost all of the preheated test samples with relative densities higher than 97.5%.

iv. *Formation of macro-cracks in non-preheated condition:* Almost all of the non-preheated samples had macro-cracks, giving evidence of thermal stresses exceeding the ultimate tensile strength of H13 tool steel. Formation of such cracks in the parts released a significant amount of accumulated stresses. Therefore, the residual stress measurement results of these samples demonstrate the aftermath of

cracking, which explains their lower magnitude compared to the preheated samples in the tensile zone of residual stress profiles.

Eliminating the need for stress-relief post-processing in the case of preheating: Application of 200°C preheating not only helped to avoid the formation of cracks but also led to the tensile stresses in the order of 300 MPa which are far away from the ultimate tensile strength of the H13 tool steel. Hence, the fabricated as-built part can be regarded as end-use components with no need for costly and time-consuming stress-relief post-processing treatments.

4.8 References

[1] A.I.H. Committee, ASM Handbook: Properties and selection, Asm International1990.

[2] D. Papageorgiou, C. Medrea, N. Kyriakou, Failure analysis of H13 working die used in plastic injection moulding, Engineering Failure Analysis 35 (2013) 355-359.

[3] R. Mertens, B. Vrancken, N. Holmstock, Y. Kinds, J.-P. Kruth, J. Van Humbeeck, Influence of powder bed preheating on microstructure and mechanical properties of H13 tool steel SLM parts, Physics Procedia 83 (2016) 882-890.

[4] M. Wang, W. Li, Y. Wu, S. Li, C. Cai, S. Wen, Q. Wei, Y. Shi, F. Ye, Z. Chen, High-temperature properties and microstructural stability of the AISI H13 hot-work tool steel processed by selective laser melting, Metallurgical and Materials Transactions B 50(1) (2019) 531-542.

[5] M. Mazur, M. Leary, M. McMillan, J. Elambasseril, M. Brandt, SLM additive manufacture of H13 tool steel with conformal cooling and structural lattices, Rapid Prototyping Journal (2016).

[6] M. Mazur, P. Brincat, M. Leary, M. Brandt, Numerical and experimental evaluation of a conformally cooled H13 steel injection mould manufactured with selective laser melting, The International Journal of Advanced Manufacturing Technology 93(1-4) (2017) 881-900.

[7] M. Katancik, S. Mirzababaei, M. Ghayoor, S. Pasebani, Selective laser melting and tempering of H13 tool steel for rapid tooling applications, Journal of Alloys and Compounds 849 (2020) 156319.

[8] L. Robert, Norton Machine Design; An Integrated Approach, Prentice-Hall, 1996.

[9] S. Taktak, Some mechanical properties of borided AISI H13 and 304 steels, Materials & design 28(6) (2007) 1836-1843.

[10] J. Mazumder, J. Choi, K. Nagarathnam, J. Koch, D. Hetzner, The direct metal deposition of H13 tool steel for 3-D components, Jom 49(5) (1997) 55-60.

[11] T. Mukherjee, J. Zuback, A. De, T. DebRoy, Printability of alloys for additive manufacturing, Scientific reports 6(1) (2016) 1-8.

[12] H.A. Abdulhadi, S.N.A.S. Ahmad, I. Ismail, M. Ishak, G.R. Mohammed, Thermally-induced crack evaluation in H13 tool steel, Metals 7(11) (2017) 475.

[13] W.E. Bryson, Heat Treatment, Selection, and Application of Tool Steels, (2005).

[14] E. Fereiduni, M. Elbestawi, Process-structure-property relationships in additively manufactured metal matrix composites, Additive Manufacturing of Emerging Materials, Springer2019, pp. 111-177.

[15] F. Bosio, A. Aversa, M. Lorusso, S. Marola, D. Gianoglio, L. Battezzati, P. Fino, D. Manfredi, M. Lombardi, A time-saving and cost-effective method to process alloys by Laser Powder Bed Fusion, Materials & Design 181 (2019) 107949.

[16] X. Song, S. Feih, W. Zhai, C.-N. Sun, F. Li, R. Maiti, J. Wei, Y. Yang, V. Oancea, L. Romano Brandt, A.M. Korsunsky, Advances in additive manufacturing process simulation: Residual stresses and distortion predictions in complex metallic components, Materials & Design 193 (2020) 108779.

[17] J. Günther, S. Leuders, P. Koppa, T. Tröster, S. Henkel, H. Biermann, T. Niendorf, On the effect of internal channels and surface roughness on the high-cycle fatigue performance of Ti-6Al-4V processed by SLM, Materials & Design 143 (2018) 1-11.

[18] I. Gibson, D.W. Rosen, B. Stucker, Additive manufacturing technologies, Springer2014.

[19] T. DebRoy, H.L. Wei, J.S. Zuback, T. Mukherjee, J.W. Elmer, J.O. Milewski, A.M. Beese, A. Wilson-Heid, A. De, W. Zhang, Additive manufacturing of metallic components – Process, structure and properties, Progress in Materials Science 92 (2018) 112-224.

[20] A. Bandyopadhyay, K.D. Traxel, Invited Review Article: Metal-additive manufacturing - Modeling strategies for application-optimized designs, Additive manufacturing 22 (2018) 758-774.

[21] T. Simson, A. Emmel, A. Dwars, J. Böhm, Residual stress measurements on AISI 316L samples manufactured by selective laser melting, Additive Manufacturing 17 (2017) 183-189.

[22] Z. Hu, R. Kovacevic, M. Labudovic, Experimental and numerical modeling of buckling instability of laser sheet forming, International Journal of Machine Tools and Manufacture 42(13) (2002) 1427-1439.

[23] M. Narvan, K.S. Al-Rubaie, M. Elbestawi, Process-Structure-Property Relationships of AISI H13 Tool Steel Processed with Selective Laser Melting, Materials 12(14) (2019) 2284.

[24] J. Krell, A. Röttger, K. Geenen, W. Theisen, General investigations on processing tool steel X40CrMoV5-1 with selective laser melting, Journal of Materials Processing Technology 255 (2018) 679-688.

[25] Z. Xiao, C. Chen, H. Zhu, Z. Hu, B. Nagarajan, L. Guo, X. Zeng, Study of residual stress in selective laser melting of Ti6Al4V, Materials & Design 193 (2020) 108846.

[26] M. Balbaa, S. Mekhiel, M. Elbestawi, J. McIsaac, On selective laser melting of Inconel 718: Densification, surface roughness, and residual stresses, Materials & Design 193 (2020) 108818.

[27] A. Hussein, L. Hao, C. Yan, R. Everson, Finite element simulation of the temperature and stress fields in single layers built without-support in selective laser melting, Materials & Design (1980-2015) 52 (2013) 638-647.

[28] Y. Li, K. Zhou, P. Tan, S.B. Tor, C.K. Chua, K.F. Leong, Modeling temperature and residual stress fields in selective laser melting, International Journal of Mechanical Sciences 136 (2018) 24-35.

[29] Y. Yang, M. Allen, T. London, V. Oancea, Residual strain predictions for a powder bed fusion Inconel 625 single cantilever part, Integrating Materials and Manufacturing Innovation 8(3) (2019) 294-304.

[30] M.F. Zaeh, G. Branner, Investigations on residual stresses and deformations in selective laser melting, Production Engineering 4(1) (2010) 35-45.

[31] K. Carpenter, A. Tabei, On Residual Stress Development, Prevention, and Compensation in Metal Additive Manufacturing, Materials (Basel) 13(2) (2020) 255.

[32] C. Li, C. Fu, Y. Guo, F. Fang, A multiscale modeling approach for fast prediction of part distortion in selective laser melting, Journal of materials processing technology 229 (2016) 703-712.

[33] I. Yadroitsev, I. Yadroitsava, Evaluation of residual stress in stainless steel 316L and Ti6Al4V samples produced by selective laser melting, Virtual and Physical Prototyping 10(2) (2015) 67-76.

[34] L. Bertini, F. Bucchi, F. Frendo, M. Moda, B.D. Monelli, Residual stress prediction in selective laser melting, The International Journal of Advanced Manufacturing Technology 105(1-4) (2019) 609-636.

[35] C. Li, Z. Liu, X. Fang, Y. Guo, On the simulation scalability of predicting residual stress and distortion in selective laser melting, Journal of Manufacturing Science and Engineering 140(4) (2018).

[36] I. Setien, M. Chiumenti, S. van der Veen, M. San Sebastian, F. Garciandía, A. Echeverría, Empirical methodology to determine inherent strains in additive manufacturing, Computers & Mathematics with Applications 78(7) (2019) 2282-2295.

[37] J.-P. Kruth, J. Deckers, E. Yasa, R. Wauthlé, Assessing and comparing influencing factors of residual stresses in selective laser melting using a novel analysis method, Proceedings of the institution of mechanical engineers, Part B: Journal of Engineering Manufacture 226(6) (2012) 980-991.

[38] M. Siewert, F. Neugebauer, J. Epp, V. Ploshikhin, Validation of Mechanical Layer Equivalent Method for simulation of residual stresses in additive manufactured components, Computers & Mathematics with Applications 78(7) (2019) 2407-2416.

[39] C. Li, J. Liu, X. Fang, Y. Guo, Efficient predictive model of part distortion and residual stress in selective laser melting, Additive Manufacturing 17 (2017) 157-168.

[40] D. Buchbinder, W. Meiners, N. Pirch, K. Wissenbach, J. Schrage, Investigation on reducing distortion by preheating during manufacture of aluminum components using selective laser melting, Journal of laser applications 26(1) (2014) 012004.

[41] X. Zhang, J. Kang, Y. Rong, P. Wu, T. Feng, Effect of Scanning Routes on the Stress and Deformation of Overhang Structures Fabricated by SLM, Materials 12(1) (2019) 47.

[42] Q. Chen, X. Liang, D. Hayduke, J. Liu, L. Cheng, J. Oskin, R. Whitmore, A.C. To, An inherent strain based multiscale modeling framework for simulating part-scale residual deformation for direct metal laser sintering, Additive Manufacturing 28 (2019) 406-418.

[43] L. Papadakis, A. Loizou, J. Risse, S. Bremen, J. Schrage, A computational reduction model for appraising structural effects in selective laser melting manufacturing: a methodical model reduction proposed for time-efficient finite element analysis of larger components in Selective Laser Melting, Virtual and Physical Prototyping 9(1) (2014) 17-25.

[44] B. Vrancken, R. Wauthlé, J.-P. Kruth, J. Van Humbeeck, Study of the influence of material properties on residual stress in selective laser melting, Proceedings of the solid freeform fabrication symposium, 2013, pp. 393-407.

[45] M. Bugatti, Q. Semeraro, Limitations of the inherent strain method in simulating powder bed fusion processes, Additive Manufacturing 23 (2018) 329-346.

[46] S. Ghosh, J. Choi, Modeling and Experimental Verification of Transient/Residual Stresses and Microstructure Formation in Multi-Layer Laser Aided DMD Process, Journal of Heat Transfer 128(7) (2005) 662-679.

[47] N.S. Bailey, C. Katinas, Y.C. Shin, Laser direct deposition of AISI H13 tool steel powder with numerical modeling of solid phase transformation, hardness, and residual stresses, Journal of Materials Processing Technology 247 (2017) 223-233.

[48] A. Standard, E915, 2010," Standard Test Method for Verifying the Alignment of X-Ray Diffraction Instrumentation for Residual Stress Measurement," ASTM International, West Conshohocken, PA, 2003, DOI: 10.1520/E0915-10.

[49] E.O. Olakanmi, Selective laser sintering/melting (SLS/SLM) of pure Al, Al–Mg, and Al–Si powders: Effect of processing conditions and powder properties, Journal of Materials Processing Technology 213(8) (2013) 1387-1405.

[50] Abaqus User's Manual, https://help.3ds.com/2019x/English/DSDoc/FrontmatterMap/DSDocHome.htm?ContextScope=onpremise, 2019.

[51] I.R. Kabir, D. Yin, N. Tamanna, S. Naher, Thermomechanical modelling of laser surface glazing for H13 tool steel, Applied Physics A 124(3) (2018) 260.

[52] Y. Woo, T. Hwang, I. Oh, D. Seo, Y. Moon, Analysis on selective laser melting of WC-reinforced H13 steel composite powder by finite element method, Advances in Mechanical Engineering 11(1) (2019) 1687814018822200.

[53] R. Besler, M. Bauer, K.P. Furlan, A.N. Klein, R. Janssen, Effect of Processing Route on the Microstructure and Mechanical Properties of Hot Work Tool Steel, Materials Research 20 (2017) 1518-1524.

[54] J.J. Yan, D.L. Zheng, H.X. Li, X. Jia, J.F. Sun, Y.L. Li, M. Qian, M. Yan, Selective laser melting of H13: microstructure and residual stress, Journal of Materials Science 52(20) (2017) 12476-12485.

[55] M.J. Holzweissig, A. Taube, F. Brenne, M. Schaper, T. Niendorf, Microstructural Characterization and Mechanical Performance of Hot Work Tool Steel Processed by Selective Laser Melting, Metallurgical and Materials Transactions B 46(2) (2015) 545-549.

[56] S. Van Bohemen, J. Sietsma, Martensite formation in partially and fully austenitic plain carbon steels, Metallurgical and Materials Transactions A 40(5) (2009) 1059-1068.

[57] K. Andrews, J Iron Steel Inst, July 203 (1965) 721.

[58] R. Casati, J. Lemke, M. Vedani, Microstructure and fracture behavior of 316L austenitic stainless steel produced by selective laser melting, Journal of Materials Science & Technology 32(8) (2016) 738-744.

Chapter 5

Laser Powder Bed Fusion of Functionally Graded Bi-Materials: Role of VC in Functionalizing AISI H13 Tool Steel

Complete Citation:

Morteza Narvan, Ali Ghasemi, Eskandar Fereiduni, and M. A. Elbestawi, " Laser Powder Bed Fusion of Functionally Graded Bi-Materials: Role of VC in Functionalizing AISI H13 Tool Steel. " *Materials & Design* Journal January 2021

https://doi.org/10.1016/j.matdes.2021.109503

Abstract:

This study investigates the feasibility of fabricating defect-free functionally graded bi-materials (FGMs) with enhanced wear resistance via incorporation of vanadium carbide (VC) into H13 tool steel. Three distinct composite powders containing 1, 3, and 5wt.%VC were prepared through ball-milling and subjected to laser powder bed fusion (LPBF) process to print different composites on top of monolithic H13 in a wide range of process parameters. Almost fully-dense parts were achieved (maximum of 99.8, 99.8, and 99.5% for 1, 3 and 5wt.%VC composite systems, respectively); however, the increase in VC content narrowed down the processability window range from 60 J/mm3 for 1, and 3wt.%VC systems to 30 J/mm3 for 5wt.%VC system. The mechanical properties of optimum samples were characterized through microhardness, nanohardness, and wear tests. The incorporation of VC significantly improved the mechanical properties, 17-40% in microhardness, 10-40% in nanohardness, and 20-53% in wear resistance. The underlying reasons behind such an improvement were correlated to the dissolution of VC during the heating stage of the LPBF process and the formation of (V+C)-supersaturated solid solution in large extents as a result of extremely high cooling rates. This study introduces LPBF-processed FGMs as promising candidates for applications in which wear resistance is paramount.

Keywords:

Laser powder bed fusion (LPBF); functionally graded material (FGM); Wear resistance; H13 tool steel; vanadium carbide (VC) ceramic particles; Supersaturated solid solution.

Acknowledgment:

The optical absorption measurements in this study were performed at the Department of Materials Engineering, KU Leuven, Belgium. We would like to thank Suraj Dinkar Jadhav and Dr. Kim Vanmeensel for providing us with these measurements.

Graphical Abstract:

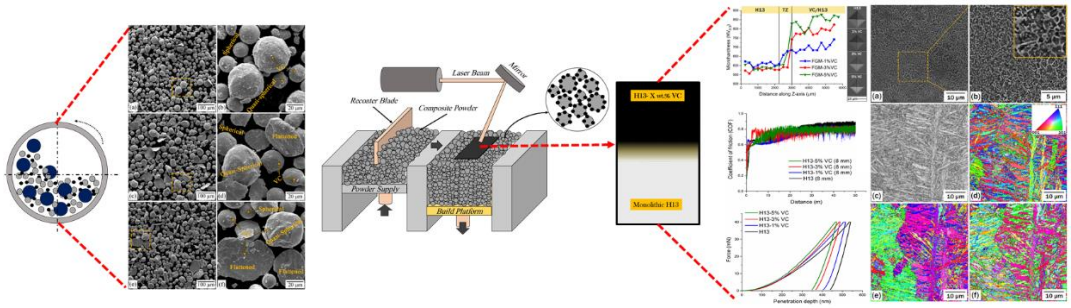

5.1 Introduction

The emergence of laser powder bed fusion (LPBF) as a novel layer-by-layer additive manufacturing (AM) technique has provided an unprecedented opportunity in many technological fields, including injection molding applications to change the concept of design from "design for manufacturing" to "design for performance" [1-4]. The manufacturing of the conformally-cooled injection molds with 20-50% improvement in the cooling efficiency compared to the conventional molds with machined cooling channels can be considered as one of the revolutions in the injection molding industry, which became feasible after the birth of LPBF [5-7]. Based on the printability studies focused on LPBF of stainless steels (e.g., AISI 316) [8, 9], maraging steels (e.g., maraging 300) [10-13] and tool steels (e.g., H11 and H13) [14-18] as the suitable candidates for injection molding applications, it can be concluded that the manufacturing of almost defect-free components with high dimensional accuracy is possible through the LPBF process.

Among the various studied materials, the H13 tool steel has found a great deal of attention as the prime nominee for injection molding applications due to the higher hardness and wear resistance compared to the AISI 316 stainless steel and cost advantages over the maraging steels and many other tool steels [6, 19]. The combination of toughness, moderate hardness, and heat check resistance, defined as the resistance to the quench cracking phenomenon occurring as a result of the dynamic heating and cooling of the molds, is believed to be the major reason behind the widespread acceptance of H13 as a versatile steel for molding applications [20, 21]. However, compared to the other members of the tool steel family, H13 has the minimum hardness, which increases the chance of the wear damage failure in service. Although a hardness value up to 52 HRC at ambient temperature is achievable in as-built LPBF parts or through heat treatment of wrought H13 tool steel

[22, 23], it is still considerably lower than the average hardness value of highly wear-resistant tool steels (higher than 60 HRC) [24, 25]. The design requirements and the interest in life extension of the molds necessitate enhancing wear resistance of H13 to improve the molds' performance and reduce the repair/replacement costs [26, 27]. At the current stage, the service temperature of H13 cannot exceed 550°C due to the sharp decrease in the hardness and therefore wear resistance of this alloy over this critical temperature (40 HRC at 625°C) [28, 29]. Therefore, the enhancement of high-temperature hardness is also essential to widen the allowable working temperature of H13 molds.

As a general rule, the wear resistance of tool steels is tied to the concentration of carbon and their carbide former alloying elements since they promote the formation of carbides as the hard particles and consequently enhance the hardness of the alloy [29, 30]. Therefore, one approach to improve the limited wear resistance of H13 is to increase the volume fraction of carbides through "alloying" or "reinforcing" mechanisms by either addition of strong carbide former elements (e.g., vanadium) to manipulate the chemical composition of H13 or incorporation of hard carbide particles (e.g., VC) to create a metal matrix composite (MMC) [31-33]. By considering the flexibility in alloy and composite design through the LPBF process simply by utilizing the alloying agent/H13 or reinforcing agent/H13 powder mixtures, this approach is completely feasible. However, it should be borne in mind that the increase in the volume fraction of carbides should be controlled to have the least influence on the toughness of H13. Otherwise, the limited toughness can also cause premature failure of the molds. According to the knowledge gained from the chemistry of H13 (V is in the alloying recipe) and other tool steels such as CPM-xV alloys, the addition of carbon and vanadium (i.e., VC carbide) to H13 can be an effective strategy to end up with a material having comparable toughness to that of H13 along with the

significantly higher wear resistance [34, 35]. The sharp decrease in the hardness of the H13 over 550°C can also be compensated by the increase in hardness caused by the presence of the reinforcing VC particles, enabling higher working temperatures.

While the literature has mostly focused on improving the mechanical properties of austenitic stainless steels by incorporating hard TiB2, TiC, or VC particles [33-36], reinforcing H13 to enhance its wear resistance has received only scant attention. Yet there is a few published information on the subject, most of which was reported before the emergence of additive manufacturing or centered around other manufacturing techniques [32, 36, 37]. This paper aims at answering this question that whether or not the wear resistance of the H13 can be upgraded by the addition of hard VC particles. Three different VC/H13 composite powder systems with varying VC concentrations ranging from 1-5 wt.% were pre-processed and subjected to the LPBF process in a wide range of process parameters. Density measurement results revealed that the sound composite parts having densities higher than 99.5% are achievable by proper selection of the process parameters. The optimum fabricated composites were compared in terms of microhardness, nanohardness, wear resistance, and coefficient of friction. The obtained trends in different mechanical properties were backed up by in-depth microstructural characterizations. It is believed that the surface modification of the current H13 molds with the proposed optimum VC/H13 composite system can not only increase the lifetime of the molds but also enhance their allowable working temperature.

5.1 Materials and methods

5.1.1 Composite powder preparation

The powders used in this study were H13 with the nominal chemical composition and particle size distribution provided in [14] and VC with 99.9% purity and particle size < 2µm. The morphology of these powders can be observed in Figure 5-1. The H13 powder has been fabricated by the gas atomization process and is characterized by highly spherical particles (Figure 5-1 (a)). However, non-spherical particles, as well as satellites, can also be found in this powder. As shown in Figure 5-1 (b), VC powder particles are irregular in shape and tend to form agglomerates due to their relatively high surface-to-volume ratio (i.e., high van der Waals attraction force). The ball milling process was performed using a high-performance planetary Pulverisette 6 machine to prepare the composite powder feedstock containing 1, 3, and 5wt.% VC, using a fixed rotational speed of 200 rpm and a mixing time of 1-3 h. The ball-to-powder weight ratio was 5:1, and every 30 min of mixing was followed by a 15 min break to avoid the temperature rise during the process. The added balls were made of hardened stainless steel with a diameter of 10 mm.

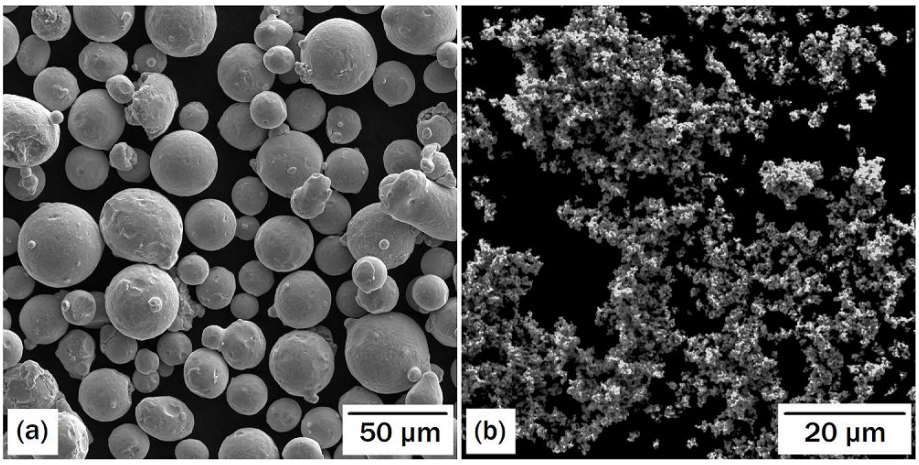

Figure 5-1 SEM micrographs of: (a) H13, and (b) VC powders.

5.1.2 Powder characterization

The optical absorption of H13 powder, as well as the developed composite powders, were measured in the wavelength range of 400-1400 nm by means of diffuse reflectance spectroscopy (DRS) using a UV-Visible-NIR LAMBDA 950 Perkin Elmer spectrophotometer equipped with a 150 mm diameter integrating sphere coated with Spectralon with a spectral resolution of 1 nm. To perform the test, powder samples were placed in a quartz cuvette and sealed prior to mounting on a Teflon sample holder. The reference material was Barium Sulfate powder with a reflectance of 100%, and the light sources were Deuterium (D2) and Tungsten with the wavelength ranges of 200-320 and 320-2500 nm, respectively. Photon Counting photomultiplier tubes (PMT) and Lead Sulfide (PbS), applicable in the wavelength ranges of 200-860 and 860-2500 nm, respectively were used as detectors.

The flowability and packing density of H13 and composite powders were assessed using the specific energy (SE) and the conditioned bulk density (CBD) indices of the FT4 Freeman powder rheometer, as thoroughly explained in [38, 39]. The precision blade's interaction with the powder in this technique resembles that of recoater/powder in the LPBF process.

5.1.3 LPBF processing

The LPBF machine used in this study was an EOS M280 (EOS, Krailling, Germany) equipped with a Yb-fiber laser system and delivers power levels of up to 400 W. High purity N_2 was used to reduce the oxygen content in the build chamber to less than 0.8%. For microstructural characterizations, functionally graded bi-material (FGM) cylindrical parts with a diameter of 10 mm and the height of 6.3 mm were printed on a steel build plate

preheated to 200 °C. Wear test specimens were also printed on the same plate with the same height but with a different diameter of 30 mm. For all sets of samples, the material for the first 3.3 mm of the height was non-reinforced H13, which was printed with the optimum process parameters reported in [14]. However, the next 3 mm was manufactured using 1, 3, and 5wt.%VC-H13 composite powder and various process parameters, as listed in Table 5-1. Using the same layer thickness and hatch spacing as those of the non-reinforced H13, different combinations of laser power and scanning speed were employed in the composite case to obtain volumetric energy densities lower and higher than the optimum value found in [14]. Scanning of layers was conducted using a stripe scanning strategy alternating 67° between subsequent layers. Samples were cut off the build plate via wire-cut electric discharge machining (EDM).

Table 5-1 Process parameters used in this study to fabricate the composite side of the FGMs

Sample	*P (W)*	*v (mm/s)*	*h (mm)*	*t (mm)*	e_v *(J/mm^3)*
1	200	600	0.08	0.04	104.2
2	200	800	0.08	0.04	78.1
3	200	1000	0.08	0.04	62.5
4	200	1200	0.08	0.04	52.1
5	250	600	0.08	0.04	130.2
6	250	800	0.08	0.04	97.6
7	250	1000	0.08	0.04	78.1
8	250	1200	0.08	0.04	65.1
9	300	600	0.08	0.04	156.2
10	300	800	0.08	0.04	117.2
11	300	1000	0.08	0.04	93.7
12	300	1200	0.08	0.04	78.1

According to the literature, the volumetric energy density can be obtained based on the following well-known equation [40]:

$$e_v = \frac{P}{vht} \quad \text{Eq. 1}$$

in which *P*, *v*, *h*, and *t* denote the laser power, scanning speed, hatch spacing, and the nominal powder layer thickness, respectively. The platform displacement during the LPBF process is mistakenly referred to as the powder layer thickness [41]. Although this definition works for the first deposited powder layer, it is not valid for the other layers due to the presence of inter-particle pores in the powder bed. In other words, consolidation of the first powder layer after laser processing is accompanied by a shrinkage since the liquid formed during the melting stage fills the interstices and creates a dense layer with a lower thickness (Figure 5-2(a,b)). Consequently, a gap is formed between the recoating blade and the top surface of the consolidated layer, which should be filled by powder during the second layer's deposition (Figure 5-2(c,d)). This simply means that the powder layer thickness will deviate from the nominal value (platform displacement) after the first layer's consolidation. The amount of increase in the powder layer thickness follows a descending trend in the consequent layers and finally approaches a constant value. This constant value is known as "effective powder layer thickness (t_{eff})" (actual powder layer thickness) [42] and is higher than the nominal value (platform displacement).

In this study, instead of using nominal powder layer thickness, t_{eff} is substituted in Eq.1. Besides, since only a fraction of the laser power is absorbed by the powder, the laser absorptivity coefficient (A) is added to this equation, which can be measured through the diffusion reflectance spectroscopy (DRS) test (section 5.1.2). The modified equation is as follows [38]:

$$E_v = \frac{AP}{vht_{eff}} \quad \text{Eq. 2}$$

This modified equation takes the effect of not only the process parameters but also the powder properties and laser-powder interactions into consideration. In most of the research studies where a fixed powder system is used, the application of this equation would only shift the energy input results to lower values. However, when it comes to comparing a monolithic powder and its composites, application of Eq. 1 would be misleading. Therefore, in addition to e_v, the E_v (Eq. 2) was also used in this study to provide a more accurate insight into the effect of energy density on the processability of different powder systems.

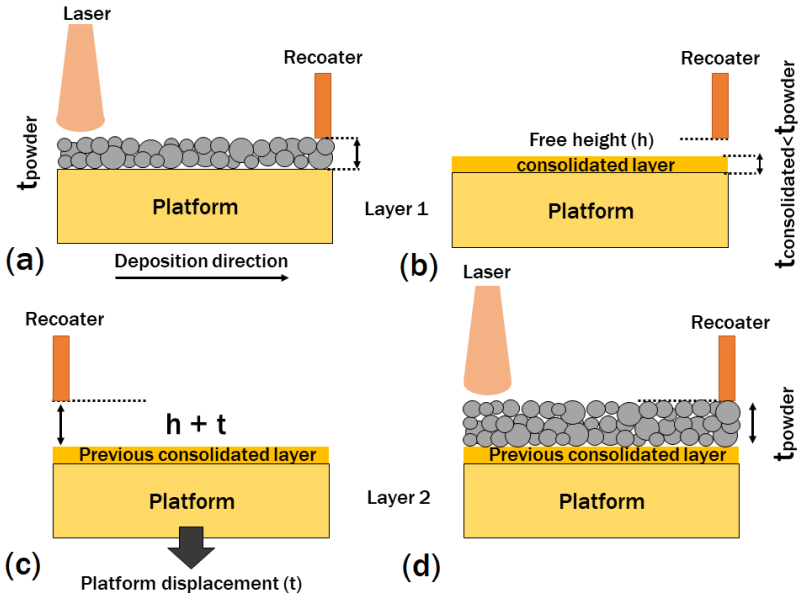

Figure 5-2 Schematic illustration of powder deposition and consolidation for a powder bed with a platform displacement of t: (a) deposition of the first powder layer with a thickness equal to that of the platform displacement (t_{powder}=t), (b) consolidation of the first layer after laser processing and formation of a free height (h), (c) incremental downward movement of the platform (t) before deposition of the next layer, and (d) deposition of the second powder layer with a thickness higher than the nominal value due to the formation of the free height after the solidification of the previous layer.

5.1.4 Microstructural observations

For microstructural characterization, the 10 mm diameter specimens were sectioned along their height and were ground using SiC papers with different meshes followed by polishing according to the standard metallographic procedure. The non-etched polished sections were analyzed by a Keyence (Osaka, Japan) VHX digital optical microscope to observe the defects in parts. Images acquired by the optical microscopy were used to measure the relative density of the composite sides of the FGMs via image processing. The polished sections were then chemically etched with 4% Nital reagent and were characterized using a Nikon LV100 optical microscope and a Vega Tescan scanning electron microscope (SEM) equipped with energy-dispersive X-ray spectroscopy (EDS). For the electron backscattered diffraction (EBSD) analysis, JEOL JSM-7000F equipped with a Schottky field emission gun was employed. The aforementioned sample preparation was followed by a 5 min of polishing on a chemical resistant cloth with a colloidal silica suspension, and finally a 4 h vibratory polishing with the same suspension. The data collection was performed using a 0.1 μm step size on an area of 50×50 μm^2. AZtecHKL software was used to post-process the collected data. The phase analysis was carried out using X-ray Diffraction (XRD) on a Bruker D8 DISCOVER with a DAVINCI design diffractometer equipped with a copper sealed tube source and a VANTEC-500 area detector.

5.1.5 Mechanical testing

The mechanical properties of fabricated parts were evaluated using microhardness and nanohardness measurements. Microhardness measurements were utilized using a Matsuzawa microhardness testing machine with a load of 500 g being applied for 10 s. The

reported microhardness value for each specimen represents an average of at least 5 distinct measurements.

Nanoindentation measurements were made using an Anton Paar NHT^3 nanoindentation tester (Anton Paar, Graz, Austria) equipped with a Berkovich pyramidal-shaped indenter tip. Calibration was performed before nanoindentation tests using a Fused Silica reference sample. The nanoindentation test was performed on the polished surface of the X-Z plane for both non-reinforced H13 and 1, 3, and 5wt.%VC-H13 composite parts. The maximum load, loading/unloading rate and the pause at the maximum load were 40 mN, 80 mN/min and 10 s, respectively. To determine the hardness and elastic modulus, the Oliver-Pharr method was used.

Anton Paar, standard TRB^3 tribometer was utilized to perform ball-on-disk wear test according to ASTM G99-95a [43]. A 6 mm diameter alumina ball subjected to a normal load of 10 N rubbed against the top surface of samples at 25°C and 43.55% room temperature and atmospheric humidity, respectively. The tests were performed on three distinct radii of 4, 6, and 8 mm on the surface of each sample. The rotation speed and the acquisition rate were set to be 150 rpm and 100 Hz. Worn tacks were investigated with an Alicona microscope to get the wear depth and width on three distinct spots for each radius to calculate the wear rate.

5.2 Results and discussions

5.2.1 Powder characterization

5.2.1.1 Selection of the appropriate composite powder feedstock

Figure 5-3 shows the 1wt.%VC-H13 composite powders' micrographs developed by 1, 2 and 3 h of ball milling. As can be observed in Figure 5-3(a,b), most of the H13 powder particles preserved their spherical shape; however, some particles showed a slight deviation from their starting spherical shape. The increase in the mixing time to 2 h was found to change the shape of a noticeable amount of H13 particles from spherical to irregular/flattened (Figure 5-3(c,d)). Further enhancement of the mixing time to 3 h led to much more powder particles losing their spherical morphology (Figure 5-3(e,f)). The change in H13 powder particles' shape can be attributed to the plastic deformation imparted to the composite powder system during the ball milling process. Longer milling times caused the deformation of more H13 powder particles in the composite powder system by enhancing the number of collisions (ball-powder-ball and ball-powder-wall). Microstructural observations also revealed that VC particles were almost fully attached to H13 powder particles' surface in the 1 h milled composite powder (Figure 5-3(b)). While most of the VC particles could still be observed on the surface of H13 particles in the 2 and 3 h milled systems, the increase in the mixing time favored their embedment in the H13 particles. This can be confirmed by the presence of lower numbers of VC particles existing on the surface of H13 particles in the 3 h milled composite powder compared to those in the 1 h milled case (Figure 5-3(b,f)).

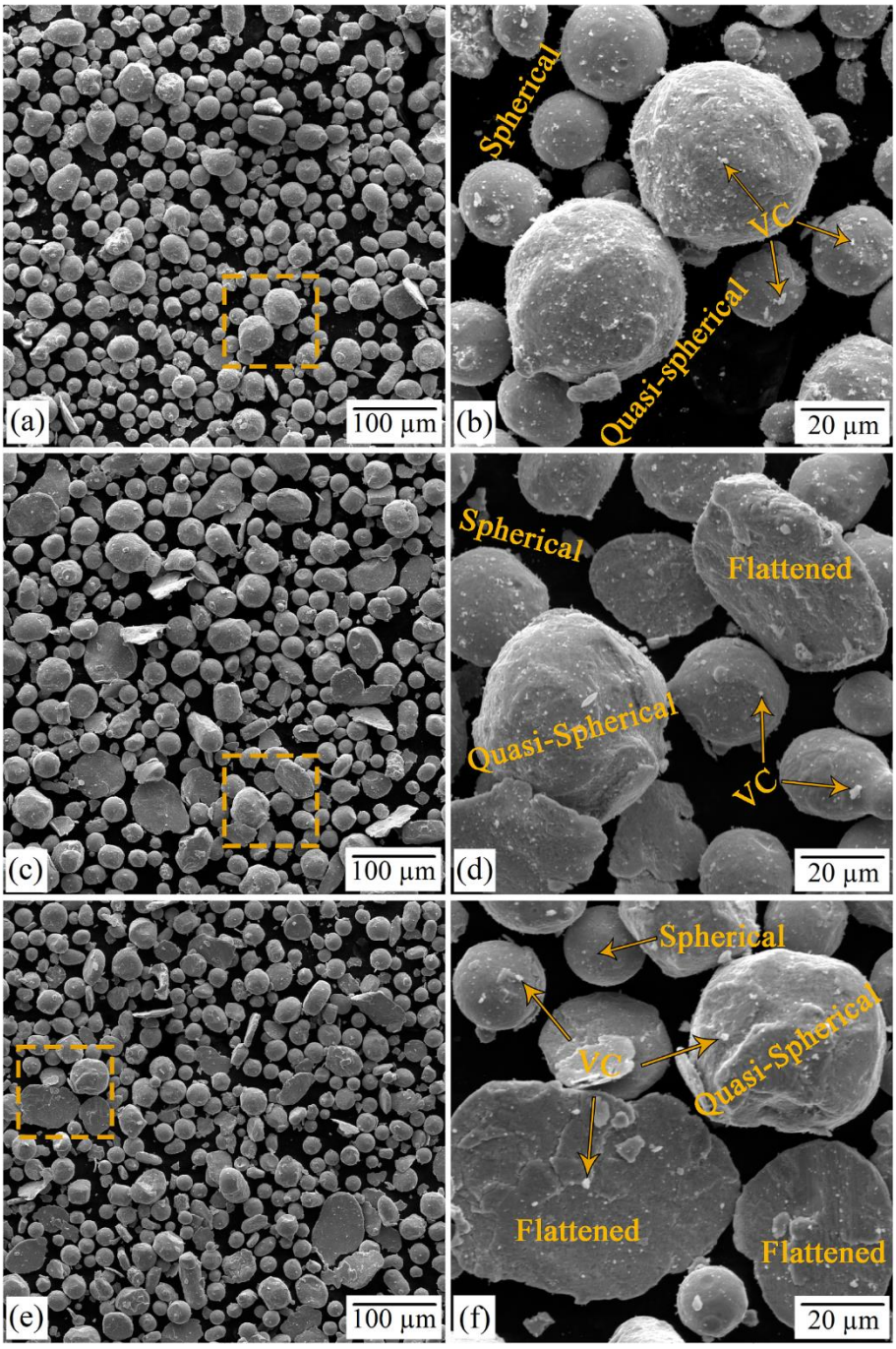

Figure 5-3 SEM micrographs of the 1wt.%VC-H13 composite powders produced by ball milling with mixing times of: (a, b) 1 , (c, d) 2 and (e, f) 3 h. Enclosed view of the selected squares in (a), (c) and (e) are provided in (b), (d) and (f), respectively.

The composite powder obtained by 1 h of ball milling was used in this study for LPBF processing due to two major reasons:

(i) Almost all of the VC particles have adhered to the surface of H13 powder particles. This attachment is required in the composite powders since it avoids the separation [39] of powder constituents caused by the difference in their density, and it decreases the agglomeration probability of the VC particles [44].

(ii) Most of the H13 particles have preserved their spherical morphology. In general, the deviation from the fully spherical morphology results in the decreased powder flowability due to the increased surface-to-volume ratio and consequently the elevated inter-particle friction. Therefore, compared to the 2 and 3 h milled powders, the composite system subjected to 1 h of milling is believed to show a flowability closer to that of the monolithic H13 powder (Section 5.2.1.2).

The mixing time of 1 h, as the optimum mixing time, was also employed to produce composite powders containing 3 and 5wt.%VC. As shown in Figure 5-4, these composite powders share the same features as those of the 1wt.%VC-H13 composite powder, with the only difference being that some VC particles remained non-attached to the surface of H13 particles. Although this might decrease the flowability of the developed composite powders, full attachment of VC particles through the application of longer milling times may not be helpful since the deviation from the spherical morphology can significantly worsen the flowability [39].

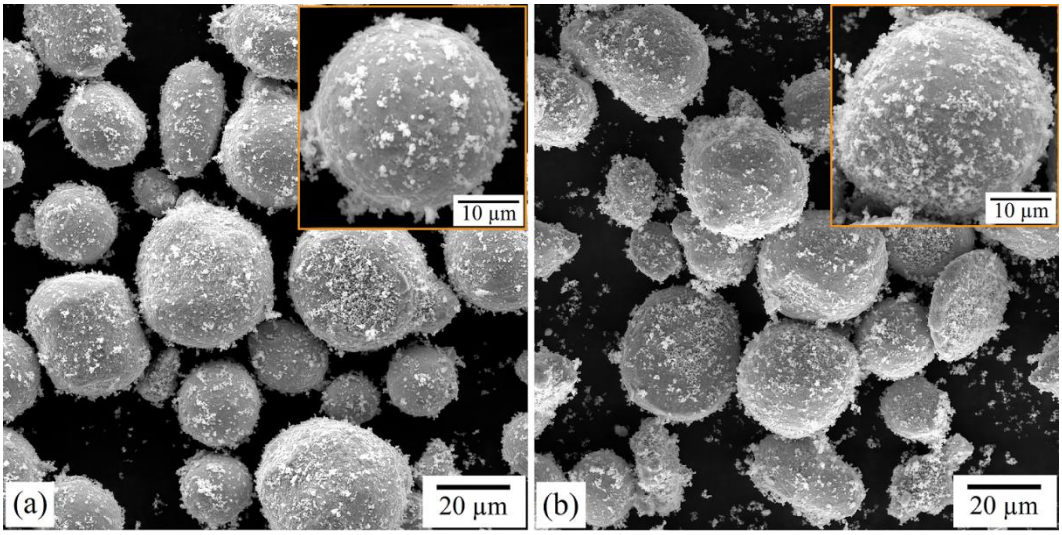

Figure 5-4 SEM micrographs of the: (a) 3wt.%VC-H13 and (b) 5wt.%VC-H13 composite powders produced by 1 h of ball milling.

5.2.1.2 Flowability and packing density

The flowability and packing density of powders play significant roles in the quality of the LPBF-processed parts. Figure 5-5(a) compares the flowability of the developed composite powders with that of the monolithic H13 powder in terms of specific energy (SE). Higher SE represents a lower powder flowability. Composite powders with 1, 3, and 5wt.%VC showed 18.4, 45.9, and 59% higher SE than that of the monolithic H13 powder, respectively. Since most of the H13 powder particles in the composite systems have preserved their spherical shape, the observed reduction in the flowability of composite powders should be traced back to the decorating VC particles. By acting as mechanical interlocking sites [45], these particles adversely affect the free flow of powder particles. The higher fraction of decorating VC particles is accompanied by creating much more particle entanglement, which justifies the trend observed in Figure 5-5(a).

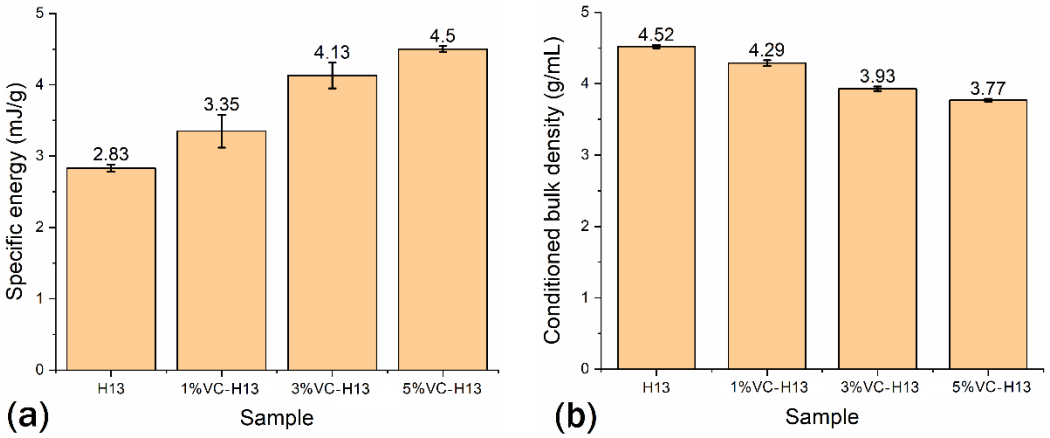

Figure 5-5 (a) The flowability in terms of specific energy (SE) index, and (b) the conditioned bulk density (CBD) of monolithic H13 and composite powders containing 1, 3, and 5wt.% VC.

5.2.1.3 Optical absorption

The laser absorptivity, defined as the ratio of the absorbed to the incident laser irradiation, is believed to be a direct indicative of the LPBF processability of a material. The optical absorption versus the wavelength is shown in Figure 5-6 for the monolithic H13 as well as the developed composite powder systems. As it is evident, the optical absorption of composite powders is higher than that of the monolithic H13 regardless of the investigated wavelength. In addition, the optical absorption showed an ascending trend by increasing the amount of VC constituent. At the wavelength of the LPBF machine used in this study (1070 nm), the addition of 1, 3, and 5wt.% VC increased the optical absorption of H13 from 61.5% to 71, 77.1, and 79.9%, respectively. This can be attributed to:

(i) Decoration of H13 particles by highly absorptive ceramic particles (i.e., VC): The laser-powder interaction is known to be a surface phenomenon. The decoration of H13 powder particles by VC particles introduces new sources of laser-material

interaction on the surface of H13 particles. Due to the higher optical absorption of the VC than that of the H13 powder, the substitution of H13 by VC on the surface leads to the increased optical absorption. The enhanced surface coverage of H13 powder particles (Figure 5-3(b) and Figure 5-4) caused by the increase in VC content elevates the overall optical absorption of the composite powders. Based on the image analysis results, the surface decoration percentage increased from 5.5±1.12 to 11.1±2.56 and then 16.5±4.87 when increasing the VC content from 1 to 3 and 5wt.% in the composite powder systems.

(ii) Multiple absorptions and reflections during the optical ray-powder interactions: Regardless of the type of the second powder constituent incorporated into the composite powder systems, decoration of the metallic powder by the ceramic particles has been shown to escalate the frequency of laser absorptions and reflections during the laser-powder interactions [46].

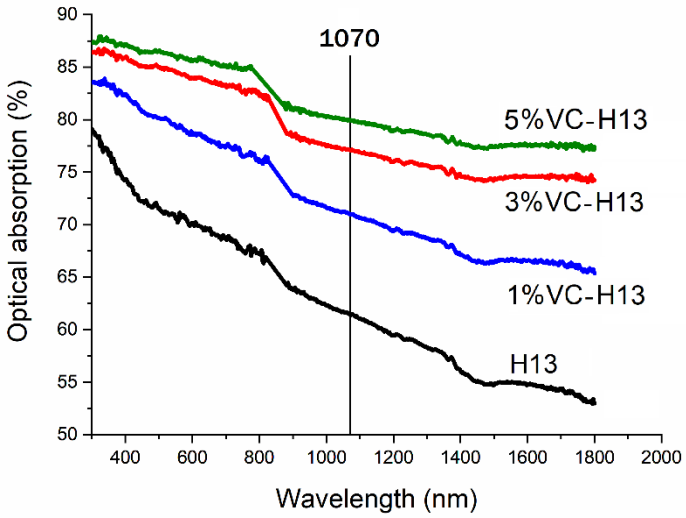

Figure 5-6 The optical absorption versus the wavelength for monolithic H13 and composite powders containing 1, 3, and 5wt.% VC. 1070 nm line indicates the wavelength of the laser in the LPBF machine used in this study.

5.2.2 Processability of FGMs

As mentioned before, the fabricated FGMs are composed of two sections of monolithic H13 (bottom) and VC-H13 composite (top). The H13 side in all of the FGMs was fabricated by the optimum set of process parameters (P = 300 W, v = 1000 mm/s, h = 0.08 mm, and t = 0.04 mm with an e_v equal to 93 J/mm^3) [14]. However, a wide range of process parameters was employed to fabricate the composite side of the FGMs. Figure 5-7 shows the relative density of the composite side of FGMs as a function of the employed e_v, which only considers the influence of process parameters. In all cases, the relative density first increased and then followed a decreasing trend by increasing the e_v. The optical micrographs corresponding to FGM-1wt.%VC, FGM-3wt.%VC, and FGM-5wt.%VC samples are also shown in Figure 5-8, Figure 5-9, and Figure 5-10, respectively. Parts with relative densities higher than 99% were achievable within a wide range of e_v for FGM-1wt.%VC and FGM-3wt.%VC cases. Only three of the fabricated samples showed relative densities lower than 99% in these systems. However, the 5wt.%VC-H13 system featured inferior processability, where only a few samples possessed a relative density exceeding 99%. Therefore, it is reasonable to conclude that the e_v range leading to highly dense samples becomes narrower as the content of VC increases. It is interesting to note that the processability of 3wt.%VC-H13 and 5wt.%VC- H13 composites was slightly better than that of the 1wt.%VC-H13 at e_v levels higher than 100 and 130 J/mm^3, respectively. This is due to the fact that the onset of the decreasing trend, where the highest relative density is obtained, shifts towards higher e_v levels with an increase in the VC content. Hence, the e_v values that are considered higher than optimum for the 1wt.%VC-H13 are still in the processable window for 3wt.%VC-H13 and 5wt.%VC-H13 systems. The optimum samples for the 1, 3 and 5wt.%VC composite systems had relative densities of 99.8, 99.8,

and 99.5% which were achieved at e_v levels corresponding to 104.2 (sample 1), 117.2 (sample 10), and 130.2 J/mm3 (sample 5), respectively (Table 5-1).

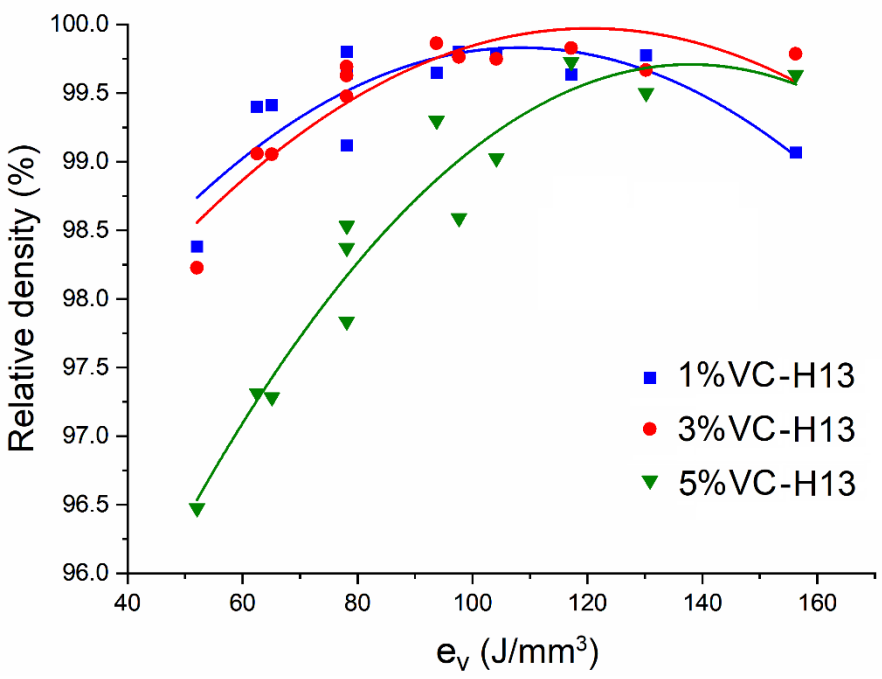

Figure 5-7 The relative density versus e_v for the composite side of the FGMs containing 1, 3, and 5wt.%VC.

At low e_v levels, the perceptible irregular-shape porosities originating from the lack of sufficient overlap between two successive tracks and/or layers are the main reason behind the relatively low density of the fabricated samples [47] (see insets in Figure 5-8(d), Figure 5-9(d), and Figure 5-10(d)). At relatively high ev levels, on the other hand, another mechanism of defect formation came into action, known as keyhole effect. The instability, as well as repeated formation and collapse of these keyholes, results in the generation of gas bubbles in the melt pool, which may lead to porosities in the final part if captured by the solidification interface. The porosities formed under such mechanism are characterized by their spherical/semi-spherical shape [48] (see the inset in Figure 5-8(i)).

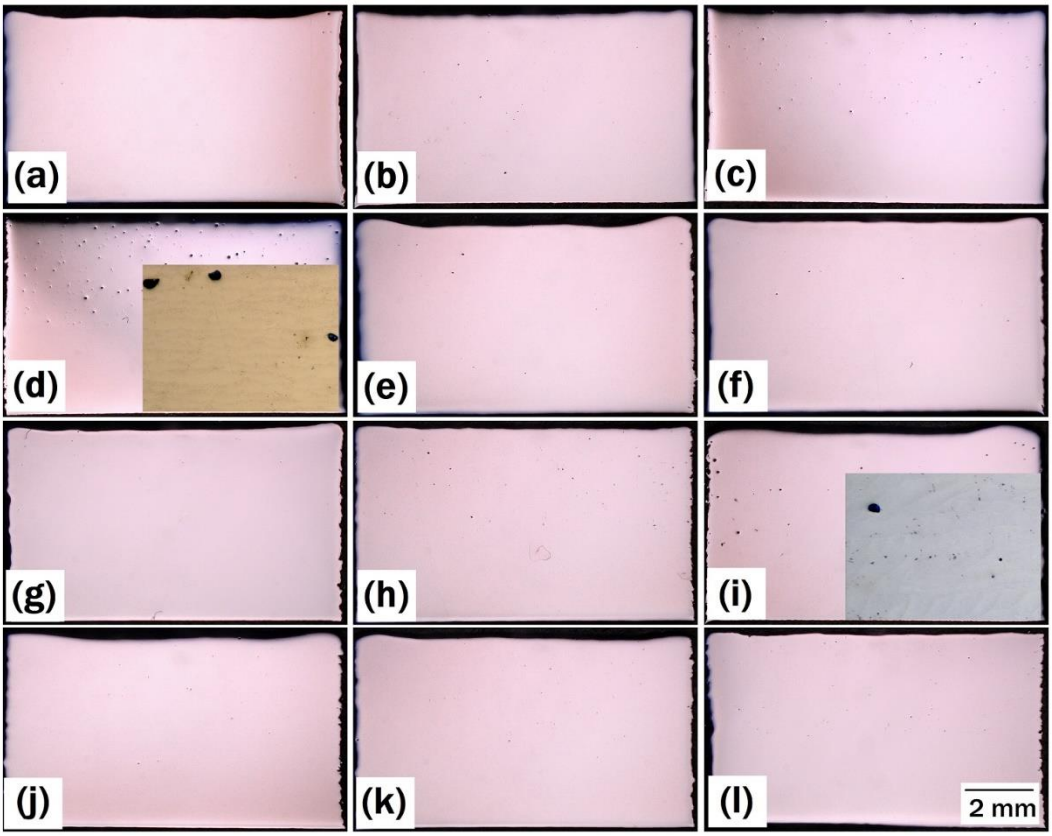

Figure 5-8 Optical micrographs of the FGM-1wt.%VC samples fabricated by the process parameters corresponding to (1-12) samples listed in Table 5-1. The insets in (d) and (i) show higher magnification images of the corresponding composite side.

According to the abovementioned results, increasing the VC content would enhance the e_v required to obtain optimum samples in terms of the densification level. To gain a better understanding of the observed trend, it is essential to consider not only the process parameters but also the powder behavior as well as powder-laser interactions during the LPBF process by implementing the modified energy density equation (Eq. 2). By substituting $t_{eff} = \frac{t}{\rho_{bed}}$ in Eq. 2 and rearranging the formula, the following relationship can be established between Eq. 1 and Eq. 2:

$$E_v = (A.\rho_{bed})e_v \quad \text{Eq. 3}$$

where ρ_{bed} is the relative powder bed packing density, which can be represented by CBD (Figure 5-5(b)) measured by FT4 test ($\rho_{bed} = CBD/\rho_{bulk}$).

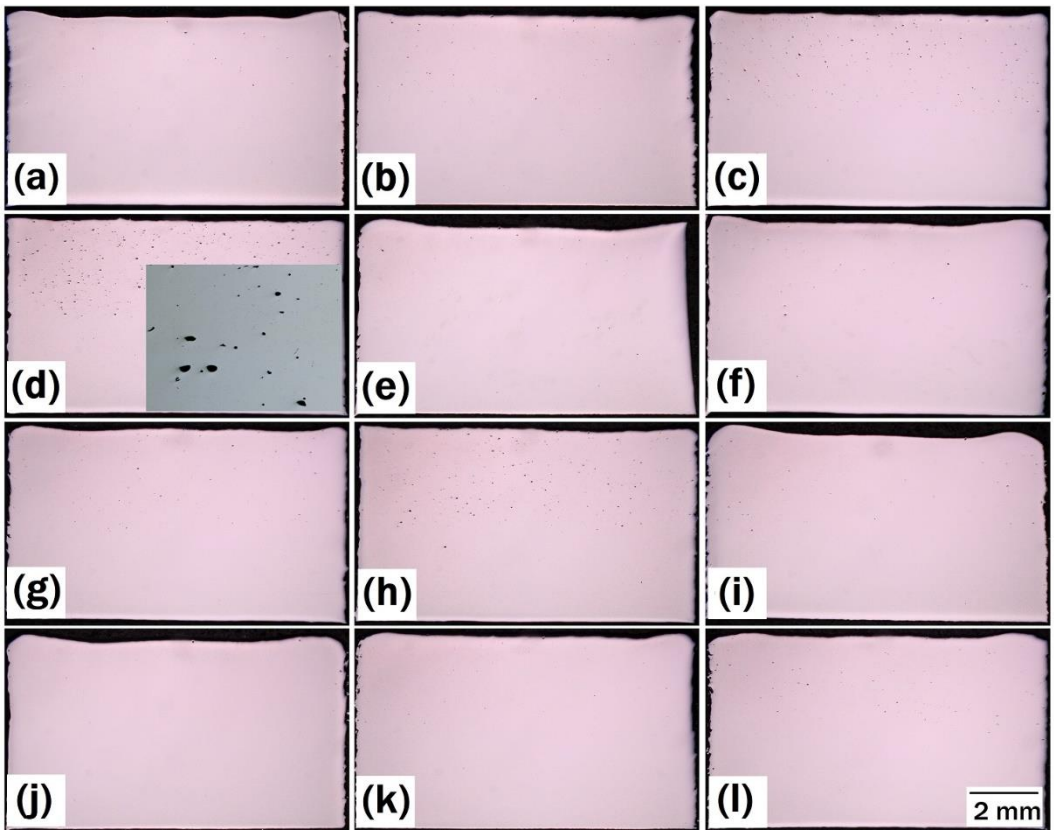

Figure 5-9 Optical micrographs of the FGM-3wt.%VC samples fabricated by the process parameters corresponding to (1-12) samples listed in Table 5-1. The insets in (d) and (i) show higher magnification images of the corresponding composite side.

Referring to Eq. 3, it can be inferred that powder systems with higher values of $A.\rho_{bed}$ are expected to require lower e_v levels to achieve optimum E_v. The calculated $A.\rho_{bed}$ values for the monolithic H13 and composite powder systems, based on the measured values provided in Figure 5-5(b) and Figure 5-6, were 0.35 and 0.39 (regardless of the VC content), respectively. Since this value is higher in the case of composite powders, lower levels of e_v were anticipated to get the optimum sample. However, the results of this study

showed the contrary. Such a discrepancy can be explained by considering the dissolution of VC particles in the composite systems during the LPBF process.

The fundamental concepts behind the dissolution of the VC powder particles below their melting temperature can be explained by considering the peak temperature experienced by the material during the LPBF process. The melt pool temperature is believed to be much higher than the liquidus temperature of H13 constituent. Nevertheless, the degree of overheating is not enough to cause melting of VC particles since their melting point (2810 °C) is almost equal to the boiling temperature of the iron (2862 °C). Therefore, the melt pool consists of the solid VC particles embedded in the molten H13 medium for a short period. Although the melt pool condition is not suitable for the VC particles to undergo melting, their dissolution may take place due to the lack of equilibrium conditions at the solid VC/liquid H13 interface. The amount of dissolution experienced by the VC particles is governed by their size as well as the applied process parameters. In other words, higher laser energy densities provide higher melt pool temperatures and a longer period that the liquid phase lasts, which both act to enhance the dissolution of the VC particles. Given the fact that the dissolution process is endothermic in nature, the presence of VC particles in the system would consume a fraction of the energy input without participating in the melting process. Hence, higher e_v levels are needed in the composite systems to melt the H13 particles and obtain highly dense samples efficiently. Due to the higher energy consumption in composite systems with higher VC content, the observed trend in Figure 5-7 is justifiable. Microstructural observations, along with the XRD analysis results provided in section 5.2.4, give evidence of such dissolution in the LPBF-processed samples.

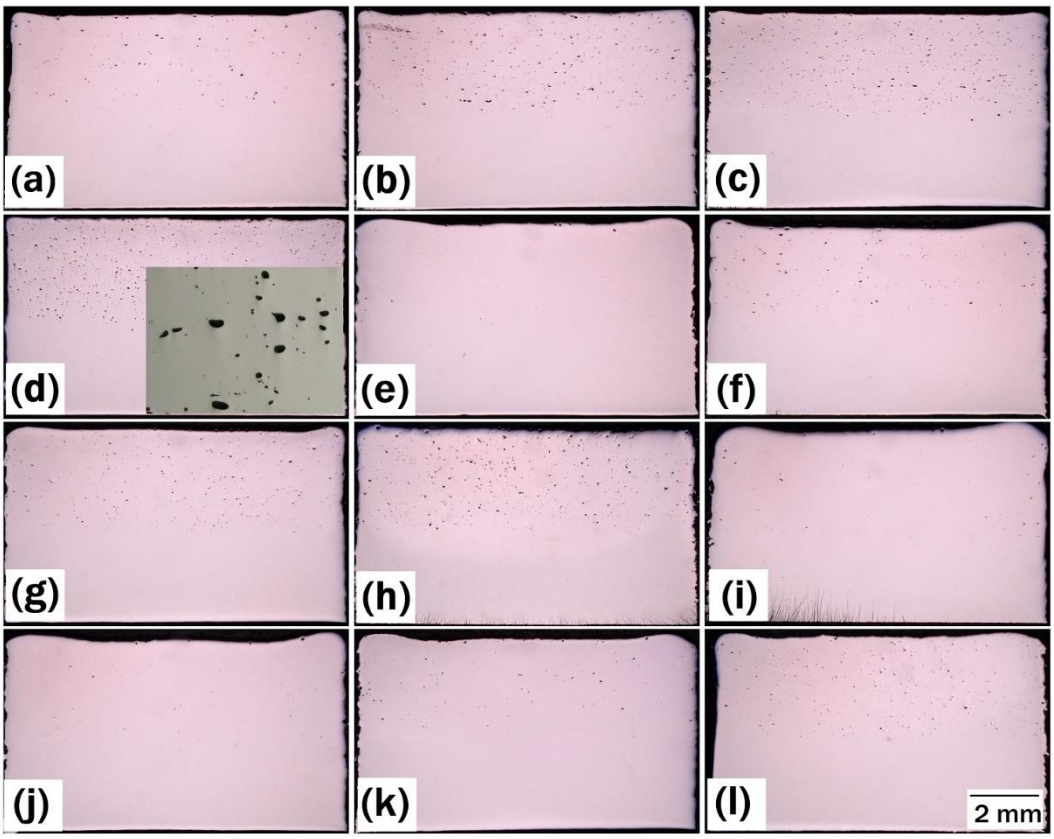

Figure 5-10 Optical micrographs of the FGM-5wt.%VC samples fabricated by the process parameters corresponding to (1-12) samples listed in Table 5-1. The insets in (d) and (i) show higher magnification images of the corresponding composite side.

5.2.3 Surface quality

Figure 5-11 shows the top surface topography of the optimum (from the densification level viewpoint) composites and monolithic H13 along with their arithmetic mean surface roughness values (S_a). Compared to the composite parts with the S_a values in the range of 6.2-7.9 µm, the monolithic H13 had a moderately higher S_a of 10.1 µm. This reveals the superior surface quality of the optimum composite samples compared to their monolithic

H13 counterpart. The obtained results are consistent with the findings of other research studies performed on the LPBF of composites. According to the literature, the addition of ceramic particles to the metallic materials up to a critical fraction can improve the surface quality. For instance, Dadbakhsh et al. [49] showed that the addition of Fe_2O_3 up to 10wt.% to aluminum could reduce the surface roughness while 15wt.% Fe_2O_3 acted to increase surface roughness. Based on another study conducted by Kang et al. [50] on LPBF processing of WC/maraging steel composites, the addition of WC up to a critical amount (10wt.%) resulted in superior surface quality compared to the monolithic maraging steel counterparts. The underlying reasons behind the improved surface quality of composites can be justified as follows:

(i) Increase in the temperature of the melt pool, which leads to lower viscosity of the melt, and consequently facilitates the free flow of the molten material to fill inter-track gaps and pores [51].

(ii) Enlargement of the melt pool caused by the enhanced absorptivity (Figure 5-6) of the composite powder compared to its monolithic system.

(iii) Enhanced thermal conductivity of the powder and consolidated composite when the reinforcing agent has higher thermal conductivity than the monolithic system [50].

In this study, the addition of VC up to 5wt.% to the H13 tool steel was found to decrease the surface roughness, meaning that the critical value beyond which the increase in VC content would reduce the surface quality in this system is higher than 5wt.%. As discussed in section 5.2.2, the optimum samples in the composites and monolithic H13 needed quite different energy densities to be achieved. Therefore, when comparing the surface quality of samples, the process parameters employed for their fabrication need to be also taken into

consideration. Higher energy densities generally lead to melt pools with higher temperatures and lower viscosities. The improved flow of the molten material under such condition is one of the major factors which promotes obtaining a track with a smoother surface and subsequently a layer with lower roughness. Besides, a higher temperature is accompanied by larger melt pool dimensions, leading to increased inter-track overlap, and consequently decreased surface roughness.

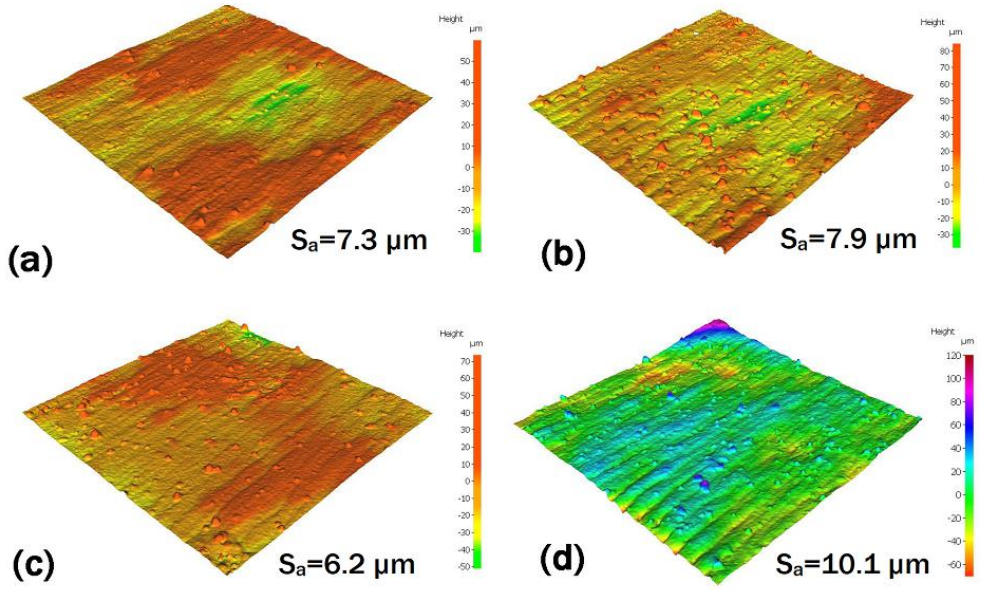

Figure 5-11 3D surface topography from the top surface of optimum samples in (a) 1wt.%VC-H13, (b) 3wt.%VC-H13, and (c) 5wt.%VC-H13 samples in the as-built condition. The image shown in (d) represents the top surface of monolithic H13 before printing composite on top of it.

5.2.4 Microstructural characterization

The XRD analysis results of the monolithic H13 as well as the 1wt.%VC-H13, 3wt.%VC-H13, and 5wt.%VC-H13 composites are provided in Figure 5-12. The semi-quantitative phase analysis results of the constituents present in the microstructures are listed in Table 5-2. All samples shared almost the same microstructure, predominantly consisted of martensite. Except for the 5wt.%VC-H13 with a relatively low percentage of retained austenite (≅5wt.%), a considerable amount of retained austenite was also detected in the microstructure of all samples (≅20wt.%). The VC contents detected by XRD in the fabricated composites were well below those of the starting composite powders. This confirms their dissolution in the liquid H13 during the heating stage and then the inability of the dissolved particles to fully precipitate in the cooling stage as a result of high cooling rates associated with the process. The enrichment of the matrix with V and C elements influences the martensite start (M_s) and finish (M_f) temperatures. While C decreases both M_s and M_f [52], the contrary is the case for V [53]. Up to 3wt.%VC, these two competing effects seem to cancel out each other, leading to almost the same retained austenite content. When it comes to the 5wt.%VC-H13 system, the dominancy of the effect of V seems to be prevailing. However, the exact reason behind this sharp decrease in the fraction of the retained austenite requires further investigation.

Phase analysis results also confirmed the presence of VC in the 3wt.%VC-H13 and 5wt.%VC-H13 composites (Figure 5-12 and Table 5-2). However, this phase was absent in the case of monolithic H13 and 1wt.%VC-H13 systems. Although fast cooling rates during the LPBF process hinder precipitation of VC in the matrix in all cases, thermal effects of upcoming layers on the previously consolidated layers can encourage the precipitation of VC depending on the level of supersaturation. For instance, the level of

supersaturation for 1wt.%VC-H13 was not high enough to trigger the precipitation of VC upon exposure to thermal cycling. That is why negligible amounts of VC could be observed in its final microstructure which would not be detected by XRD due to limitations with the size and weight fraction resolution of this method. However, the precipitation was more pronounced in 3wt.%VC-H13 and 5wt.%VC-H13 composites due to the higher levels of (V+C) supersaturation. It should be borne in mind that limited precipitation of VC phase occurs because of thermal cycling, meaning that considerable levels of (V+C) supersaturation are still present in the matrix of all composites.

Table 5-2 Semi-quantitative phase analysis of the constituent phases in the microstructure of the monolithic H13 and composites

Sample	Weight percentage (wt.%)-Measured			Volume percentage (vol.%)-Calculated
	Martensite	Retained austenite	VC	VC
H13	80.23	19.76	-	-
1%VC-H13	75.02	24.98	-	-
3%VC-H13	77.82	20.64	1.54	2.07
5%VC-H13	93.03	4.69	2.28	3.06

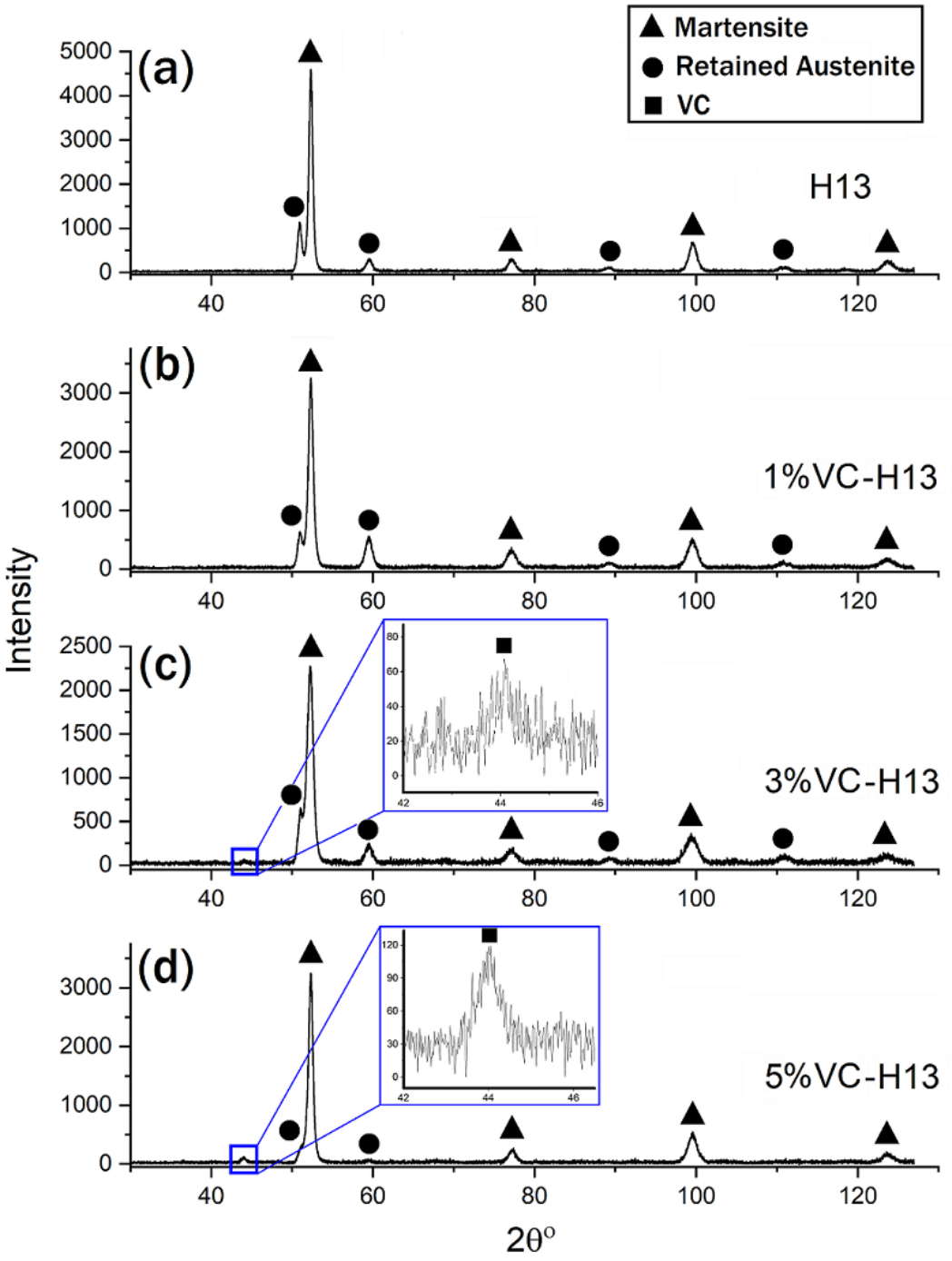

Figure 5-12 XRD patterns of: (a) monolithic H13, (b) 1wt.%VC-H13, (c) 3wt.%VC-H13, and (d) 5wt.%VC-H13 samples in the as-built condition. The insets in (c) and (d) are the magnified views of the selected squares.

5.2.4.1 Microstructure of the H13 side of FGMs

Figure 5-13(a) shows the overview of the microstructure for the monolithic H13 side of the FGMs. Based on the micrograph at higher magnification provided in Figure 5-13(b), a cellular microstructure is perceptible in which the core of the cells and the cell boundaries are composed of martensite and austenite phases, respectively [54]. The band contrast along with the inverse pole figures (IPFs) of the martensite phase in X, Y, and Z directions are shown in Figure 5-13(c-f) to characterize the morphology of the martensite phase. The prior austenite grains with almost equiaxed morphology are designated with a dotted line in Figure 5-13(f). Figure 5-13(d-f) confirms the presence of lath-type martensite in the microstructure of the monolithic H13. According to the literature, depending on the carbon content, lath-type (<0.6wt.% C), plate-type (>1wt.% C) or a mix of them (0.6<wt.% C<1) is expected to be found in the microstructure [55]. Since the carbon content in the monolithic H13 is about 0.4wt.%, this observation is justifiable.

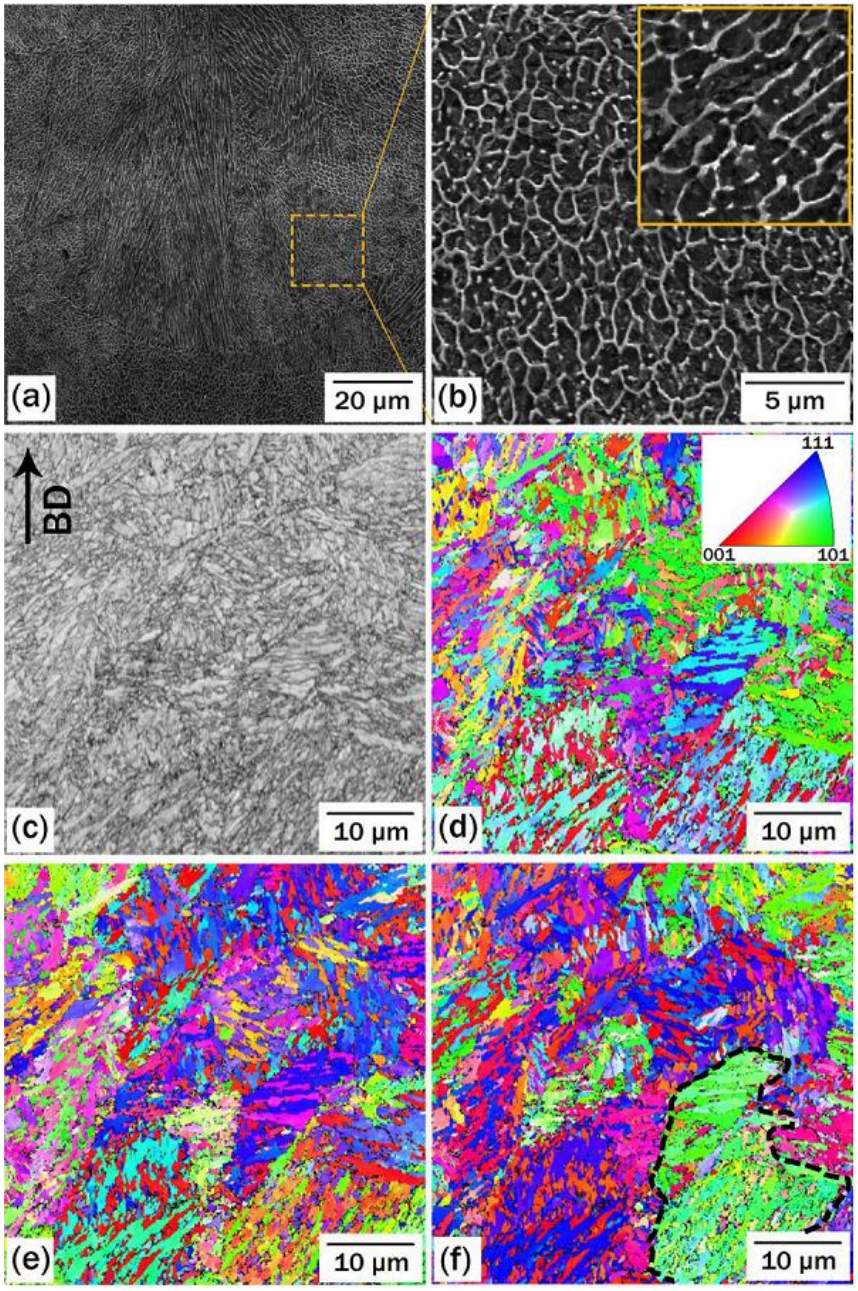

Figure 5-13 SEM micrographs of monolithic H13: (a) overview, and (b) high-magnification image of the dashed square shown in (a). EBSD micrographs: (c) band contrast, (d) IPFX, (e) IPFY, and (f) IPFZ. “BD” refers to the building direction

5.2.4.2 Microstructure of the composite side of FGMs

The SEM and EBSD micrographs of the 1wt.%VC-H13, 3wt.%VC-H13, and 5wt.%VC-H13 composites are shown in Figure 5-14, Figure 5-15, and Figure 5-16, respectively. Referring to Figure 5-14(a,b), the microstructure is fully cellular, meaning that the addition of 1wt.%VC to the monolithic H13 did not change the solidification mode. The microstructure of 3wt.%VC-H13 can still be characterized as cellular (Figure 5-15(a,b)), the only difference being that the cell boundaries show some degrees of discontinuity. When it comes to 5wt.%VC-H13, only a small region at the melt pool boundaries features a cellular microstructure (Figure 5-16(a,b)), while columnar dendritic solidification mode is dominant within the rest of the melt pool.

Based on the IPFs provided in Figure 5-14(d-f), the microstructure features lath-type martensite similar to that of the monolithic H13. Referring to the XRD analysis results of the 1wt.%VC-H13 system presented in Figure 5-12(b), the final microstructure was free from VC precipitates, confirming the presence of dissolved V and C elements as supersaturated solid solution in the matrix. The C content of 0.58wt.% was calculated in the 1wt.%VC-H13 system, which falls within the lath-type martensite region. By excluding the portion of C existing in the precipitated VC in 3wt.%VC-H13 and 5wt.%VC-H13 systems, the total amount of C present in the form of the supersaturated solid solution was calculated to be 0.67 and 0.91wt.%, respectively, which both lie within the mixed (lath+plate)-type martensite region. The IPFs presented in Figure 5-15, and Figure 5-16 confirm the presence of both martensite types in the final microstructure. It is worth mentioning that the change in the type of martensite caused by the increase in the incorporated VC validates the existence of a major portion of C (originating from VC dissolution) as a supersaturated solid solution in the matrix.

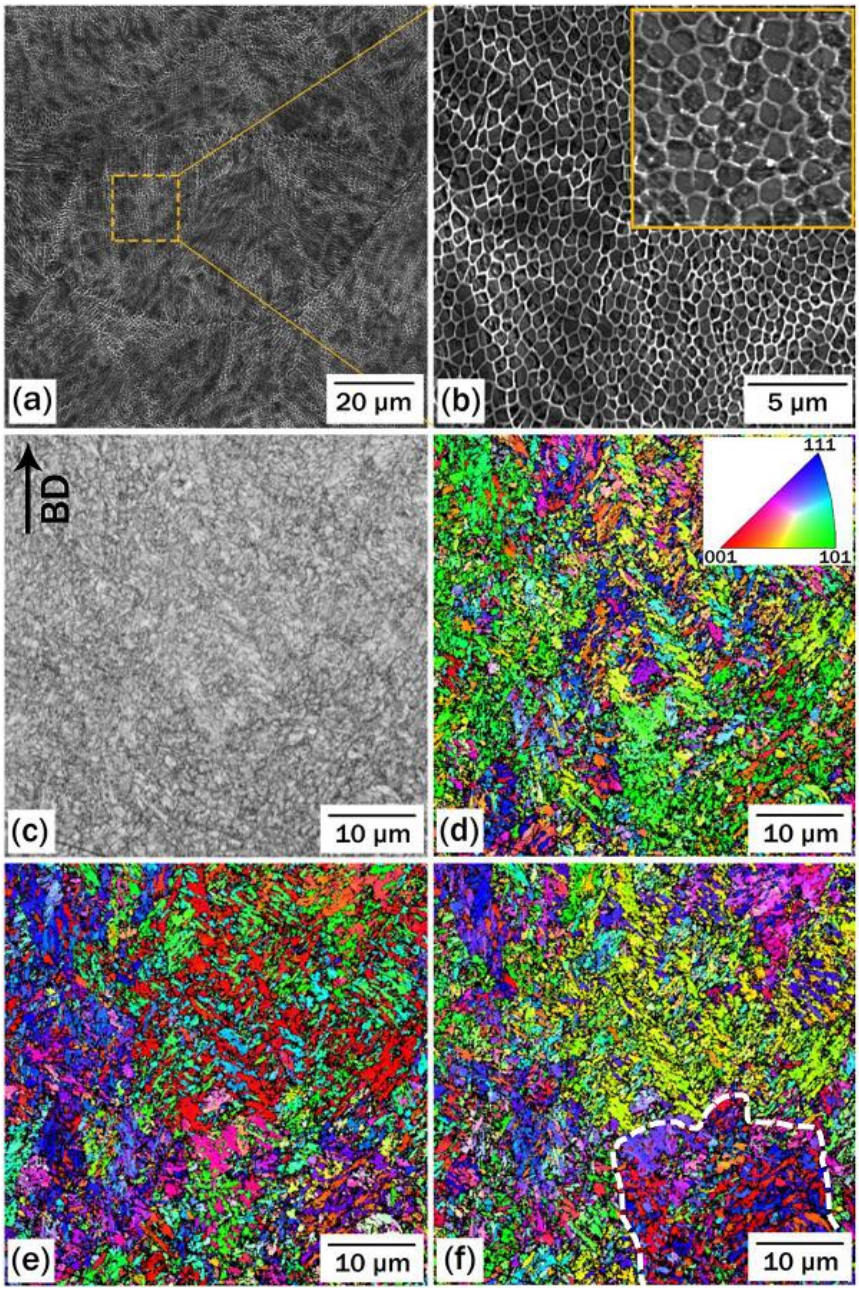

Figure 5-14 SEM micrographs of 1wt.%VC-H13: (a) overview, and (b) high-magnification image of the dashed square shown in (a). EBSD micrographs: (c) band contrast, (d) IPFX, (e) IPFY, and (f) IPFZ. “BD” refers to the building direction.

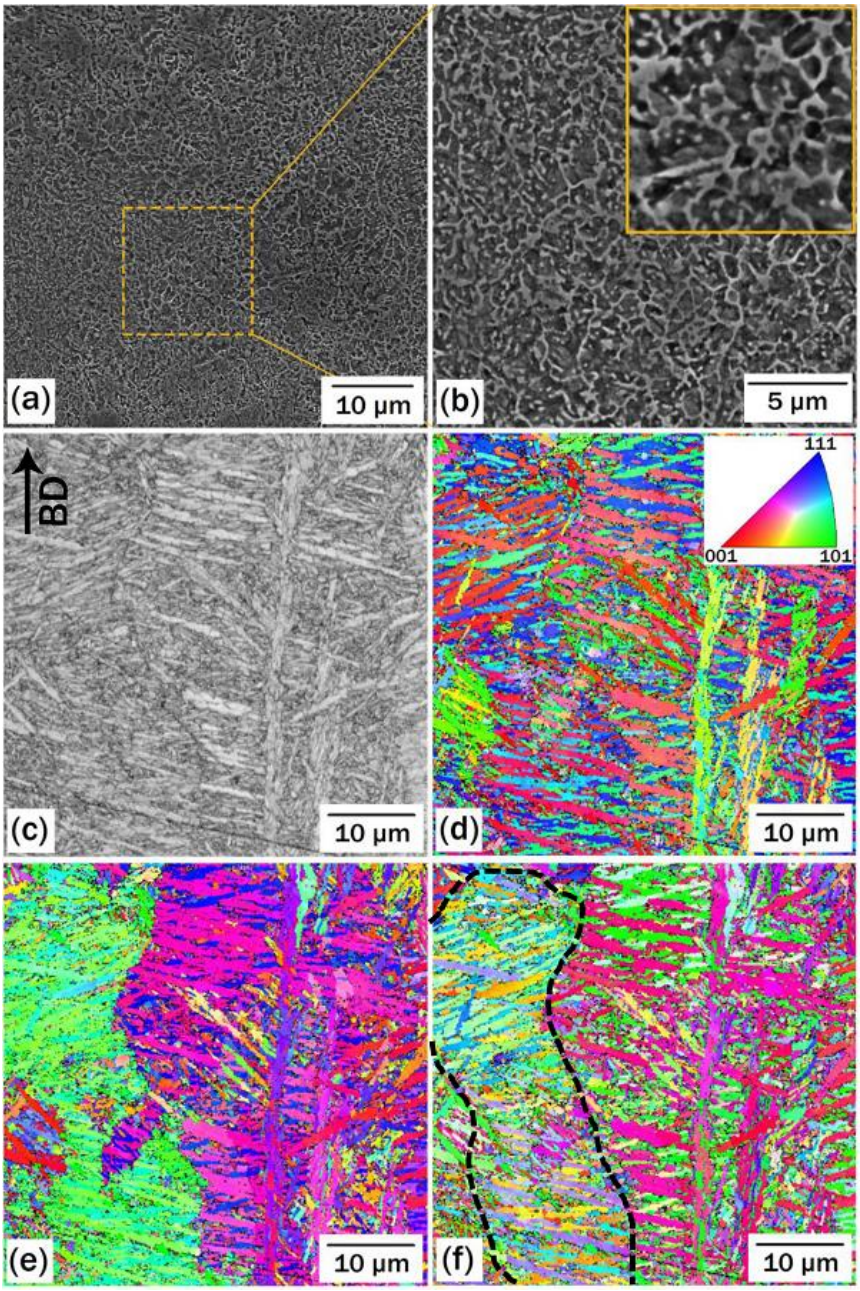

Figure 5-15 SEM micrographs of 3wt.%VC-H13: (a) overview, and (b) high-magnification image of the dashed square shown in (a). EBSD micrographs: (c) band contrast, (d) IPFX, (e) IPFY, and (f) IPFZ. “BD” refers to the building direction**.**

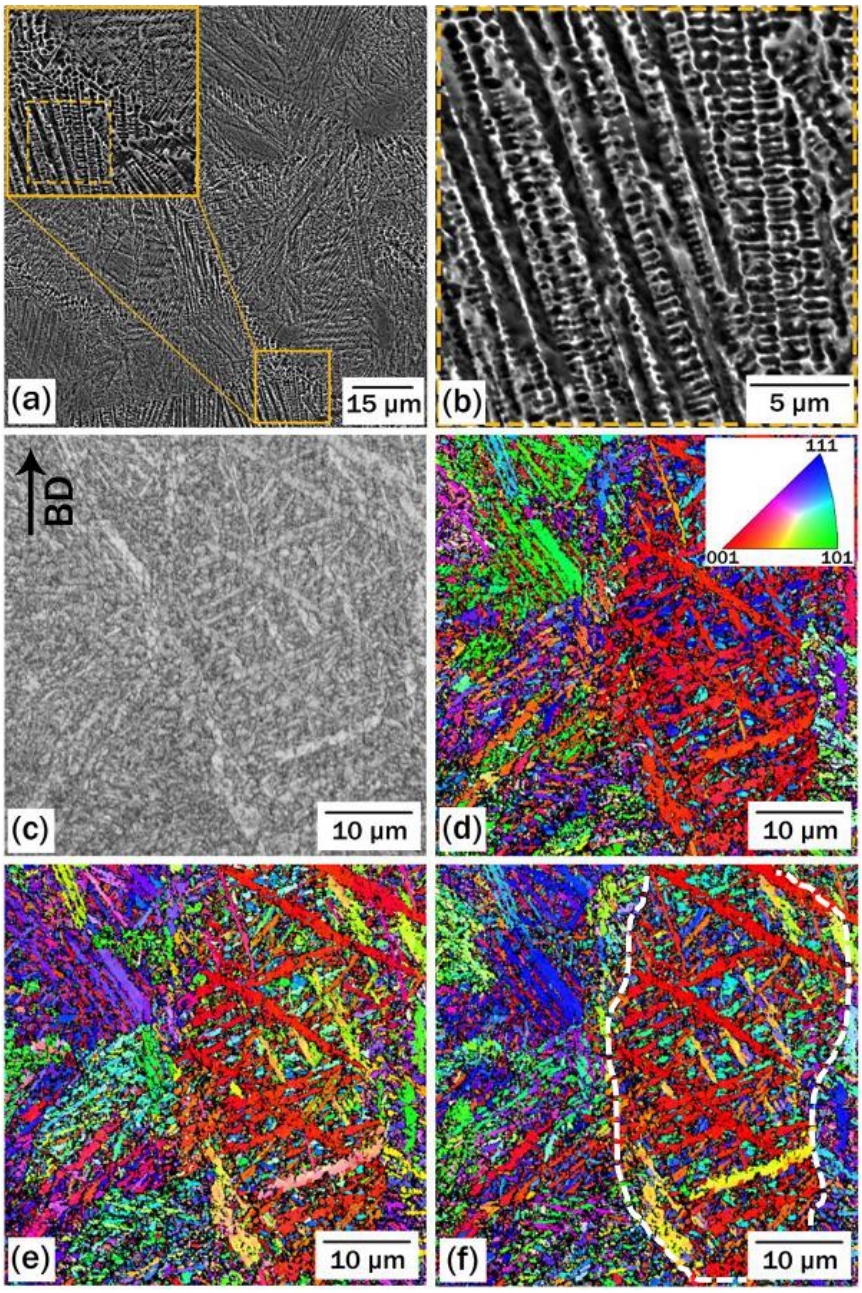

Figure 5-16 SEM micrographs of 1wt.%VC-H13: (a) overview, and (b) high-magnification image of the dashed square shown in (a). EBSD micrographs: (c) band contrast, (d) IPFX, (e) IPFY, and (f) IPFZ. “BD” refers to the building direction.

5.2.4.3 Characterization of the interface in FGMs

According to Figure 5-8, Figure 5-9, and Figure 5-10, no sign of cracking or delamination was observed at the interface, proving that the interface between the monolithic H13 and composites is sound. The porosities in the composite side might also be present at the interface. These porosities are associated with the process parameters and do not originate from incompatibility between the two materials.

EDS line-scan analysis results revealed that there is a transition zone (TZ) at the interface of the monolithic H13 and composites. In this zone, the composite powder deposited during the LPBF process is diluted by the existing unprocessed H13 powder, which causes the deviation of the VC content from the nominal value of the composite powder system. Such deviation would fade away as the build progresses until it reaches the VC-H13 composite zone. Figure 5-17 shows the variation in the V and Cr elements along the build direction in a length of 3 mm covering the TZ. As it is evident, the intensity of Cr is almost constant along the scanned line. However, the V content undergoes a sharp drop in TZ. The thickness of the TZ in all FGMs is about 0.4 mm corresponding to 10 powder layers.

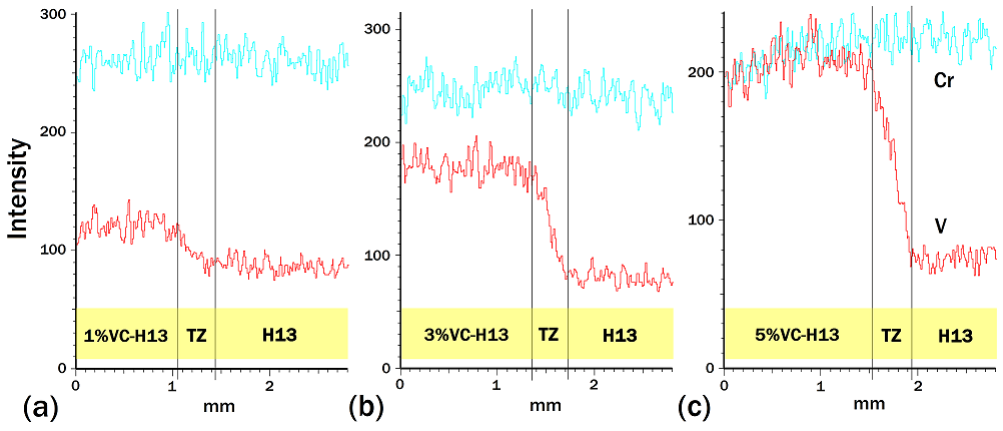

Figure 5-17 Line-scan EDS analysis results of vanadium (V) and chromium (Cr) elements in: (a) FGM-1wt%VC, (b) FGM-3wt%VC, and (c) FGM-5%wtVC.

5.2.5 Mechanical properties

5.2.5.1 Microhardness

The variation in the microhardness along the build direction (Z-axis) of the FGMs is provided in Figure 5-18. Three distinct zones of monolithic H13, TZ, and VC-H13 composite can be distinguished based on the observed trend. As it is evident, the microhardness in the H13 zone maintains the average of 600 HV, whereas, in the TZ, such a value undergoes a sharp change due to the VC content variation from zero up to its nominal value in each composite system. The level of jump in the microhardness of this zone was 76, 165, and 229 HV for FGMs containing 1, 3, and 5wt.%VC, respectively. The microhardness profile in each FGM approaches an almost constant value in the VC-H13 zone. The average microhardness values corresponding to the composite zone of FGMs with 1, 3, and 5wt.%VC were 700, 785, and 840 HV, respectively which are 17, 31, and 40% higher than that of the monolithic H13.

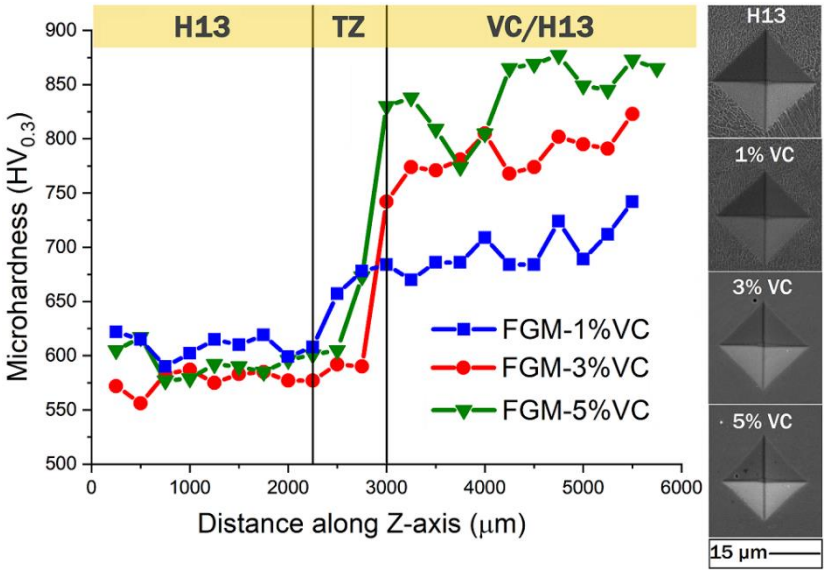

Figure 5-18 The microhardness profile along the Z-axis (build direction) for FGMs containing 1, 3, and 5wt.% VC.

5.2.5.2 Nanohardness

Nanoindentation test was also performed to investigate the nano-mechanical properties of the LPBF-processed FGMs. Figure 5-19(a) shows representative nanoindentation load-displacement curves of monolithic H13 as well as composite sides of different FGMs. The maximum penetration depth decreased from 536 nm to 515, 489, and 470 nm when 1, 3, and 5wt.%VC are added to the monolithic H13. The lower penetration depth in the composite side of FGMs clearly confirms their higher hardness compared to the H13 side. The average nanohardness values obtained by several measurements in each side are presented in Figure 5-19(b). The same trend as the microhardness is perceptible in the nanohardness measurement results, the only difference being that the nanohardness values were moderately greater than the corresponding microhardness values due to the well-known indentation size effect [56, 57].

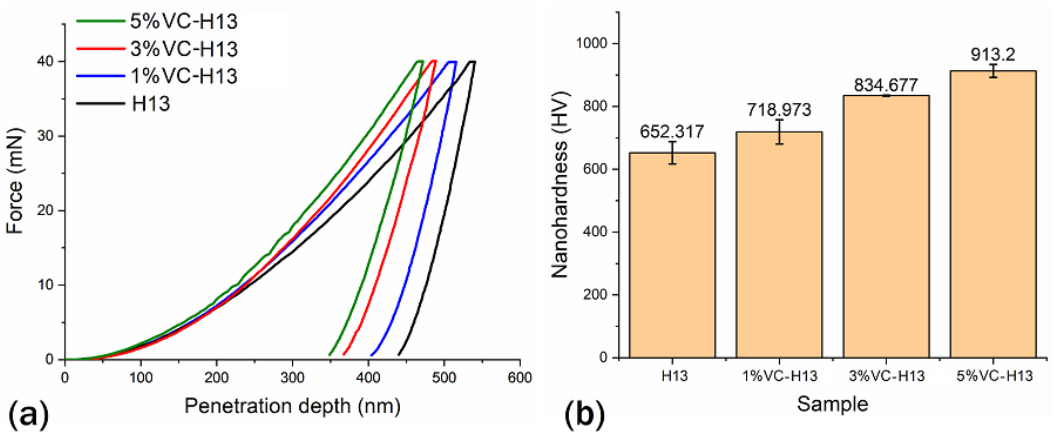

Figure 5-19 (a) Representative nanoindentation load-displacement curves, and (b) average nanohardness of monolithic H13 and 1wt%VC-H13, 3wt%VC-H13, and 5wt%VC-H13 composites.

5.2.5.3 Hardening mechanism

As discussed before, the starting VC reinforcing agent experiences dissolution (rather than melting) during the heating stage of the LPBF process. Due to the rapid solidification as well as the thermal cycling induced by the layer-wise nature of the process, only a fraction of the dissolved VC particles can find the chance to precipitate during the cooling stage, as revealed by XRD analysis results (Figure 5-12 and Table 5-2). Therefore, the final microstructure of composites is composed of a (V+C)-supersaturated solid solution martensitic matrix along with small amounts of VC precipitates dispersed in it. Although the literature suggests the significant contribution of carbide forming elements (i.e., V, Cr, and Mo) on the hardness improvement of tool steels through carbide formation, the results obtained in this study demonstrated otherwise. To clarify, despite the negligible content of VC reinforcement in the matrix of the fabricated composites (≅0, 1.54, 2.28wt.%), the hardness increased up to 250 HV based on the microhardness and nanohardness measurement results. This clearly gives evidence of other factors playing a major role in hardening of LPBF-processed VC-H13 composites. In the following, the contribution of load-bearing (caused by the presence of reinforcement), non-equilibrium phase transformation, and (V+C)-supersaturation hardening mechanisms are thoroughly elucidated for the developed composites containing 1, 3, and 5wt.%VC.

Load-bearing mechanism: Incorporation of harder reinforcement into the softer matrix generally leads to the improvement in hardness based on the rule of mixture [58-60]:

$$H_{MMC} = V_r H_r + V_m H_m \quad \text{Eq. 4}$$

where H_{MMC}, H_r, and H_m represent the hardness of the composite, reinforcement and matrix, respectively. V_m and V_r signify the volume fraction of matrix and reinforcement, respectively in which V_r is defined as (1-V_m).

The term ($V_r H_r$) in Eq. 4 represents the hardness improvement through the load-bearing mechanism. Therefore:

$$\Delta H_{Load-bearing} = V_r H_r \quad \text{Eq. 5}$$

In order to analyze the hardening potential of VC reinforcement, the monolithic H13, as well as the developed composites, were subjected to the standard austenitizing heat treatment at 1050°C/30 min followed by furnace cooling down to the ambient temperature. This thermal cycle allows the supersaturated V, and C elements to fully precipitate in the matrix (Figure 5-21(b,c)). In addition, the martensite in the as-build condition transforms to ferrite as a result of the furnace cooling. Therefore, the experienced phase transformations during the heat treatment cycle can be summarized as follows:

$M \rightarrow \gamma \rightarrow \alpha + carbides$

According to the XRD measurement results in Figure 5-20, the dominant carbides in the heat-treated samples were VC, while scant amounts of chromium carbides (e.g., Cr_3C_2, $Cr_{23}C_6$, Cr_7C_3) were also present. The semi-quantitative analysis results, including the weight percentage of ferrite and VC phases, are listed in Table 5-3. As can be seen, the monolithic H13 contains 1.12wt.% VC in equilibrium condition. Addition of 1, 3, and 5wt.%VC to H13 has increased the VC content of HT samples by 1.62, 2.8, and 4.22wt.%, respectively. Figure 5-21(a) shows the microhardness measurement results on the heat-treated FGMs. The difference between the microhardness of the monolithic H13 and composite sides is merely attributable to the presence of a higher fraction of VC in the latter. The average microhardness of H13 increased from 206 HV to 216, 221, and 230 HV for 1, 3, and 5wt.% VC composites, respectively. This clearly shows the insignificant contribution of VC to hardening behavior. Figure 5-22 shows the level of improvement in hardness caused by higher volume fraction of VC in composites compared to the

monolithic H13 in the heat-treated condition. The hardness improvement predicted based on the rule of the mixture is also incorporated in this figure. It is self-evident that the predicted values considerably overestimate the improvement in hardness due to the presence of VC.

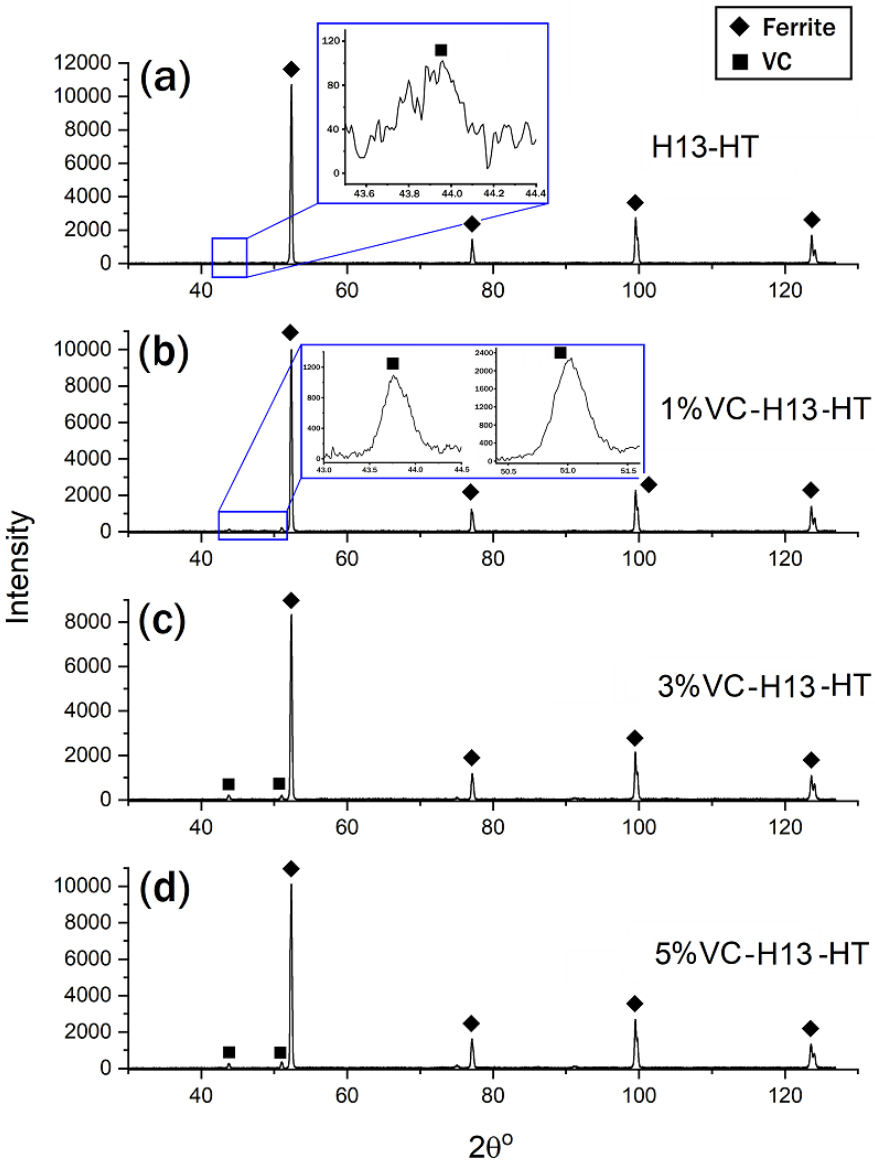

Figure 5-20 XRD patterns of heat-treated: (a) monolithic H13, (b) 1wt.%VC-H13, (c) 3wt.%VC-H13, and (d) 5wt.%VC-H13 samples. The insets in (a) and (b) are the magnified views of the selected squares.

Table 5-3 The weight/volume percentage of ferrite and VC phases in the heat-treated monolithic H13 and composites containing 1, 3, and 5wt.% VC.

Sample	Weight percentage (wt.%)-Measured		Volume percentage (Vol.%)-Calculated	
	Ferrite	VC	Ferrite	VC
H13-HT	98.88±0.133	1.12±0.133	98.49	1.51
1%VC-H13-HT	97.16±0.151	2.74±0.151	96.33	3.67
3%VC-H13-HT	96.08±0.168	3.92±0.168	94.77	5.23
5%VC-H13-HT	94.66±0.188	5.34±0.188	92.92	7.08

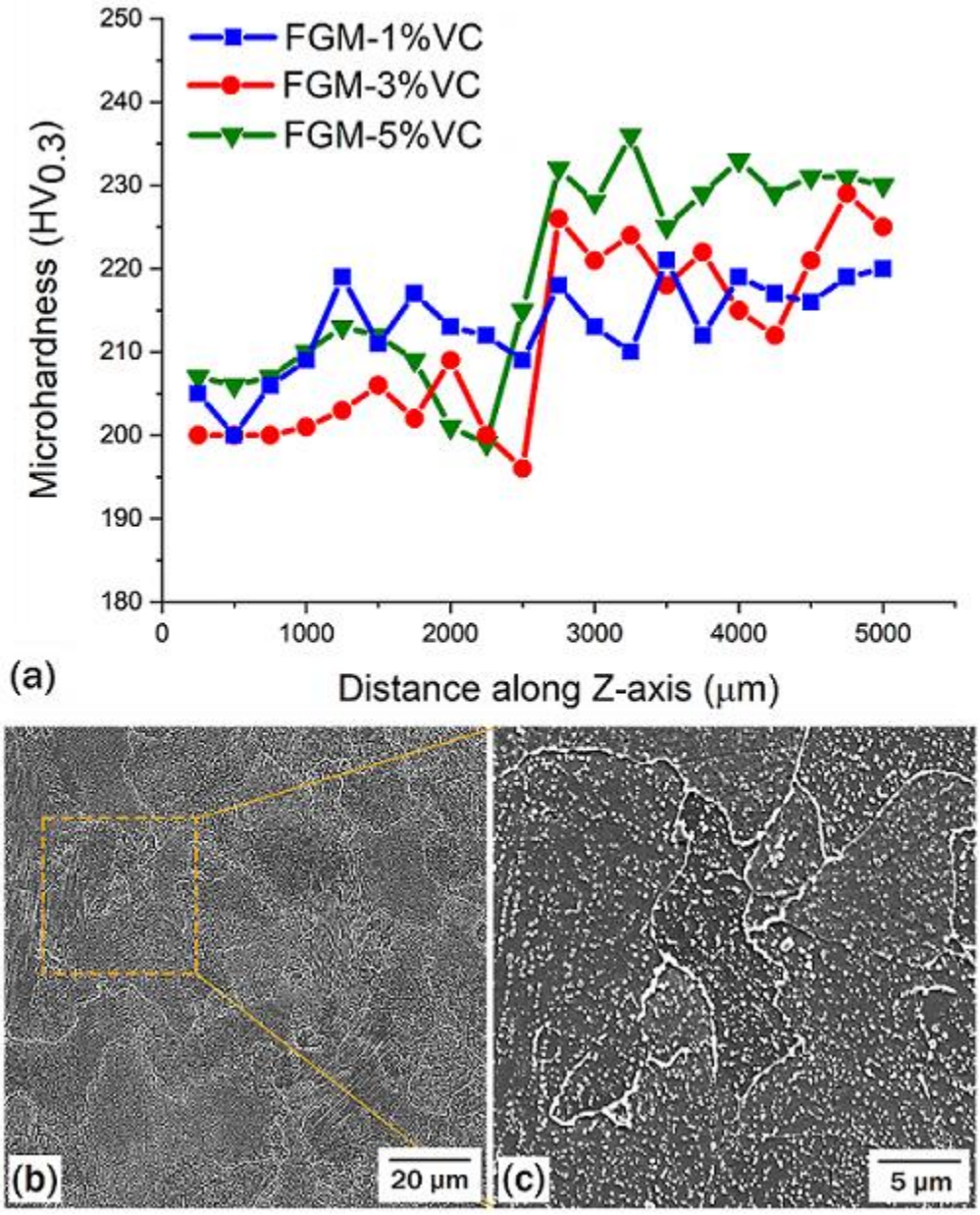

Figure 5-21 The microhardness profile along the Z-axis (build direction) for heat-treated FGMs containing 1, 3, and 5wt.%VC.

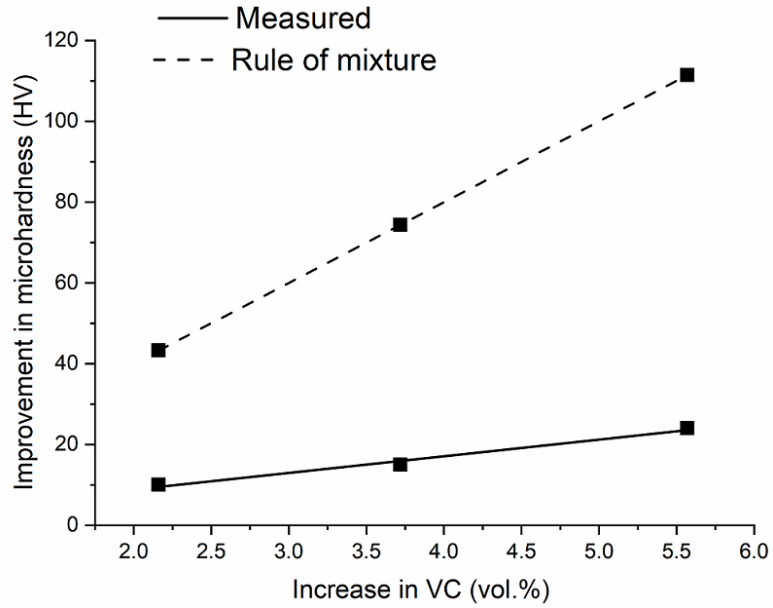

Figure 5-22 The improvement in microhardness of fabricated composites as a function of the increase in VC content over that of the monolithic H13.

The reference line obtained to determine the contribution of VC reinforcement on the hardness improvement (solid line in Figure 5-22) can be utilized to calculate the role of load-bearing mechanism in the as-built composites. Referring to Table 5-2, the VC phase is absent in 1wt.%VC-H13 composite; therefore, the hardening does not occur through the load-bearing mechanism for this sample. In composites containing 3, and 5wt.%VC, the increase in the volume fraction of VC compared to the monolithic H13 in the as-build condition was 2.07 and 3.06%, corresponding to less than 10 HV improvement in microhardness (Figure 5-22).

(V+C)-Supersaturation: The solid solution hardening is related to the interaction between the mobile dislocations and the solute atoms. While several theories have been suggested for explaining solid solution strengthening, the most relevant mechanisms are the elastic interactions due to: (*i*) the size misfit, in which the difference between the size of solute and matrix atoms induces a strain field, and (*ii*) the modulus misfit, where the difference

in shear modulus of the solute and matrix atoms creates a hard or soft "spot" in the matrix [61-63]. The formed local strain fields interact with dislocations and impede their motion, resulting in the enhanced hardness [64, 65]. Compared to conventional manufacturing processes with equilibrium condition, the non-equilibrium nature of LPBF process caused by its extremely fast cooling rates can noticeably extend the solid solubility limit of alloying elements in the matrix and lead to intensified solid solution hardening [66, 67]. In comparison to the substitutional alloying elements, the larger size misfit ($|(r_{matrix} - r_{solute})/r_{matrix}|$, where r represents the atomic radius) provided by interstitial alloying elements (i.e., carbon) can generate significantly stronger obstacles for the movement of dislocations, leading to higher levels of solid solution strengthening [68]. Referring to the XRD results in Table 5-2, the VC contents in the composites were noticeably lower than the contents added to the starting H13 monolithic powder, proving the entrapment of V and C elements in the matrix caused by the fast cooling rates during the LPBF process. Since the limited VC phase precipitated during the process in the 3wt.%VC-H13, and 5wt.%VC-H13 composites showed to have a negligible influence on the hardness improvement (Figure 5-22), the significantly higher microhardness in these cases (Figure 5-18) is mainly attributable to the presence of (V+C) in the form of supersaturated solid solution. Figure 5-23 shows the hardness improvement as a function of the atomic fraction of (V+C) in the form of supersaturated solid-solution in the matrix. The supersaturation level was calculated from the difference between the VC content added to the monolithic H13 powder and the VC content in the composite parts after LPBF processing obtained by XRD (Table 5-2). As shown in Figure 5-23, a linear correlation can be established between the hardness improvement and the level of (V+C) supersaturation (at.%) within the range of VC contents investigated in this study.

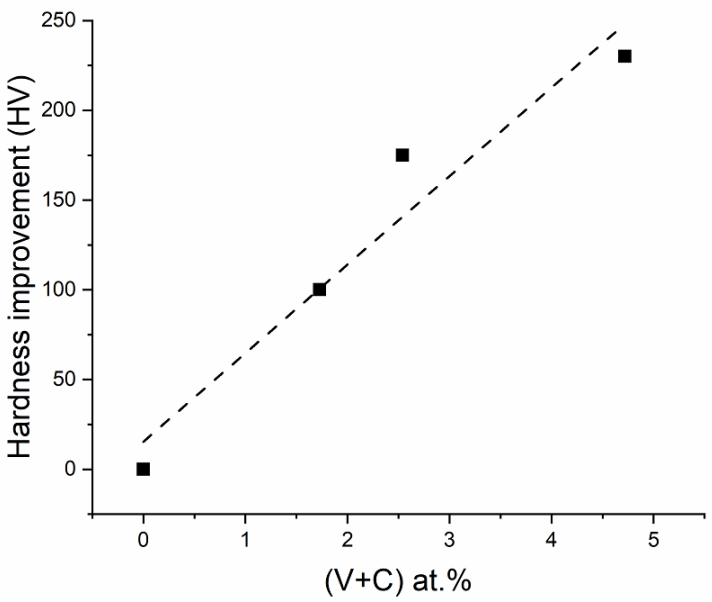

Figure 5-23 The improvement in microhardness of fabricated composites as a function of the increase in the level of (V+C) supersaturation over that of the monolithic H13.

It should be noted that the fraction of retained austenite is almost the same as that of the monolithic H13 for 1wt.%VC-H13 and 3wt.%VC-H13 composites. Therefore, the whole hardness improvement can be attributed to the supersaturation of V and C elements. However, in the case of 5wt.%VC-H13, the fraction of retained austenite was noticeably lower than other cases, which also can act to increase the hardness. In other words, the hardness improvement reported in Figure 5-23 for this sample is overestimating the impact of (V+C) supersaturation solid solution mechanism. On the other hand, as microstructural characterizations revealed in Figure 5-14, Figure 5-15, and Figure 5-16 incorporation of VC to H13 did not significantly affect the primary austenite grain size, meaning that the hardness improvement through the Hall-Petch hardening mechanism is negligible for the VC-H13 systems.

5.2.5.4 Wear resistance

In order to investigate the wear resistance of the fabricated FGMs, ball-on-disk wear test was performed in three different radii of 4, 6, and 8 mm for every single case to ensure consistency and repeatability. The coefficient of friction (COF) as a function of the sliding distance is shown in Figure 5-24(a-c). The mean values of COF in each composite, as well as the monolithic H13, is provided in Table 5-4. Regardless of the VC content, the mean value of COF for all composites was almost the same as that of the monolithic H13. Therefore, the addition of VC up to 5wt.% to H13 tool steel does not seem to influence the magnitude of COF in LPBF-processed parts. Figure 5-24(d) represents the typical measured depth profile of the worn tracks. The width and depth of the tracks were obtained and used to calculate the wear rates listed in Table 5-4. The results revealed that the incorporation of VC progressively improves the wear resistance of H13 up to 53% corresponding to the 5wt.%VC-H13 composite.

The same discussion provided in Section 5.2.5.3 for the higher hardness of composites compared to the monolithic H13 is also valid for their higher wear resistance. Figure 5-25(a) shows the COF versus sliding distance for 1wt.%VC-H13-HT at three different radii of 4, 6, and 8 mm. By comparing the depth and width of the worn track in the as-build (Figure 5-24(d)) and heat-treated (Figure 5-25(b)) 1wt.%VC-H13, it can be concluded that the wear resistance significantly dropped in the heat-treated case. The wear rate in the heat-treated sample was determined to be 76.7×10-5 mm^3/N.m, which is an order of magnitude higher than the corresponding composite in the as-built condition. This clearly reveals that the VC particles (also other carbides) precipitated in the ferritic matrix yield a noticeably inferior wear resistance compared to that of the (V+C)-supersaturated martensitic matrix.

It is worth noting that the mean COF after heat-treatment (0.66) is comparable to that of the composite in the as-built condition.

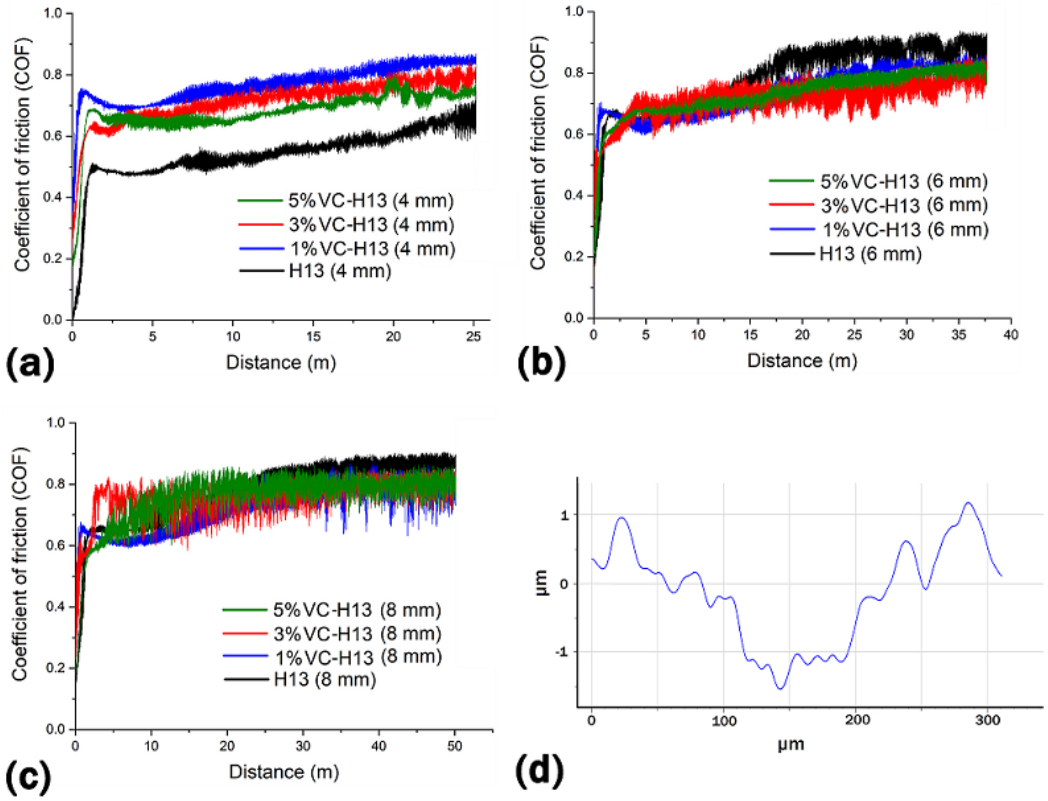

Figure 5-24 Coefficient of friction (COF) versus sliding distance in the radius of (a) 4 mm, (b) 6 mm, and (c) 8 mm. The depth profile for a typical worn track is shown in (d).

Table 5-4 The coefficient of friction (COF) and wear rate of monolithic H13 and composites containing 1, 3, and 5wt.% VC.

Sample	Coefficient of friction (μ)		Wear rate [mm^3/N.m]×10^{-5}	
	Mean	Standard deviation	Mean	Standard deviation
H13	0.70	0.116	2.575	0.505
1%VC-H13	0.74	0.091	2.057	0.188
3%VC-H13	0.73	0.092	1.513	0.469
5%VC-H13	0.72	0.090	1.214	0.21

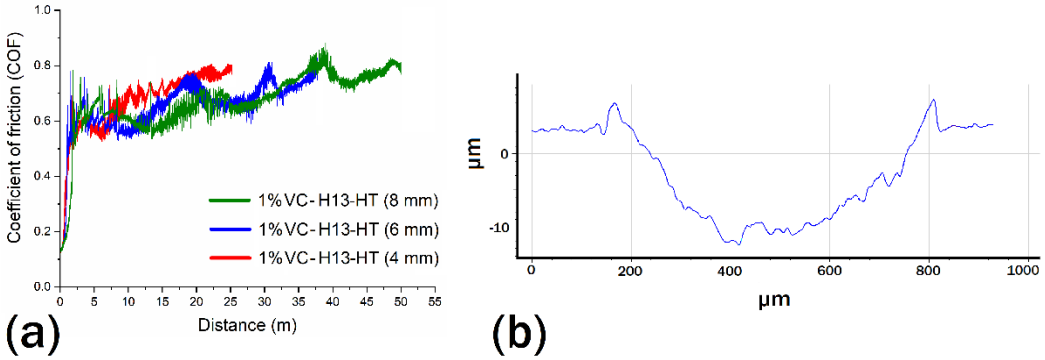

Figure 5-25 (a) Coefficient of friction (COF) versus sliding distance in three different radii of 4, 6, and 8 mm, and (b) the depth profile for the worn track of for the heat-treated 1wt.%VC-H13 composite.

5.3 Conclusions

In this study, functionally graded bi-materials having monolithic H13 at the bottom and VC-H13 composites on top were fabricated via the LPBF process to assess the possibility of improving the wear resistance of H13 tool steel. The following summarizes the main outcomes:

1- Ideal composite powders (containing 1, 3, and 5wt.%VC) with almost spherical H13 particles fully decorated by VC were successfully prepared by 1 h of ball milling. Although decreasing the powder flowability (18-60% increase in the specific energy) and conditioned bulk density (5-17%), the increase in the VC content led to the enhanced optical absorption (15-30%) of the developed composite powders compared to the monolithic H13 powder.

2- 1wt.%VC-H13 and 3wt.%VC-H13 were found to be highly processable since almost defect-free parts (>99.5% relative density) were achievable in a wide range

of energy densities. However, the addition of 5wt.%VC significantly degraded the processability by narrowing down the energy density range leading to highly dense parts. As the VC content increased, higher energy density levels were required to obtain samples with the highest density. This was attributed to the endothermic nature of the VC dissolution during the LPBF processing of composites which consumes a fraction of the heat input subjected to the system.

3- In addition to their high density, the fabricated composites benefitted from surface quality superior to that of the monolithic H13 counterpart (S_a of 6.2-7.9 µm for composites versus 10.1 µm for H13).

4- The dominant phase in the microstructure of all samples was martensite. Except for the 5wt.%VC-H13 system, a considerable amount of retained austenite was also detected in all samples by the XRD analysis. The martensite type in 3wt.%VC-H13 and 5wt.%VC-H13 changed to a mix of lath and plate compared to the lath-type martensite in the monolithic H13 and 1wt.%VC-H13 cases. This confirms the presence of C originating from dissolved VC particles in the form of a supersaturated solid solution.

5- The hardening mechanism governing the improved microhardness, nanohardness, and wear resistance was attributable to V and C elements as supersaturated solid solutions in the matrix rather than precipitated VC particles.

6- Since all of the FGMs in this study could be successfully processed, selecting the appropriate VC content depends on the level of improvements required for hardness and wear resistance. Although the 5wt.%VC composite system possessed the highest hardness and wear resistance among the others, its processability was found to be limited to a relatively narrow window.

5.4 References

[1] M.J. Holzweissig, A. Taube, F. Brenne, M. Schaper, T. Niendorf, Microstructural Characterization and Mechanical Performance of Hot Work Tool Steel Processed by Selective Laser Melting, Metallurgical and Materials Transactions B 46(2) (2015) 545-549.

[2] R. Mertens, B. Vrancken, N. Holmstock, Y. Kinds, J.-P. Kruth, J. Van Humbeeck, Influence of powder bed preheating on microstructure and mechanical properties of H13 tool steel SLM parts, Physics Procedia 83 (2016) 882-890.

[3] T.H. Becker, D. Dimitrov, The achievable mechanical properties of SLM produced Maraging Steel 300 components, Rapid Prototyping Journal (2016).

[4] N. Zhang, J. Liu, H. Zhang, N.J. Kent, D. Diamond, M. D Gilchrist, 3D Printing of Metallic Microstructured Mould Using Selective Laser Melting for Injection Moulding of Plastic Microfluidic Devices, Micromachines 10(9) (2019) 595.

[5] M. Mazur, M. Leary, M. McMillan, J. Elambasseril, M. Brandt, SLM additive manufacture of H13 tool steel with conformal cooling and structural lattices, Rapid Prototyping Journal (2016).

[6] M. Mazur, P. Brincat, M. Leary, M. Brandt, Numerical and experimental evaluation of a conformally cooled H13 steel injection mould manufactured with selective laser melting, The International Journal of Advanced Manufacturing Technology 93(1-4) (2017) 881-900.

[7] C. Liu, Z. Cai, Y. Dai, N. Huang, F. Xu, C. Lao, Experimental comparison of the flow rate and cooling performance of internal cooling channels fabricated via selective laser melting and conventional drilling process, The International Journal of Advanced Manufacturing Technology 96(5-8) (2018) 2757-2767.

[8] M.F. El Kashouty, A.E. Rennie, M. Ghazy, Tool Life Performance of Injection Mould Tooling Fabricated by Selective Laser Melting for High-Volume Production, Materials 12(23) (2019) 3910.

[9] J.C. Simmons, X. Chen, A. Azizi, M.A. Daeumer, P.Y. Zavalij, G. Zhou, S.N. Schiffres, Influence of processing and microstructure on the local and bulk thermal conductivity of selective laser melted 316L stainless steel, Additive Manufacturing 32 (2020) 100996.

[10] Y. Bai, Y. Yang, Z. Xiao, D. Wang, Selective laser melting of maraging steel: mechanical properties development and its application in mold, Rapid Prototyping Journal (2018).

[11] E. Yasa, K. Kempen, J. Kruth, L. Thijs, J. Van Humbeeck, Microstructure and mechanical properties of maraging steel 300 after selective laser melting, Solid freeform fabrication symposium proceedings, 2010, pp. 383-396.

[12] C. Tan, K. Zhou, W. Ma, P. Zhang, M. Liu, T. Kuang, Microstructural evolution, nanoprecipitation behavior and mechanical properties of selective laser melted high-performance grade 300 maraging steel, Materials & Design 134 (2017) 23-34.

[13] R. Mahshid, H.N. Hansen, K.L. Højbjerre, Strength analysis and modeling of cellular lattice structures manufactured using selective laser melting for tooling applications, Materials & Design 104 (2016) 276-283.

[14] M. Narvan, K.S. Al-Rubaie, M. Elbestawi, Process-Structure-Property Relationships of AISI H13 Tool Steel Processed with Selective Laser Melting, Materials 12(14) (2019) 2284.

[15] J.J. Yan, D.L. Zheng, H.X. Li, X. Jia, J.F. Sun, Y.L. Li, M. Qian, M. Yan, Selective laser melting of H13: microstructure and residual stress, Journal of Materials Science 52(20) (2017) 12476-12485.

[16] R. Casati, M. Coduri, N. Lecis, C. Andrianopoli, M. Vedani, Microstructure and mechanical behavior of hot-work tool steels processed by Selective Laser Melting, Materials Characterization 137 (2018) 50-57.

[17] J. Ge, N. Fan, Y. Long, J. Lin, Y. Lei, S. Yin, Investigation on H13 buildups produced with wire arc additive manufacturing: Deposition strategies-induced microstructural evolution and mechanical performances, Journal of Alloys and Compounds (2020) 157893.

[18] J. Džugan, K. Halmešová, M. Ackermann, M. Koukolikova, Z. Trojanová, Thermo-physical properties investigation in relation to deposition orientation for SLM deposited H13 steel, Thermochimica Acta 683 (2020) 178479.

[19] H. Fayazfar, M. Salarian, A. Rogalsky, D. Sarker, P. Russo, V. Paserin, E. Toyserkani, A critical review of powder-based additive manufacturing of ferrous alloys: Process parameters, microstructure and mechanical properties, Materials & Design 144 (2018) 98-128.

[20] H. Choi, A deeper understanding of heat checking, an old but frequently overlooked failure mechanism, of downhole drilling components, SPE/IADC drilling conference, Society of Petroleum Engineers, 1997.

[21] W.E. Bryson, Heat Treatment, Selection, and Application of Tool Steels, (2005).

[22] A. Bahrami, S.M. Anijdan, M. Golozar, M. Shamanian, N. Varahram, Effects of conventional heat treatment on wear resistance of AISI H13 tool steel, Wear 258(5-6) (2005) 846-851.

[23] C. Chen, K. Yan, L. Qin, M. Zhang, X. Wang, T. Zou, Z. Hu, Effect of heat treatment on microstructure and mechanical properties of laser additively manufactured AISI H13 tool steel, Journal of Materials Engineering and Performance 26(11) (2017) 5577-5589.

[24] L. Xue, J. Chen, S.-H. Wang, Freeform laser consolidated H13 and CPM 9V tool steels, Metallography, Microstructure, and Analysis 2(2) (2013) 67-78.

[25] J. Chen, L. Xue, Laser cladding of CPM tool steels on hardened H13 hot-work steel for low-cost high-performance automotive tooling, JOM 64(6) (2012) 688-693.

[26] F. Klocke, K. Arntz, M. Teli, K. Winands, M. Wegener, S. Oliari, State-of-the-art laser additive manufacturing for hot-work tool steels, Procedia CIRP 63(1) (2017) 58-63.

[27] A. Çiçek, F. Kara, T. Kıvak, E. Ekici, I. Uygur, Effects of deep cryogenic treatment on the wear resistance and mechanical properties of AISI H13 hot-work tool steel, Journal of Materials Engineering and Performance 24(11) (2015) 4431-4439.

[28] M. Wang, W. Li, Y. Wu, S. Li, C. Cai, S. Wen, Q. Wei, Y. Shi, F. Ye, Z. Chen, High-temperature properties and microstructural stability of the AISI H13 hot-work tool steel processed by selective laser melting, Metallurgical and Materials Transactions B 50(1) (2019) 531-542.

[29] R.A. Mesquita, Tool steels: Properties and performance, CRC press2016.

[30] J. Sander, J. Hufenbach, L. Giebeler, H. Wendrock, U. Kühn, J. Eckert, Microstructure and properties of FeCrMoVC tool steel produced by selective laser melting, Materials & Design 89 (2016) 335-341.

[31] G.A. Roberts, R. Kennedy, G. Krauss, Tool steels, ASM international1998.

[32] H. Chen, Y. Lu, Y. Sun, Y. Wei, X. Wang, D. Liu, Coarse TiC particles reinforced H13 steel matrix composites produced by laser cladding, Surface and Coatings Technology (2020) 125867.

[33] W. Jiang, R. Kovacevic, Laser deposited TiC/H13 tool steel composite coatings and their erosion resistance, Journal of Materials Processing Technology 186(1-3) (2007) 331-338.

[34] J. Chen, L. Xue, Laser cladding of wear resistant CPM 9V tool steel on hardened H13 substrate for potential automotive tooling applications, Materials science and technology (2010) 2459-2470.

[35] P. Kattire, S. Paul, R. Singh, W. Yan, Experimental characterization of laser cladding of CPM 9V on H13 tool steel for die repair applications, Journal of Manufacturing Processes 20 (2015) 492-499.

[36] S. Henschel, V. Kietov, F. Deirmina, M. Pellizzari, L. Krüger, Fracture toughness of a hot work tool steel-TiC composite produced by mechanical milling and spark plasma sintering, Materials Science and Engineering: A 709 (2018) 152-159.

[37] A. Dadoo, S.M.A. Boutorabi, S. Kheirandish, Effect of titanium carbide concentration on the morphology of MC carbides in pulsed laser surface alloyed AISI H13 tool steel, Optics & Laser Technology 112 (2019) 236-244.

[38] M. Balbaa, A. Ghasemi, E. Fereiduni, M. Elbestawi, S. Jadhav, J.-P. Kruth, Role of powder particle size on laser powder bed fusion processability of AlSi10mg alloy, Additive Manufacturing (2020) 101630.

[39] E. Fereiduni, A. Ghasemi, M. Elbestawi, Characterization of Composite Powder Feedstock from Powder Bed Fusion Additive Manufacturing Perspective, Materials 12(22) (2019) 3673.

[40] T. DebRoy, H.L. Wei, J.S. Zuback, T. Mukherjee, J.W. Elmer, J.O. Milewski, A.M. Beese, A. Wilson-Heid, A. De, W. Zhang, Additive manufacturing of metallic components – Process, structure and properties, Progress in Materials Science 92 (2018) 112-224.

[41] H. Mindt, M. Megahed, N. Lavery, M. Holmes, S. Brown, Powder bed layer characteristics: the overseen first-order process input, Metallurgical and Materials Transactions A 47(8) (2016) 3811-3822.

[42] A.B. Spierings, G. Levy, Comparison of density of stainless steel 316L parts produced with selective laser melting using different powder grades, Proceedings of the Annual International Solid Freeform Fabrication Symposium, Austin, TX, 2009, pp. 342-353.

[43] ASTM, G99-95a (2000) e1, Standard Test Method for Wear Testing with a Pin-on-Disk Apparatus, (2000).

[44] X. Zhao, B. Song, W. Fan, Y. Zhang, Y. Shi, Selective laser melting of carbon/AlSi10Mg composites: microstructure, mechanical and electronical properties, Journal of Alloys and Compounds 665 (2016) 271-281.

[45] J. Fogagnolo, F. Velasco, M. Robert, J. Torralba, Effect of mechanical alloying on the morphology, microstructure and properties of aluminium matrix composite powders, Materials Science and Engineering: A 342(1-2) (2003) 131-143.

[46] W. Zhou, X. Sun, K. Kikuchi, N. Nomura, K. Yoshimi, A. Kawasaki, Carbon nanotubes as a unique agent to fabricate nanoceramic/metal composite powders for additive manufacturing, Materials & Design 137 (2018) 276-285.

[47] G. Kasperovich, J. Haubrich, J. Gussone, G. Requena, Correlation between porosity and processing parameters in TiAl6V4 produced by selective laser melting, Materials & Design 105 (2016) 160-170.

[48] W.E. King, H.D. Barth, V.M. Castillo, G.F. Gallegos, J.W. Gibbs, D.E. Hahn, C. Kamath, A.M. Rubenchik, Observation of keyhole-mode laser melting in laser powder-bed fusion additive manufacturing, Journal of Materials Processing Technology 214(12) (2014) 2915-2925.

[49] S. Dadbakhsh, L. Hao, P. Jerrard, D. Zhang, Experimental investigation on selective laser melting behaviour and processing windows of in situ reacted Al/Fe2O3 powder mixture, Powder technology 231 (2012) 112-121.

[50] N. Kang, W. Ma, L. Heraud, M. El Mansori, F. Li, M. Liu, H. Liao, Selective laser melting of tungsten carbide reinforced maraging steel composite, Additive Manufacturing 22 (2018) 104-110.

[51] K. Mumtaz, N. Hopkinson, Selective laser melting of Inconel 625 using pulse shaping, Rapid Prototyping Journal (2010).

[52] J. Kundrák, Z. Gácsi, K. Gyáni, V. Bana, G. Tomolya, X-ray diffraction investigation of white layer development in hard-turned surfaces, The International Journal of Advanced Manufacturing Technology 62(5-8) (2012) 457-469.

[53] C. Capdevila, F.G. Caballero, C. García de Andrés, Analysis of effect of alloying elements on martensite start temperature of steels, Materials science and technology 19(5) (2003) 581-586.

[54] J. Krell, A. Röttger, K. Geenen, W. Theisen, General investigations on processing tool steel X40CrMoV5-1 with selective laser melting, Journal of Materials Processing Technology 255 (2018) 679-688.

[55] G. Krauss, Principles of heat treatment of steel, American Society for Metals, 1980 (1980) 291.

[56] Y. Huang, J. Shen, Y. Sun, J. Sun, Indentation size effect of hardness of metallic glasses, Materials & Design 31(3) (2010) 1563-1566.

[57] A. Ruiz-Moreno, P. Hähner, Indentation size effects of ferritic/martensitic steels: A comparative experimental and modelling study, Materials & Design 145 (2018) 168-180.

[58] H. Attar, L. Löber, A. Funk, M. Calin, L. Zhang, K. Prashanth, S. Scudino, Y. Zhang, J. Eckert, Mechanical behavior of porous commercially pure Ti and Ti–TiB composite materials manufactured by selective laser melting, Materials Science and Engineering: A 625 (2015) 350-356.

[59] E. Fereiduni, S.G. Banadkouki, Reliability/unreliability of mixture rule in a low alloy ferrite–martensite dual phase steel, Journal of alloys and compounds 577 (2013) 351-359.

[60] E. Fereiduni, S.G. Banadkouki, Improvement of mechanical properties in a dual-phase ferrite–martensite AISI4140 steel under tough-strong ferrite formation, Materials & Design 56 (2014) 232-240.

[61] G.E. Dieter, D.J. Bacon, Mechanical metallurgy, McGraw-hill New York1986.

[62] R.L. Fleischer, Substitutional solution hardening, Acta metallurgica 11(3) (1963) 203-209.

[63] A. Akhtar, E. Teghtsoonian, Solid solution strengthening of magnesium single crystals—I alloying behaviour in basal slip, Acta Metallurgica 17(11) (1969) 1339-1349.

[64] J. Fisher, On the strength of solid solution alloys, Acta metallurgica 2(1) (1954) 9-10.

[65] X. Li, X. Wang, M. Saunders, A. Suvorova, L. Zhang, Y. Liu, M. Fang, Z. Huang, T.B. Sercombe, A selective laser melting and solution heat treatment refined Al–12Si alloy with a controllable ultrafine eutectic microstructure and 25% tensile ductility, Acta Materialia 95 (2015) 74-82.

[66] S. Dadbakhsh, L. Hao, Effect of Al alloys on selective laser melting behaviour and microstructure of in situ formed particle reinforced composites, Journal of alloys and compounds 541 (2012) 328-334.

[67] E.J. Lavernia, T.S. Srivatsan, The rapid solidification processing of materials: science, principles, technology, advances, and applications, Journal of Materials Science 45(2) (2010) 287.

[68] S. Schmauder, C. Kohler, Atomistic simulations of solid solution strengthening of α-iron, Computational Materials Science 50(4) (2011) 1238-1243.

Chapter 6

Summary and Conclusions

6.1 Summary and conclusive remarks

AISI H13 tool steel, is a Cr-Mo hot work tool steel that has found its way in a wide variety of tooling applications owing to its high wear resistance, outstanding thermal fatigue stability, and cost advantages. The excellent balance of these properties has introduced H13 tool steel as a prime candidate in many applications including, plastic injection molding, die casting, and hot-extrusion industries. In the context of AM, LPBF processing of H13 tool steel could be quite challenging. H13 tool steel has been designed to be processed via conventional manufacturing routes, like machining processes. H13 tool steel exhibits poor printability with LPBF process (as well as low weldability) due to its high hardenability. Once the laser moves away from the location of interest, the material in that location undergoes fast cooling, and hence, hardens. Such a hardening brings about stresses since the consolidated material is highly constrained, with a concomitant risk for cracking. To make matters worse, the as-built parts usually suffer from pores, rough surfaces, distortions originating from residual stresses, and loss of alloying elements, should the process parameters are not chosen carefully.

The LPBF processing of H13 tool steel parts has been studied in the past decade. Most of the studies concentrated on densification behavior of this alloy without bringing attention

to the main hurdle in its application to the tooling industry which is its high cracking propensity. This thesis focuses on defect development in LPBF processing of H13 tool steel, through characterization of the as-built parts, and finally improving the wear resistance of the monolithic alloy by developing FGM, via LPBF process.

The Process-Structure-Property (PSP) relationship of the H13 tool steel printed using LPBF process was investigated. The H13 tool steel parts were printed over a broad range of volumetric energy densities (VED). The relative density of the as-built material, processed with and without preheating of 200°C, increased non-linearly with increasing the volumetric energy density up to a value of about 60 J/mm^3 and then no significant increase was observed. Application of the preheating not only enhanced the relative density, but also it helped in eliminating the thermally-induced cracks. In fact, preheating of the base plate was found to broaden the safe processing window of LPBF-manufactured H13 tool steel. The best surface roughness achieved was 6.1 µm. Due to un-melted powders, further improvements in the surface roughness were not possible and parts need to go through post-processing in case better finishes are required.

Moreover, as the other defect in the LPBF processing of the H13 tool steel, residual stresses were investigated thoroughly via direct (i.e., XRD) and indirect (i.e., twin-cantilever beam deflection) experimental measurements combined with the part-level simulations. Contributing factors to the regime and magnitude of residual stresses in the LPBF-processing of the alloy at hand were determined. According to the thermal gradient model, the residual stress in the as-consolidated layer in LPBF process is usually tensile in nature. However, in the case of H13 tool steel, the martensitic phase transformation not only offsets the tensile stresses but also leaves behind a considerable amount of compressive residual stresses, especially in the non-preheated scenario. The impact of martensitic phase

transformation on the residual stress regime gets alleviated when preheating is applied. Application of 200°C preheating not only helped to avoid the formation of cracks but also led to the tensile stresses in the order of 300 MPa which are far away from the ultimate tensile strength of the H13 tool steel. Hence, the fabricated as-built part can be regarded as end-use components with no need for costly and time-consuming stress-relief post-processing treatments. A sequentially-coupled finite element model was developed to predict the beam deflections. It was found that ignoring the martensitic phase transformation in the part-level simulation caused a discrepancy between the experimental and simulation results of beam deflections. A solution was proposed to account for the discrepancy between the experiment and the finite element results.

Finally, functionally graded bi-materials (FGM) having monolithic H13 at the bottom and VC-H13 composites with VC contents corresponding to 1, 3, and 5wt.% on top were fabricated via the LPBF process aiming at improving the wear resistance of H13 tool steel. 1wt.%VC-H13 and 3wt.%VC-H13 were found to be highly processable since almost defect-free parts (>99.5% relative density) were achievable in a wide range of energy densities. However, the addition of 5wt.%VC significantly degraded the processability by narrowing down the energy density range leading to highly dense parts. As the VC content increased, higher energy density levels were required to obtain samples with the highest density. This was attributed to the endothermic nature of the VC dissolution during the LPBF processing of composites which consumes a fraction of the heat input subjected to the system. The mechanical properties of optimum samples were characterized through microhardness, nanohardness, and wear tests. The incorporation of VC significantly improved the mechanical properties, 17-40% in microhardness, 10-40% in nanohardness, and 20-53% in wear resistance. The underlying reasons behind such an improvement were

correlated to the dissolution of VC during the heating stage of the LPBF process and the formation of (V+C)-supersaturated solid solution in large extents as a result of extremely high cooling rates. These improvements introduce LPBF-processed FGMs as promising candidates for applications in which wear resistance is paramount.

6.2 Strength, limitations, and future work

The effect of process parameters on the defect development during the LPBF processing of H13 tool steel investigated in the current thesis helps to guarantee the reliable fabrication of tools and dies, which in turn, facilitates the full-scale implementation of AM in the tool and die making industry. Application of 200°C of preheating to the substrate not only proves to be a cost-effective solution to the cracking problem of H13 tool steel in the LPBF process (as apposed to the alloying method), but also improves the quality of the parts and eliminates the need for costly stress-relief post-processing steps. A numerical model was developed to predict the beam deflection of the LPBF-processed H13 tool steel. Moreover, taking advantage of the unique capabilities of LPBF process in creating functional materials, FGMs in this case, wear performance of the monolithic H13 was improved by adding VC particles. This would imply enhanced productivity in an industrial application which renders the obtained results in this research quite valuable.

On the flip side, there are still some limitations to the obtained results that would invoke the necessity of the further studies as the future work. The finite element model proposed in this thesis to predict the beam deflections in the LPBF-processed H13 tool steel applies to a part-level analysis. Considering the multi-scale nature of AM processes, from a computational perspective, incorporation of important physics that take place on a different

scale to obtain accurate results, still remains a challenge. In this case, martensitic phase transformation that occurs on a micron level brought about a large discrepancy between the experimental and numerical results. Despite the fact that a customed solution (Only applicable to H13 tool steel) to account for such a discrepancy was proposed in this thesis, it is worthwhile to note that, a comprehensive finite element model that is applicable to various materials still remains a void in the literature.

H13 tool steel is famous for its high toughness. However, the obtained high hardness in the as-built condition (~52-56 HRC) after LPBF-processing might compromise this stronghold. Of course, the required properties for the end-use components are directly dictated by the nature of the application. In the applications such as plastic injection molding where wear resistance is more needed that toughness, the as-built parts processed with LPBF could potentially be regarded as end-use components. On the other hand, the necessity of the proper heat-treatment cycles to attain a suitable balance between toughness and hardness becomes obvious in the case of applications like close-die forging where impact toughness of the die components plays a crucial role in the longevity of the tooling. In this case, as-built components must be put through complicated and costly heat-treatment post-processing. The same rationale applies to the case of the FGMs fabricated with LPBF process in this thesis. The design of a proper heat-treatment cycles to obtain desired properties for the case of FGMs with supersaturated-(V+C) in the martensitic matrix would be an interesting topic of future work. Upon heat-treatment, VC would precipitate in the matrix. Controlling the size of these precipitates and extent of precipitation could potentially have significant role on the mechanical properties of the components.

Finally, the FGMs fabricated in this thesis are simple cylindrical samples that would act as a proof of concept that how LPBF process can contribute to design of functional materials. However, in the real industrial applications, the dies and the associated components posses complex freeform geometries. Without a doubt, fabrication of functionally graded tools and die with complex geometries with the current LPBF machines that have the capability of delivering a monolithic powder would be a challenge. Retrofitting the current machines with reliable powder delivery systems that can support multiple materials, is a technical challenge that needs adequate attention.

6.3 Contribution

This thesis serves as an important step in dealing with the materials aspect of LPBF processing of AISI H13 tool steel. The findings of this study have contributed to understanding the influence of the LPBF processing parameters on the flaw development of this commonly used hot-work tool steel. Also, this thesis extends the applicability of the AM technology from “geometric design” to “functional material design”. Thus, paves the way for the full-scale implementation of AM technology in tooling applications.